EUROPEAN ORGANIZATION FOR NUCLEAR RESEARCH

CERN-PPE/90-168
13 November 1990

THE STANDARD MODEL PARAMETERS

Review of Recent Results on the Intermediate Vector Boson Production and Decay Properties at the CERN and FNAL $\bar{p}p$ Colliders[1)]

H. PLOTHOW-BESCH
CERN - PPE, CH - 1211 Genève 23, Switzerland

Abstract

Recent measurements on the W and Z production and decay properties from the UA1, UA2 and CDF experiments at the CERN and the FNAL $\bar{p}p$ colliders are summarized and compared to e^+e^- and deep-inelastic lepton-nucleon scattering experiments and to theoretical predictions. The width of the W boson has been determined to $\Gamma_W = 2.184 \pm 0.124$ GeV/c^2. The W mass has been precisely measured to $m_W = 80.14 \pm 0.31$ GeV/c^2 and from the mass ratio, m_W/m_Z, a precise value of $\sin^2\theta_W = 0.2265 \pm 0.0062$ has been obtained. From this measurement an upper limit on the mass of the top-quark of $m_{top} < 219$ GeV/c^2 at the 95% confidence level has been deduced. Direct searches for the top-quark have given a best lower limit on its mass of $m_{top} > 89$ GeV/c^2. No deviations from the Standard Model predictions have been found.

1) Work partially supported by the Deutsche Forschungsgemeinschaft, Bonn, FRG

1. INTRODUCTION

The CERN SPS $\bar{p}p$ collider program [1] of the years 1981 - 1985 has been a great success and has given important contributions to the understanding of the elementary forces in the field of particle physics. The discovery of the Intermediate Vector Bosons [2], the carriers of the electro-weak forces, $W^{\pm}$ and Z^0, by the UA1 and UA2 collaborations in 1983 has given convincing confirmation of the validity of the Standard Model of Glashow, Salam and Weinberg [3] which unifies the electromagnetic and the weak forces. Furthermore, the observation of hadronic jets, produced by the interaction of the constituents of protons and antiprotons, has given the possibility to study hard parton collisions in great detail [4]. Encouraged by such achievements and motivated by equally exciting physics topics still unrevealed and possibly within reach - the top-quark and supersymmetry searches are just two examples - CERN has undertaken in the years 1985-1987 an important upgrading of the $\bar{p}p$ collider complex [5], which was expected to increase the peak-luminosity by one order of magnitude up to $\mathcal{L}_{max} \sim 5 \cdot 10^{30}\ cm^{-2}\ s^{-1}$, a value which has been nearly achieved during the collider run in 1989.

In spring 1987 the $\bar{p}p$ collider complex, TEV-I, at Fermilab (FNAL) has started its physics program at a centre-of-mass energy of $\sqrt{s} = 1.8$ TeV, the highest energy available for the coming years at a hadron collider. Since 1987 in a second data-taking period of about one year, from June 1988 to May 1989, the reliability of the machine as well as the peak-luminosity has been increased to such a level that its performance became very much comparable to that of the CERN collider.

While the mass of the Z^0 has already been measured with high accuracy at the e^+e^- colliders SLC at SLAC and LEP at CERN - a precision of $\Delta m_Z \sim 30\ MeV/c^2$ has been achieved [6] -, the W sector will remain the domain of $\bar{p}p$ colliders until LEP phase II starts around 1994, because the present energy of LEP is not sufficient to produce a $W^{\pm}$ pair, and the production of a single W is not detectable at the existing e^+e^- machines due to its negligible cross section.

Many reviews on the properties of the Intermediate Vector Bosons, together with tests of the Standard Model parameters obtained from $\bar{p}p$ collider, deep-ineleastic lepton-nucleon scattering as well as e^+e^- experiments have been written over the last few years. Recently the statistics from the CERN $\bar{p}p$ collider has been increased and new data from the FNAL $\bar{p}p$ collider have become available. Futhermore, the SLC and LEP e^+e^- colliders which an available high statistics of already more than 10^5 Z^0 for each LEP experiment have successfully started last year. This altogther allows for even higher precision tests of

the Standard Model and gives enough motivation for an additional review. In this article we restrict ourselves to a review of recent results from the $\bar{p}p$ colliders. These are compared to recent LEP results and new results from the deep-inelastic lepton-nucleon scattering experiments whenever it is relevant.

In the following the four detectors, UA1, UA2, CDF and DØ, which are studying the physics questions mentioned above at the CERN and FNAL $\bar{p}p$ colliders, are shortly reviewed and their basic concepts for identification of electrons, muons, taus, neutrinos and jets are described, with a particular insistance to the detector calibrations. After having defined the theoretical framework, the latest experimental results on the production and the decay properties of the Intermediate Vector Bosons at the $\bar{p}p$ colliders are summarized. In particular, emphasis has been given to the precise measurements of the masses of the W and Z bosons and of their significantly improved mass ratio. The Standard Model parameters derived from these measurements are compared to results from other experiments and to theoretical predictions. Direct searches for the still missing sixth quark, the top-quark, predicted by the Standard Model are reviewed.

2. THE DETECTORS

The four big detectors, UA1, UA2, CDF and D0, have been designed to study $\bar{p}p$ collisions at the CERN and FNAL $\bar{p}p$ colliders and to explore the physics of the Intermediate Vector Bosons (IVBs). The main signature of the IVBs in $\bar{p}p$ collisions is the production of charged leptons with high transverse energy accompanied by large missing transverse momentum in case of W production. Therefore all detectors have given special emphasis to identify electrons, muons (except UA2), taus, neutrinos and jets with high efficiency and to measure their energy and their momenta with high accuracy.

In order to exploit the possibilities offered by the upgraded collider facility at CERN in 1987, an improvement program was also undertaken on the two big $\bar{p}p$ collider experiments UA1 and UA2. At FNAL until now only one experiment accumulated data in the years 1987 to 1989. Another experiment, DØ, is still under construction and is expected to be ready for data-taking in the next run in 1991.

2.1 The UA1 detector at CERN

The UA1 detector is a general-purpose detector with an almost 4π angular coverage around the $\bar{p}p$ interaction region. An artistic view of the detector is shown in Fig.1. The detector, as it has been used in the 1981-1985 runs, is shortly described in the next paragraph.

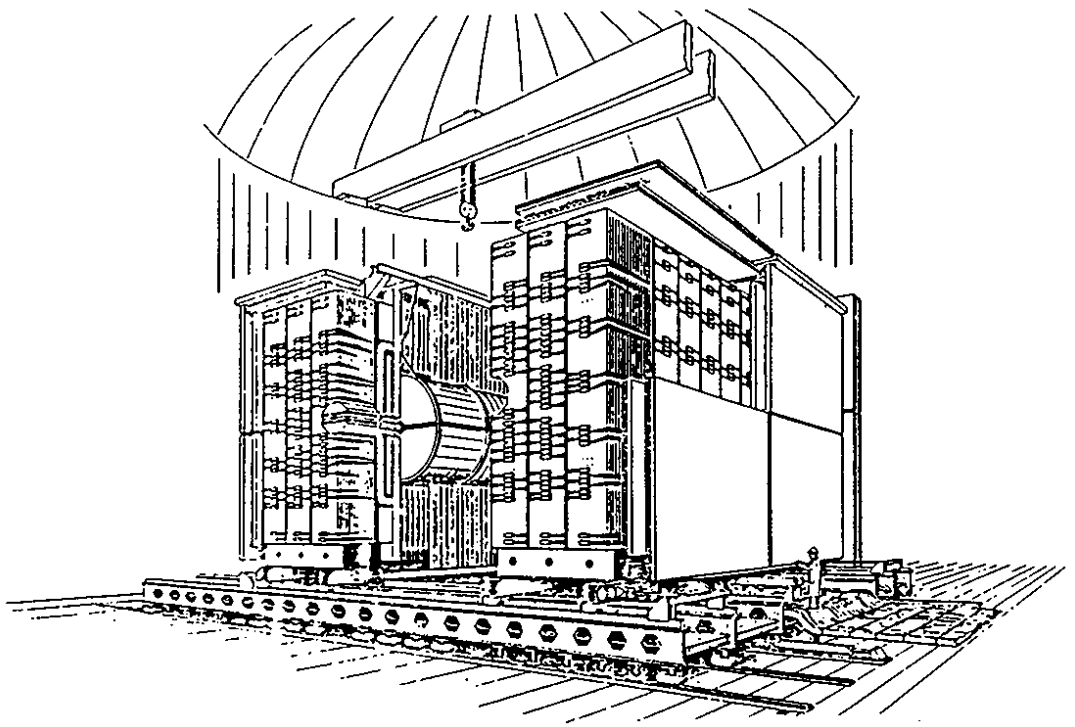

Figure 1
Artistic view of the UA1 detector

Particles first traverse a large drift chamber (6 m long, 2.4 m in diameter). This allows the reconstruction of charged tracks, and subsequently of the event vertex. A 1.5 Tesla dipole magnetic field in this region allows momentum measurement of charged tracks with a precision of typically $\Delta p/p^2 \sim 0.005$ $(GeV/c)^{-1}$ in the horizontal plane. The magnetic field volume contains the central electromagnetic (EM) calorimeter covering the polar angular range of $25° < \theta < 155°$ relative to the beam axis which corresponds to a pseudorapidity range of $|\eta| < 1.5$ with $|\eta| = -\ln\{\tan(\theta/2)\}$ and 2π in azimuth. This calorimeter consists of 24 half-cylindrical shells on either side of the beam called

"gondolas". A gondola is made of a multilayer lead/scintillator sandwich with a total thickness of 26.6 radiation lengths (r.l.) and subtends an angular range of $\Delta\theta = 5°$ and $\Delta\phi = 180°$. Though the spatial segmentation of the calorimeter is rather coarse, four independent longitudinal EM samplings with thicknesses of 3.3, 6.6, 10.1 and 6.6 r.l. allow a measurement of the profile of deposited energy. Two end-cap (EC) EM calorimeters called "bouchons" extend the polar angular range down to $\theta = 5°$ with respect to the beam axis. Each EC calorimeter consists of 32 azimuthal sectors of a lead/scintillator sandwich with a total thickness of 27 r.l. and is also segmented four times in depth. The resolution is the same as for the central EM calorimeter (see Section 3.3). Additional chambers and calorimeters cover the small-angle region, $0.2° < \theta < 5.0°$ ($3 < |\eta| < 6$). Beyond the EM calorimeters, a hadron (HAD) calorimeter which consists of 450 independent cells with typical size of $\Delta\theta = 15°$, $\Delta\phi = 18°$ in the central region and of $\Delta\theta = 5°$, $\Delta\phi = 10°$ in the forward region measures the energy leakage from the EM calorimeters for electrons and photons, and the energy deposition for single hadrons or jets. The total thickness is ~ 5 (~ 7) absorption length in the central (forward) region. None of the calorimeters do have pointing geometry. Outside the hadron calorimeters and the magnet yoke, two planes made of 50 drift chambers separated by 60 cm are used to identify muons. Each of these drift chambers is made of four layers of drift tubes which define two orthogonal coordinates, and cover a surface of $\sim 4 \times 6$ m^2. Together with the interaction vertex and the muon-track parameters it is possible to obtain an independent measurement of the muon momentum with a relative precision of ~ 20%, from the measurement of its deflection in the magnet yoke. More details of the detector performance can be found in Ref. [7].

In UA1, for the new running periods from 1987 to 1989 with the upgraded $\bar{p}p$ collider complex, in preparation for the new Tetramethylpentane-Uranium (TMP-U) calorimeter [8] the old EM calorimeters in the central and in the forward region, the "gondolas" and the "bouchons", have been removed. This caused a substantial decrease of the momentum resolution to $\Delta p/p^2 \sim 0.02$ (GeV/c)$^{-1}$. Furthermore, the hadron-absorption in the forward region ($13° < \theta < 44°$) for μ-identification, as well as the μ-trigger itself at different levels and the data-acquisition system have been improved.

2.2 The UA2 detector at CERN

The UA2 detector, almost completely redesigned [9] and rebuilt in less than three years, has started taking data again at the beginning of the first running period of the new $\bar{p}p$ collider complex in autumn 1987. Emphasis was given to detect events with the emission of non interacting particles with high transverse momentum such as neutrinos and to improve the electron identification in the central region to help in the search for the top-quark. To cope with the expected increase in luminosity (by a factor of ~ 10) and with the amount of information available for each event, a new data acquisition and a more selective three-level trigger system were implemented [10]. A schematic view of one quarter of the new UA2 detector in the longitudinal cross section is shown in Fig. 2.

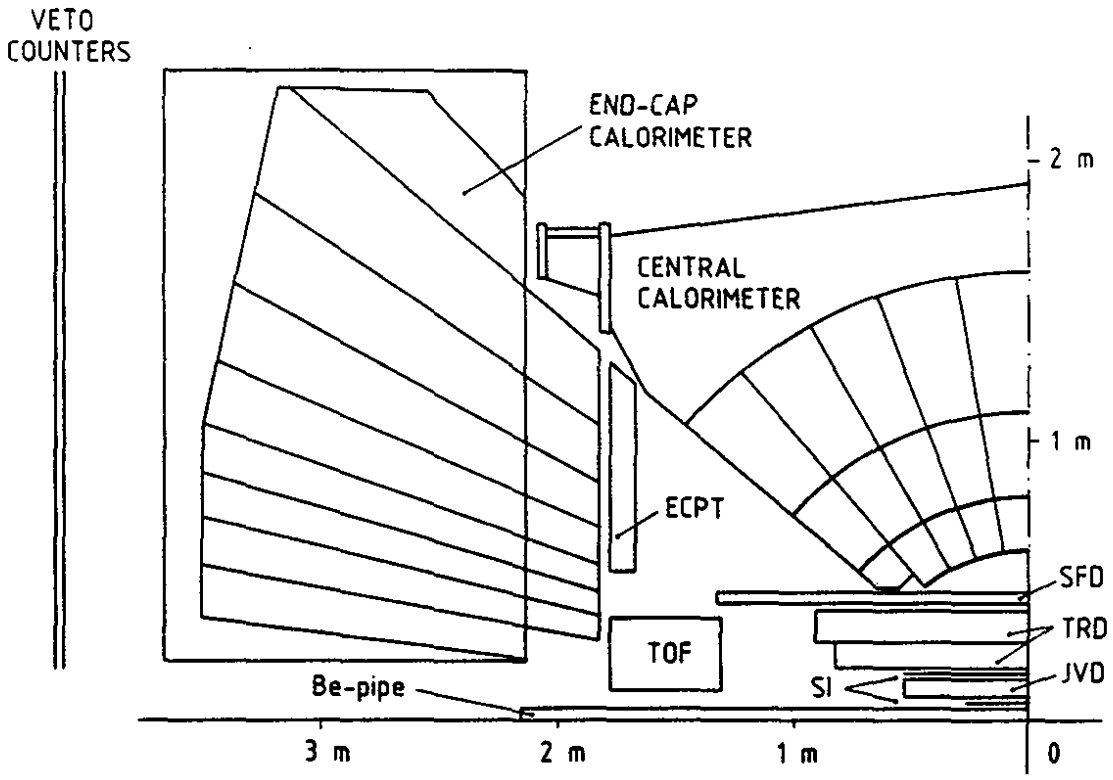

Figure 2

Schematic view of one quarter of the UA2 detector in the longitudinal cross section

The individual components are briefly described in the following. A detailed description of the design and the properties of the different detector parts can be found in Ref. [11]. The UA2 detector has no magnetic field and consists of

i. a cylindrical drift chamber of the "jet" type (JVD) with a radial thickness of only 10 cm surrounding a beryllium beam pipe to measure tracks close to the event vertex.

ii. an outer silicon hodoscope (OSI) (a total active area of about 1 m^2) supported by a carbon fibre cylinder of ~ 14 cm radius and an inner silicon hodoscope (ISI) squeezed in the free area of only 5 mm at a radius of ~ 3 cm [12]. The silicon hodoscopes serve to reject photon conversions by dE/dx measurement and to remove "ghost" tracks.

iii. a transition radiation detector (TRD) [13] which fills the available radial space of 21 cm. It consists of two coaxial cylindrical chambers, each made of a stack of polypropylene radiators followed by a Xenon chamber with a drift region followed by an amplification region. The X-ray photons produced by electrons in the radiator are rapidly absorbed by the Xenon in the early part of the chamber and generate large signals at late times with respect to the ones produced in the amplification region by any ionising particle. The TRD is used to separate electrons from charged hadrons by detection of photons emitted by particles with high γ ($\gamma = E/m_0$).

iv. a tracking and preshower detector, made of scintillating fibres (SFD) [14]. It consists of about 60000 scintillating fibres, 1 mm in diameter, arranged in 24 coaxial cylindrical layers forming 8 stereo triplets. A lead converter, 1.5 radiation length (r.l.) thick, covering 2π in azimuth and the polar angular range of the central calorimeter is inserted before the last two stereo triplets acting as a preshower detector. The fibres are read by means of 32 read-out chains, each consisting of three image intensifiers, one CCD and a FASTBUS digitizer, providing the necessary amplification, image demagnification, multiplexing and data compaction. The track resolution obtained is 0.4 mm per layer, and the resolution of the track-preshower matching is $\sigma_{R\phi}$=0.4 mm in the transverse plane and σ_z = 1.1 mm along the beam direction.

The old UA2 EM and HAD calorimeters in the central region (CC) [15], covering the polar angular range of $40° < \theta < 140°$ ($|\eta| < 1.0$) is a lead-scintillator and iron-scintillator sandwich, respectively. The scintillator in the HAD part has been completely replaced and the EM edge cells have been shortened to provide more space for the central detector.

Tracking and electron identification in the forward regions are provided by a set of proportional tube chambers (ECPT) [16] located in front of the new EC calorimeter [17] which has EM calorimetry in a polar angular range of $9° < \theta < 37.5°$ and $142.5° < \theta < 171°$ ($1.0 < |\eta| < 2.5$) and HAD calorimetry down to 6° in polar angle ($|\eta| < \pm 3$) with conventional lead-scintillator and iron-scintillator sandwich, respectively. Finally, a fast time-of-flight system (TOF) with scintillation counters situated at each side of the interaction point provides a minimum bias trigger and fast vertex reconstruction as well as good suppression of beam gas background.

2.3 The CDF detector at FNAL

The CDF experiment at FNAL tries to answer the physics questions mentioned above at the $\bar{p}p$ collider, TEV-I, at a centre-of-mass energy of 1.8 TeV, which is about three times higher than at CERN. An overview of the different detector systems can be found in Ref. 18. The general layout of this detector is shown in Fig. 3.

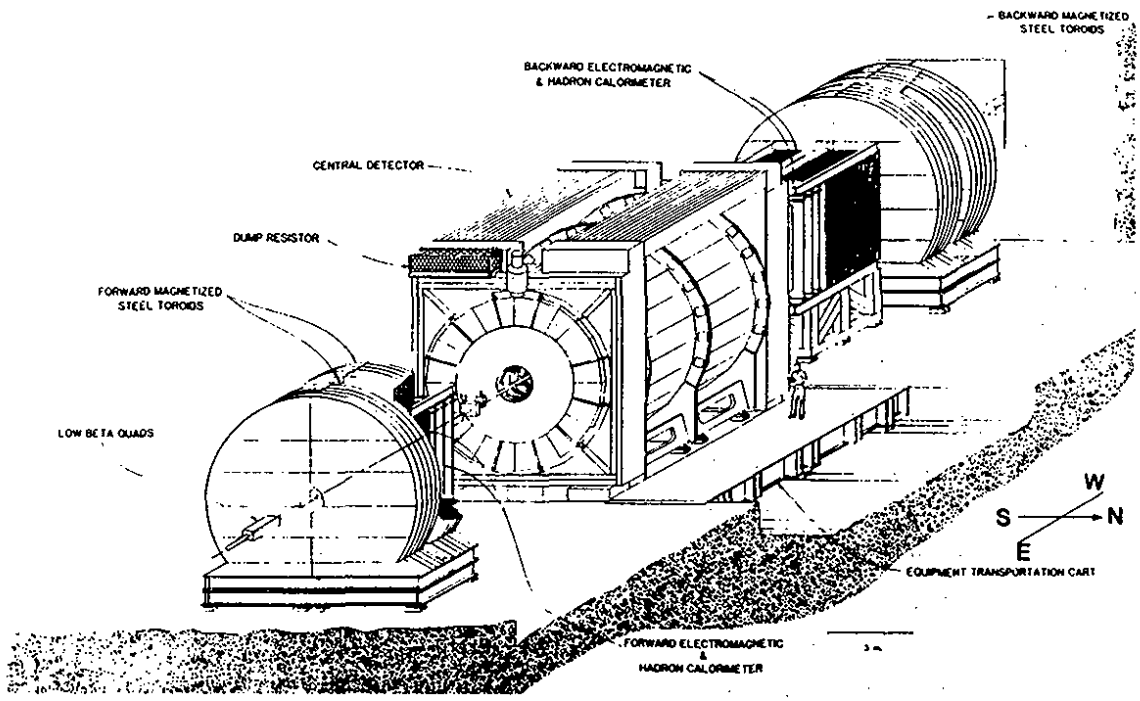

Figure 3
Perspective view of the CDF detectors

It consists of a central detector which is made up of a solenoidal magnet, steel yoke, tracking chambers, EM shower counters, HAD calorimeters and muon chambers, and two symmetric forward-backward detectors consisting of segmented time-of-flight counters, EM shower counters, HAD calorimeters and muon toroidal spectrometers. Outside the tracking devices the EM and HAD calorimeters cover 2π in azimuth and a range of $1.7° < \theta < 178.3°$ in polar angle (corresponding to a pseudorapidity range of $|\eta| < 4.2$). All calorimeters are constructed as multilayer sandwiches with no pointing geometry. The EM calorimeter uses lead as radiator and is 20 r.l. thick. The HAD

calorimeter uses iron as converter and has a thickness of at least 4 absorption lengths. In the central region ($37° < \theta < 143°$; $|\eta| < 1.1$) the sampling medium is scintillator with a segmentation of 0.1 units in $\Delta\eta$ and 15° in $\Delta\phi$, while outside this region, for the "plug" ($1.1 < |\eta| < 2.4$) and for the forward ($2.4 < |\eta| < 4.2$) calorimeters, gas-proportional-tubes are used with a segmentation of 0.1 units in $\Delta\eta$ and 5° in $\Delta\phi$. Proportional strip-chambers embedded near the shower maximum at a depth of 5.9 r.l. in the central electromagnetic calorimeter measure the position and the shape of electromagnetic showers with an accuracy of 3 mm.

In addition, a superconducting solenoid magnet with maximum field of 1.5 Tesla allows to measure the momenta of charged tracks with a resolution of $\Delta p_T/p_T^2 = 0.002$ $(GeV/c)^{-1}$ in the central region ($|\eta| < 1.1$), becoming $\Delta p_T/p_T^2 = 0.001$ $(GeV/c)^{-1}$ with a vertex constrained fit.

The CDF tracking system allows to reconstruct particle trajectories over the full region covered by calorimetry. It consists of four parts :

i) the vertex Time Projection Chambers (TPCs [19]) made out of 8 small chambers, which provide vertex reconstruction and track information in $|\eta| < 3.5$. The interaction vertex in $\bar{p}p$ collisions is reconstructed with a resolution of 1 mm (rms) along the beam direction.

ii) the central tracking chamber (CTC), a large cylindrical drift chamber providing 84 samples in a tilted cell of the "jet" type. It measures with excellent spatial and momentum resolution the charged particle trajectories in the R-ϕ plane to determine their curvature in the magnetic field and thus the particle momenta.

iii) the system of central drift tubes surrounding the CTC which provide a correlated R-ϕ-z measurement using charge division with high resolution and

iv) the forward tracking chambers which allow the reconstruction of tracks leaving the central detector through the 10° hole in the end "plug".

Behind ~ 5 interaction lengths of calorimetry is the central muon detector covering a pseudorapidity range of $|\eta| < 0.63$. Four layers of drift chambers for μ-identification with alternating pairs of wires projecting back to the interaction vertex are mounted at the back of the central calorimeter modules and in between magnetized iron toroids which are located behind the "plug" and forward calorimeters covering a range of polar angles $2° < \theta < 10°$ ($2.4 < |\eta| < 4.0$).

Scintillation counters covering the range of $3.2 < |\eta| < 5.8$ are located on each side of the detector. At least one hit in these counters on each side of the interaction region signals an inelastic event.

2.4 The DØ detector at FNAL

A fourth experiment, DØ [20], also foreseen at FNAL is nearly completed. This detector will probably start taking data for the next collider run at FNAL scheduled for summer of 1991.

The detector layout, shown in Fig. 4, has taken advantage of the experience gained with previous collider experiments.

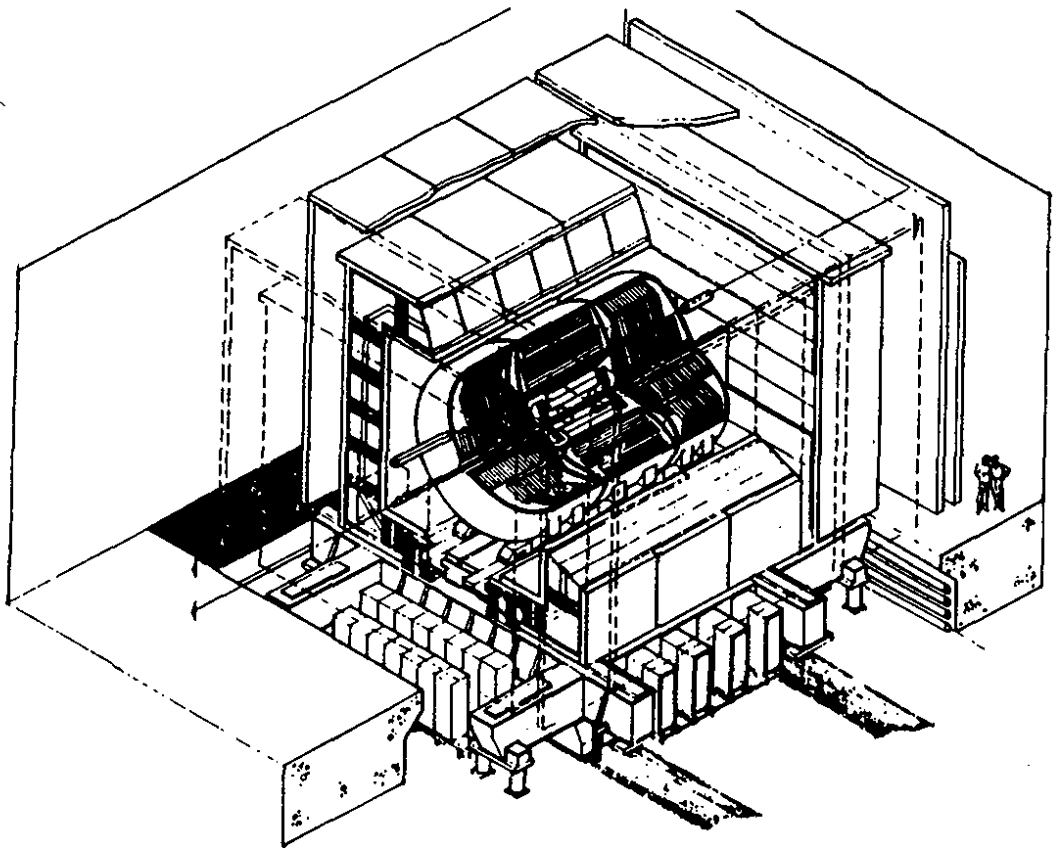

Figure 4
Isometric view of the DØ detectors

Major emphasis has been placed on good calorimeter hermeticity and on lepton identification. For the calorimeters which consist of a central part, end-caps and end-plug

modules, the uranium/liquid-argon technique has been chosen, resulting in a compact design with excellent transverse and longitudinal granularity and good energy resolution. In addition to the highly segmented EM calorimeter, electron identification will be strongly enhanced in the central and the forward regions by layers of transition radiation detectors interleaved by drift-chambers with dE/dx measuring capabilities. The muon detection system with magnetized iron for muon momentum measurements up to ~ 300 GeV/c, covers all polar angles down to $\theta = 11°$. As UA2 has DØ no magnetic field in the tracking region.

3. PARTICLE IDENTIFICATION AND DETECTOR CALIBRATION

In order to search for the Intermediate Vector Bosons (IVBs) and to study their production and decay properties, all three experiments have chosen the leptonic decay modes in spite of the smaller branching ratios compared to the decay into $q\bar{q}$ pairs which amounts to ~ 70%. The latter would appear as two-jet events which are indeed very hard to separate from the large QCD background continuum from hard parton scattering, which is approximately two orders of magnitude larger than the IVB signal and cannot easily be reduced because there is no handle to distinguish jets coming from W and Z decays from those due to hard parton scattering.

3.1 Lepton identification

Some basic considerations on lepton identification at the $\bar{p}p$ colliders are described below. The details depend very much on the particular detector.

3.1.1 Electron identification

The purpose of the electron identification criteria is to select high-p_T isolated electrons with large acceptance and to reject the backgrounds coming from QCD jets with high efficiency. The main background arises from pathological jet fragmentation (i.e. from jets containing a large transverse momentum π^o or multi-π^o's, where a charged π overlaps in space with a π^o), or photon conversions which occur in the beam pipe or in the detector, resulting in fake electron candidates. Therefore, at least for the W and Z physics, all three operational experiments use somewhat similar electron identification criteria. Electron candidates are selected requiring high transverse energy showers in the electromagnetic calorimeters ($E_T > 15$ GeV in UA1, $E_T > 20$ GeV in UA2 and $E_T > 25$ GeV in CDF) with the presence of a charged track . Cuts are made on the shower profile, exploiting the

four longitudinal samplings available in UA1, the small lateral cell size in UA2 and the strip-chamber shower profile in the z direction together with the lateral energy sharing between towers in CDF. Small leakage into the hadronic calorimeters is also required, compatible with an electron of the appropriate energy. In UA1 and CDF an additional requirement of momentum-energy matching is made. In UA2, where there is no magnetic field, the position in space measured by the preshower detectors (which cover the full solid angle of the calorimeters) has to match the track impact point. Furthermore the charge deposited by the electromagnetic shower has to exceed a threshold equivalent to several minimum-ionizing particles, as expected for electrons. In addition, in all three experiments, the electron candidate is required to be "isolated" in the sense that only a small amount of energy should be observed nearby. To ensure that an event comes from a real beam-beam collision UA2 and CDF require an additional cut on the longitudinal position of the event vertex. The cuts used by UA1, UA2 and CDF to identify electrons from $W \rightarrow e\nu$ decays are summarized in Table 1. For the identification of electrons from $Z^0 \rightarrow e^+e^-$ decays the experiments use somewhat looser identification criteria because the background is strongly reduced by the requirement of two electrons in the event.

The overall efficiencies of these selection criteria are estimated to be around ~ 65% (UA1 and UA2) and ~ 85% (CDF) for electrons with a rejection factor of more than 50000 against hadronic jets. These efficiencies do not apply to electrons inside or near to jets, such as those coming from semileptonic decays of heavy flavours, which would be largely suppressed by the implicit or explicit isolation criteria. A higher background rejection has been achieved in searching for the top-quark, but only at the cost of decreased efficiency.

Table 1 : Electron identification criteria

Variable	UA1	UA2	CDF
E_T cluster	> 15 GeV	> 20 GeV	> 25 GeV
Shower profile	Consistent with electron (longitudinal and lateral from test beams)	Similar	Similar
Charged track	Required (except $\Delta\phi < \pm 5°$ wrt vertical plane)	Required	Required
Momentum to energy matching	$1/p - 1/E < 3\,\sigma$	no magnetic field	$0.5 < E/p < 1.4$
Preshower	-	High charge and tight Track/Shower match	Similar
Isolation	$E_T < 3.2$ GeV in cone ~ 45°	-	$\frac{\Sigma E_T - E_T^e}{E_T^e} < 0.1$ in cone with $R = \sqrt{(\Delta\phi^2+\Delta\eta^2)}<0.4$
z-vertex	-	$\lvert z_V\rvert < 250$ mm	$\lvert z_V\rvert < 600$ mm
Efficiency	~ 67%	~ 65%	~ 85%

As an example, the UA2 distribution of events containing at least one electron candidate is shown in Fig. 5 in the (p_T^e, p_T^ν) plane, where p_T^e is the measured transverse momentum of the electron candidate and p_T^ν the measured missing transverse momentum (see Section 3.1.3) in the event. As can be seen in Fig. 5, the $W \rightarrow e\nu$ decays are visible as a band ($p_T^e \approx p_T^\nu$) in the high p_T^e and high p_T^ν region, while the $Z^o \rightarrow e^+e^-$ decays, which are not well separated from the background yet, are concentrated in the high p_T^e and low p_T^ν region. The main background coming from misidentified electrons from QCD jet events, photon conversions and semileptonic b decays is concentrated in the low p_T^e and low p_T^ν region.

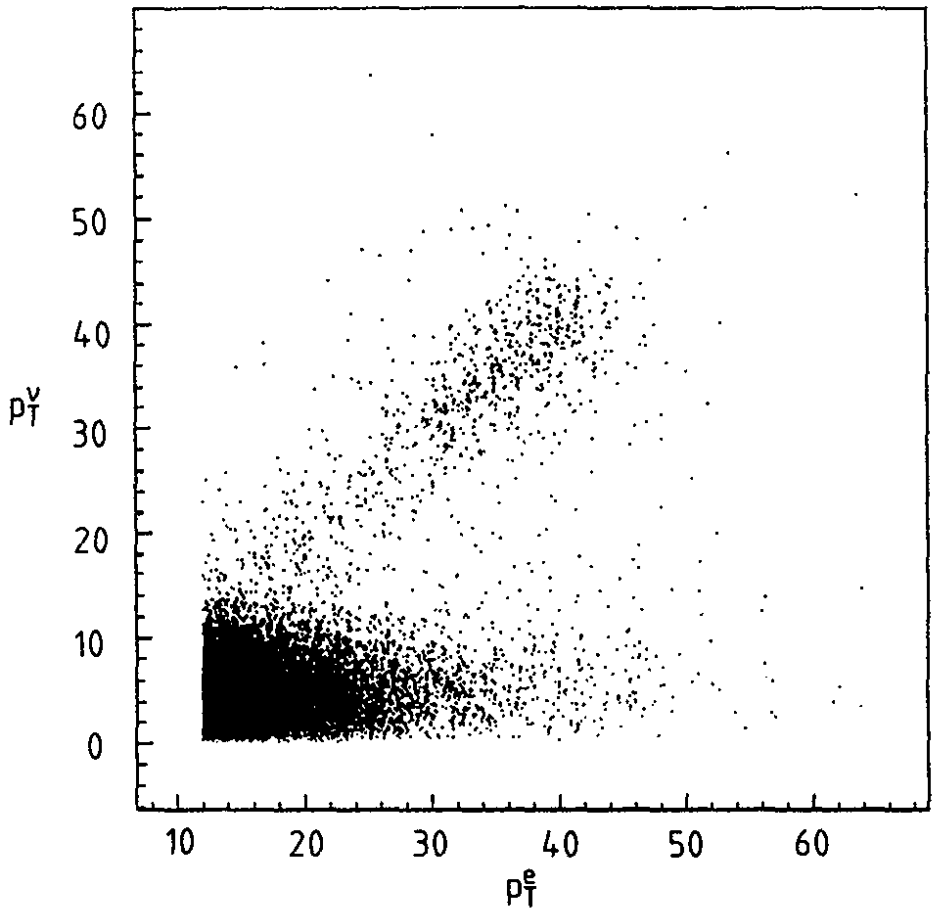

Figure 5
Example of the p_T^e vs p_T^ν distribution from UA2

3.1.2 Muon identification

Muon identification is possible in the UA1 and CDF detectors and foreseen in the DØ experiment. Only the UA2 detector has no instrumentation to detect muons. The electromagnetic and hadronic calorimeters and magnetized iron are used to filter out

hadrons. The signature for a muon is a charged track in the central detector matching a track in the muon chambers outside the shielding and a signal in the EM and HAD calorimeters characteristic of a minimum-ionizing particle. The background sources from the decay of high-p_T $K^{\pm}$'s and $\pi^{\pm}$'s as well as low-p_T K-decays are suppressed by rejecting tracks with kinks. Muons from heavy flavour decays are suppressed by an explicit isolation requirement. The overall efficiency to detect muons is around 15% (UA1 and CDF) with special selection criteria. Although clean IVB signals are observed in $W \rightarrow \mu\nu$ and $Z \rightarrow \mu\mu$ decays, the mass resolution is much worse than for electrons for both, UA1 and CDF (see Section 3.3).

3.1.3 "Neutrino" identification

A precise determination of the missing transverse momentum, $\not{p}_T = p_T^{\nu}$ is important for the detection of the reaction $W \rightarrow \ell\nu$, $\ell = e, \mu, \tau$. Even more important is a good understanding of the measurement of the W transverse momentum at production, $\vec{p}_T^{\,W} = \vec{p}_T^{\,\ell} + \vec{p}_T^{\,\nu}$, and of the intrinsic p_T^W distribution which is affected by both, the detector resolution and the quality of the $\not{p}_T$ measurement. The W mass can be determined using the transverse variables p_T^{ℓ}, p_T^{ν}, or $m_T^{\ell\nu}$ (see Section 5.5), where p_T^{ℓ} is the lepton transverse momentum and $m_T^{\ell\nu}$ is the transverse mass of the lepton-neutrino system defined as

$$m_T^{\ell\nu} = \sqrt{2 \cdot p_T^{\ell} \cdot p_T^{\nu} \cdot (1 - \cos\phi_{\ell\nu})}, \qquad (1)$$

with $\phi_{\ell\nu}$ being the angle between the lepton and the neutrino in the transverse plane. Distortions to the Jacobian shape of all three, the p_T^{ℓ}, p_T^{ν} and $m_T^{\ell\nu}$, distributions for a given value of the W mass and width depend critically on both, the detector resolution and the distribution of p_T^W. Therefore a determination of the W mass with high precision needs a detailed knowledge of the p_T^W spectrum in case of a fit to $m_T^{\ell\nu}$ as well as to p_T^{ℓ}.

Non-interacting particles, such as neutrinos, among the final state products can in principle be detected by measuring the total transverse momentum vector associated to all the visible particles. The missing transverse momentum vector is defined as

$$\vec{\not{p}}_T \equiv - \sum_i \vec{p}_T^{\,i}, \qquad (2)$$

with $\vec{p}_T^{\,i}$ being the tranverse momentum vectors of the produced particles. In an ideal detector with all produced particles being detected, one expects $\vec{\not{p}}_T \equiv 0$. If instead one or more non-interacting particles have been produced, $\vec{\not{p}}_T$ is the vector sum of their

transverse momenta. The above relation can experimentally be approximated by the relation

$$\vec{\not{p}}_T = - \sum_j E_T^j \cdot \vec{u}_j, \qquad (3)$$

with $\vec{u}_j$ being a unit vector in the transverse plane pointing from the event vertex to the centre of the j-th cell, and E_T^j being the transverse energy as measured in that cell. The sum extends over all calorimeter cells.

The quality of the $\not{p}_T$ measurement is a function of the angular coverage of the calorimeter. Experimentally one has observed that the components of the measured $\not{p}_T$ vectors have gaussian distributions for a given total transverse energy, ΣE_T, if no systematic effects play a role and the calorimeters have a ~ 4π angular coverage. Minimum bias triggers and other triggers based on scalar sums of transverse energy do not contain significant physics sources of $\not{p}_T$ such as neutrinos. Consequently, the observed transverse momentum balance in these events provides a measure of the $\not{p}_T$ resolution of the detector. The distribution of the transverse momentum balance, $\vec{\not{p}}_T$, with its two components $\not{p}_T^x$ and $\not{p}_T^y$ being gaussian with the same resolution $\sigma = \sigma_x = \sigma_y$, is well described by the form

$$\frac{dn}{d\not{p}_T^2} \sim e^{-\frac{1}{2} \cdot (\frac{\not{p}_T}{\sigma})^2}, \qquad (4)$$

where σ depends on ΣE_T.

The HAD calorimeter of UA1 covers the angular range up to very small polar angles, but has acceptance losses in azimuth of $\Delta\phi = \pm 4°$ relative to the vertical axis along the beam line. This means that only events which have an angle of $\Delta\phi > \pm 15°$ between the $\vec{\not{p}}_T$-vector and the vertical plane along the beam axis and no tracks with large transverse momenta point to the calorimeter crack ($\Delta\phi < \pm 5°$ relative to the vertical plane) are suited for a valid measurement of the neutrino transverse momentum. In UA1, the transverse components of $\vec{\not{p}}_T$ are gaussian distributed and give a resolution in $\not{p}_T$ of $\sigma(\not{p}_T) = 0.7 \cdot \sqrt{\Sigma E_T}$ (ΣE_T in GeV). The $\not{p}_T$ resolution is shown in Fig. 6a as a function of σ^2.

The old UA2 detector did not have any calorimetry below $\theta < 20°$, and no HAD calorimetry between $20° < \theta < 40°$. This caused non-gaussian tails in the determination of $\not{p}_T$. Nevertheless, for large $\not{p}_T$ a sufficient rejection of background was obtained to observe the reaction $W \rightarrow e\nu$ with high efficiency. The upgraded UA2 has now a substantially improved measurement of $\vec{\not{p}}_T$, because of the enlarged EM and HAD calorimetry without

acceptance losses in azimuth and a $5° < \theta < 175°$ coverage in polar angle. The $\not{p}_T$ resolution ($\Delta = \sqrt{2}\,\sigma$) parameterized as a function of ΣE_T is shown in Fig. 6b. On average, minimum bias events are more spherical and uniform than the underlying events from W and Z production. Therefore the resolution measured from minimum bias events can be taken as a lower limit of the true resolution. Two-jet events, on the other hand, show a higher complexity in the underlying events than W events. Therefore two-jet data can be used to obtain an upper limit for the $\not{p}_T$ resolution. In this case the value of ΣE_T represents the remaining sum of transverse energy after contributions from the two jets have been removed. These limits are shown as lower (open circles) and upper (full circles) curves in Fig. 6b, respectivly. The $\not{p}_T$ resolution is taken as the mean of the minimum bias and two-jet resolutions and is parametrized by
$\sigma(\not{p}_T) = [0.818 \cdot (\Sigma E_T)^{0.423} + 1.290 \cdot (\Sigma E_T)^{0.351}]/2$ (ΣE_T in GeV).

CDF measures the missing transverse momentum by summing the transverse energies over all EM and HAD calorimeter towers in the range of $|\eta| \leq 3.6$. Due to shower fluctuations and calorimeter response, the $\not{p}_T$ resolution is $\sigma(\not{p}_T) \sim 0.66 \cdot \sqrt{\Sigma E_T}$ (ΣE_T in GeV). Due to calorimeter non-linearities and cracks the $\not{p}_T$ measurement has to be corrected in a similar way as the jet energies (see Sections 3.2 and 3.3). The correction is made in conjunction with the jet energy correction and uses the following relation

$$|\vec{p}_T^{\,\nu}| \equiv |\vec{\not{p}}_T(\text{corrected})| = \not{E}_T = -\Sigma E_T^e - \Sigma E_T^{jet}(\text{corrected}) - k_\mu \cdot |\vec{p}_T^{\,ue}|, \qquad (5)$$

where $|\vec{p}_T^{\,ue}|$ is the vector sum of transverse energies over all calorimeter towers for the underlying event. The constant k_μ is an overall correction of the non-linear response of the calorimeter for the underlying event. All energy seen in the event which is neither accounted for by an electron nor by jets is attributed to the underlying event. The correction factor k_μ is obtained by minimizing the width of the $\not{p}_T$ distribution. Using the Z and jet samples, k_μ was found to be 1.4 for $\Sigma p_T^{hadrons} > 30$ GeV/c. The $\not{p}_T$ resolution as a function of ΣE_T is shown in Fig. 6c.

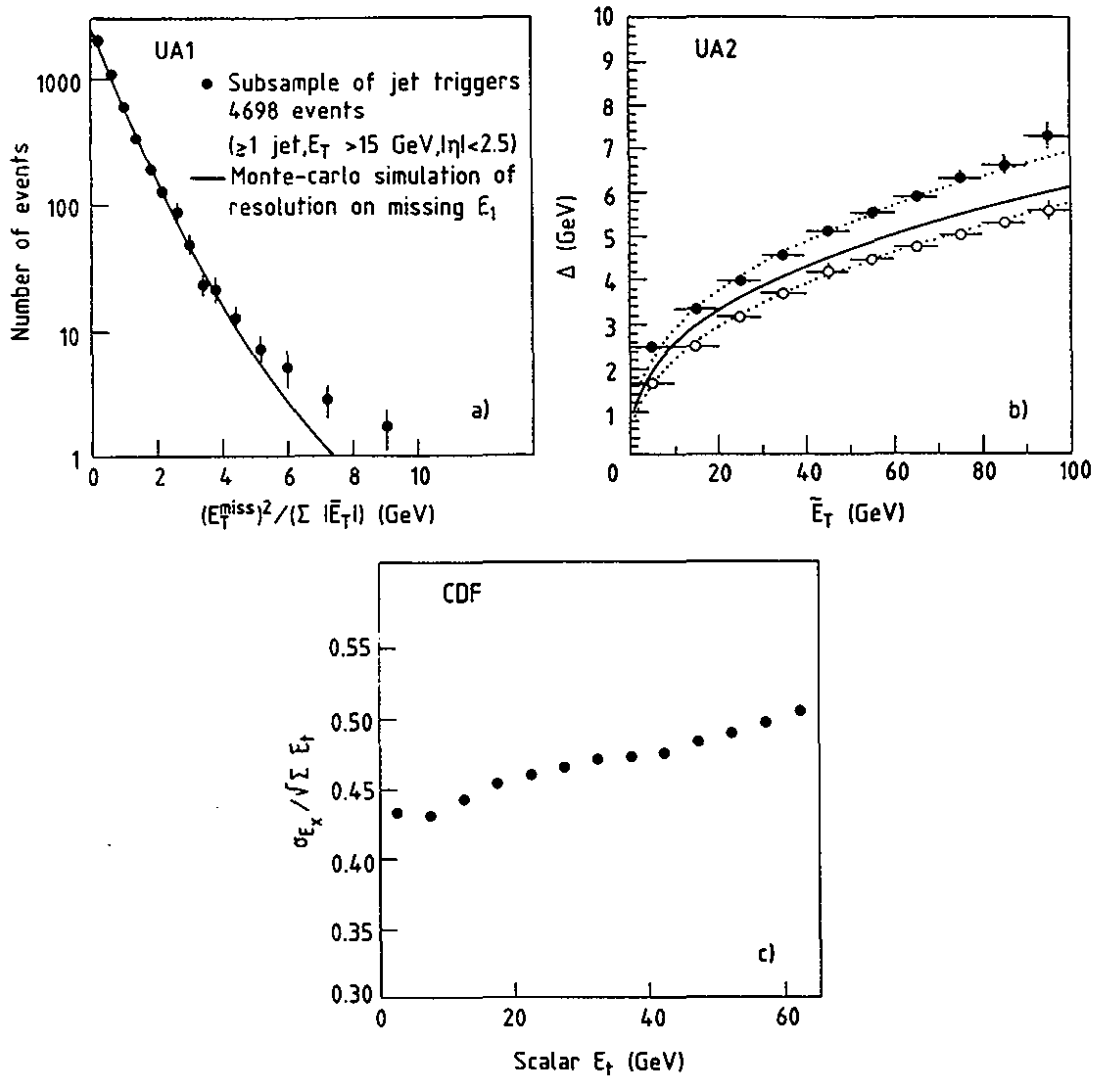

Figure 6
Resolution function of the $\not{p}_T$ measurement as a function of ΣE_T
a) for UA1 b) for UA2 c) for CDF

As can be seen from Fig. 6 all three experiments have studied the $\not{p}_T$ resolution carefully, parametrized the result which then has been used in tuned models to describe the detector response. The measured p_T^W distribution is shown in Fig. 7a and 7b for the UA2 and CDF experiments, respectively. The theoretical prediction convoluted with the tuned model of the detector response has been superimposed to the experimental distribution. UA2 uses somewhat conservative bounds of the p_T^W resolution indicated by the dotted lines in Fig. 7a.

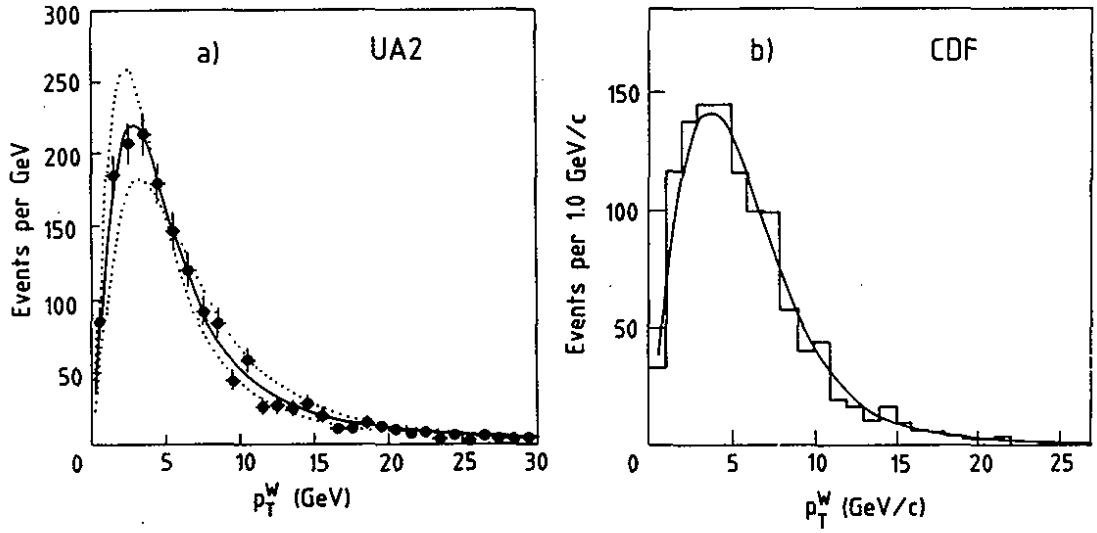

Figure 7
p_T^W distribution with the detector response superimposed

3.1.4 Tau identification

The decay $W \rightarrow \tau\nu_\tau$, $\tau \rightarrow \nu_\tau$ + hadrons is expected to result in purely hadronic events with large missing transverse momentum, $\not{p}_T$, due to the undetected neutrinos. The branching ratio to hadrons for τ decays is approximately 64% as compared to the 18% branching fractions to either an electron or a muon, and the fraction with five or more charged particles amounts to less than 1%. Therefore, the hadrons from τ decays appear as a highly collimated jet of moderate transverse energy with low charged particle multiplicity (one or three), and each hadron is expected to carry a substantial fraction of the jet transverse energy.

UA1 has presented a $W \rightarrow \tau\nu_\tau$ signal from the 1982 - 1985 data corresponding to an integrated luminosity of ~ 0.75 pb^{-1} [21]. After very restrictive cuts for background suppression the final tau sample contained 32 events. The overall efficiency to detect taus was about 7%.

UA2 has made a tau analysis restricted to the central region ($|\eta| < 0.8$) from the 1988 - 1989 data sample corresponding to an integrated luminosity of 7.4 pb^{-1} using the following cuts :

a) the $\not{p}_T$ in the event was required to exceed 25 GeV/c,
b) there should be at least one cluster with transverse energy of $E_T > 10$ GeV,
c) there should be at least one track in a 10° cone pointing to the cluster.

Two more variables have been defined to reduce the contributions from beam halo and to distinguish among the various fake contributions to the $W \rightarrow \tau\nu_\tau$ data sample :

i) the hadronicity, $HR = E_{HAD}/E_{TOT}$, where E_{HAD} is the cluster energy in the first and second hadronic compartment and E_{TOT} is the total energy of the cluster, is expected to be less than 90% to reject the beam halo and

ii) the profile, $PR = (E_1 + E_2)/E_{TOT}$, where E_1 and E_2 are the energies of the two most energetic cells in the cluster, is expected to be larger than 75%.

The number of tau events is extracted by likelihood fits to the profile and hadronicity distributions assuming that these distributions are known for taus, electrons and jets. An event sample of 235 $W \rightarrow \tau\nu_\tau$ decays has been selected in this way [22].

CDF has built a special hardware trigger designed to enhance the number of events containing a "tau-like" signature described above. In a subsequent analysis for the reaction $W \rightarrow \tau\nu_\tau$ from the τ - trigger ($\not{p}_T$-trigger) only events with :

a) $\not{p}_T > 20$ GeV/c (25 GeV/c) and

b) a "significance of missing E_T", S_{E_T}, greater than 2.4

are retained, where S_{E_T} is defined as

$$S_{E_T} = \frac{|\not{p}_T|}{\sqrt{E_{T'}}} \text{ with } E_{T'} = \sum_i E_i \cdot \sin\theta_i \qquad (6)$$

and the sum extends over all calorimeter towers. To suppress the enormous background from two-jet events in which one of the two jets has been significantly mismeasured, events were rejected if they contained at least one other calorimeter cluster with $E_T > 7$ GeV. "Tau-like" objects were searched by forming cones of 10° and 30° around the highest p_T track in the event, and all tracks of more than 1 GeV/c in the 10° cone were combined into a "track" cluster. Clusters with one or more tracks with $p_T > 1$ GeV/c in the region between 10° and 30° were rejected. In order to suppress events from the process $W \rightarrow e\nu$, clusters were also rejected if their ratio of hadronic to electromagnetic transverse energy was less than 20%. Finally, the transverse energy summed over all calorimeter towers within a region of 30° in azimuth and of 0.6 units in pseudorapidity surrounding the trajectories of the remaining clusters was required to be greater than 15 GeV. From studies of event samples with the above cuts, CDF makes a preliminary conclusion [23] that the events with a single, narrow, isolated jet appear to be significantly different from the background expected from QCD production of either light or heavy quarks. They have also indications that a mass peak of the charged ρ can be reconstructed from the single charged track combined with a single nearby neutral cluster as measured in the strip chambers in the tau data sample. No such an enhancement at the ρ mass is visible in a di-jet control sample (for details of the di-jet sample see Section 3.3)

3.2 Jet algorithms

Fragmentation of quarks and gluons results in a continuous hadronic energy flow known as hadronic "jets". The common definition of a "jet" is a cluster of particles with some limited momentum transverse to a central axis. In practice, jets are what a particular reconstruction algorithm in an experiment defines them to be, and in particular the three experiments considered have developed slightly different jet algorithms, whose use depends mainly on the physics question to be addressed. Of equal importance for the detection of jets is the energy measurement of the fragmentation products with well understood response and good resolution.

In UA1 jets are defined as clusters in the η - ϕ plane by the following procedure: an energy vector is associated to each calorimeter cell. For hadronic cells, the vector points from the interaction vertex to the centre of the cell. For electromagnetic cells, the vector points to the energy centroid determined by the pulse height measurement (Gondolas) or by the position detectors (Bouchons). Among the cells with $E_T > 2.5$ GeV, the highest E_T cell initiates the first jet. Subsequent cells are considered in order of decreasing E_T. Each cell momentum is added in turn vectorially to the jet closest in η - ϕ plane with the smallest $\Delta R = \sqrt{(\Delta\eta^2 + \Delta\phi^2)} < 1.0$ (with ϕ given in radians). If there is no jet with $\Delta R < 1.0$, the cell initiates a new jet. Cell momenta with $p_T < 2.5$ GeV/c are finally added vectorially to the jet nearest in η - ϕ, if their transverse momentum relative to the jet axis is less than 1 GeV/c and if they are not separated by more than 45° from the jet axis.

In UA2 four different jet algorithms are used, a) a cluster algorithm, b) a cluster algorithm with merging, c) a window algorithm and d) a cone algorithm. Which one of the different algorithms is used depends on the particular physics question one is addressing. The cluster algorithm forms a cluster by joining all cells which share a common side and have a transverse energy deposition exceeding 400 MeV. A momentum vector with magnitude equal to the cluster energy is assigned to each cluster by joining the cluster centroid to the centre of the detector. The individual clusters are taken as massless. This basic cluster method provides a good two-jet resolution in space. However, the jet energy measurement is limited to the central core of the jet, which for a jet of 40 GeV transverse energy typically contains only 90% of the total jet energy. The merging algorithm improves the energy collection by merging clusters around a primary seed cluster. The window algorithm uses the transverse energy flow in a fixed jet aperture. The cell size of the UA2 central calorimeter suggests a rectangular window of dimensions 70° × 75° in the θ - ϕ plane. All energy deposited in that window is assigned to the jet. This algorithm overcomes the problem that low transverse momentum jets may deposit energy into cells

which are not included in the jet defined by the two algorithms above. Because of its fast execution time, this simple fixed-aperture jet algorithm has been used in the UA2 second level trigger decision with the advantage of reducing the trigger bias for low momentum jets. Finally, the cone algorithm uses a fixed cone with a cone size of $\Delta R = \sqrt{(\Delta\eta^2 + \Delta\phi^2)} < 0.64$ (ϕ given in radians) to collect the energy in that cone.

CDF has studied three basic jet definitions, based on a nearest neighbour algorithm, a transverse energy dependent cone algorithm and a fixed cone algorithm. Physics studies requiring good jet energy resolution favour the fixed cone algorithm, which has the additional advantage of being more directly applicable to QCD comparisons. The fixed cone algorithm has two stages, a preclustering stage and a stage where the preclusters are merged into clusters. In the preclustering stage, a list of towers with transverse energy $E_T > 1$ GeV is formed, and preclusters are defined as an unbroken chain of adjacent towers with continuously decreasing transverse energy. If the total E_T of a precluster is larger than 2 GeV it is used as a starting point for clustering. In the next stage the E_T-weighted centroid of the precluster is found. Then a fixed cone in the η - ϕ plane of radius 0.6 is formed around the centroid, and all towers with $E_T > 200$ MeV inside this cone are included. A new centroid is calculated from this set of towers. This process is repeated until the list of towers inside the cone remains unchanged in successive iterations. Finally, if two clusters overlap, they are merged if either cluster shares more than 50% of its energy with the other cluster, otherwise the clusters remain separate and towers common to both clusters are assigned to the nearest cluster. The cluster energy is defined to be the scalar sum of the energies in all associated towers. From the energy and the angle formed between the cluster centroid and the beam axis (θ), the jet transverse energy is defined as $E_T^{jet} = E \sin\theta$.

Jet energies have to be corrected for significant energy loss due to various detector effects, such as calorimeter cell boundaries, non-linear response, energy leakage and losses due to the jet algorithm. Three main effects, common to all experiments and related to the definition of a jet, require an energy correction: a) the additional energy from the underlying event, b) the energy leakage outside the cone, and c) the loss of jet energy due to cell or single tower threshold.

3.3 Detector calibrations

The calibration of the detectors of the three experiments (UA1, UA2 and CDF) is of significant importance for the different analyses. In particular, the W and Z mass

measurements depend critically on the alignment of the central tracking chambers for the momentum measurement (UA1 and CDF) and on the calibration of the electromagnetic calorimeters (all three experiments).

In UA1, the momentum accuracy for high-momentum tracks is limited by systematic errors on the chamber alignment (≤ 100 μm) and by diffusion of the drifting electrons (≤ 300 μm). This results in a momentum uncertainty of $\Delta p/p^2 = 0.005$ $(GeV/c)^{-1}$ for a track of 1 m length perpendicular to the magnetic field. The energy resolution for electrons and photons in the central electromagnetic (EM) calorimeters is $\Delta E/E \sim 15\%/\sqrt{E}$ (E in GeV), with a quoted energy-scale uncertainty of $\sim \pm 3\%$, and a cell-to-cell calibration uncertainty of $\sim \pm 3\%$. The energy is less well measured within ±15° of the vertical direction, because of the space taken by the light-guides of the EM calorimeter. Also the azimuthal granularity is rather poor because two particles separated by as much as 180° may hit the same gondola, in which case their individual energies cannot be measured separately. The resolution $\Delta E/E$ has deteriorated from $\approx 15\%/\sqrt{E}$ in 1983 to $\approx 21\%/\sqrt{E}$ in 1985 due to the decreasing light collection as the scintillator ages. The energy resolution for hadrons, together with the electromagnetic calorimeter placed in front has been measured in a test beam to be $\Delta E/E \sim 80\%/\sqrt{E}$ (E in GeV). For the 1988 - 1989 collider run the energy measurement relied on the hadron calorimeters alone. In addition the central drift chamber was operated in a new mode in order to cope with the higher currents resulting from the increased collider luminosity. These two effects resulted in a worse momentum resolution of $\Delta p/p^2 \approx 0.02$ $(GeV/c)^{-1}$.

In UA2, each calorimeter module has been calibrated with electron, pion and muon test beams of known momentum at different energies. Short-term changes in response are tracked with Co^{60} source measurements. Further control of the calibration is obtained by a periodic recalibration of some modules in a test beam. As an example, the calorimeter response from test beam measurements of 40 modules of the central calorimeter EM cells performed in summer 1989 is compared in Fig. 8 with those performed in summer 1986 after applying the Co^{60} source corrections. As can be seen from that figure, the Co^{60} source calibration follows the ageing of the calorimeter up to a level of 0.3% per year, despite a reduction of the calorimeter response due to ageing which amounts to ~ 5% per year and an additional similar reduction due to radiation damage. In addition, the energy response varies by about ±10% over the cell surface depending on the impact point. To correct for these effects a detailed model derived from test beam data has been developed. To optimize the energy resolution for single hadrons relative weight factors were defined for all compartments in order to compensate on average for the difference in response to EM and HAD showers. This weighting procedure is relevant for the EM and HAD shower

components of a single pion as well as for HAD jets being composed of charged pions and π^0's which decay into photons. The absolute energy calibration was determined to be within ~ 1% (~ 2%) for EM (HAD) showers, resulting in an absolute energy scale error of ~ 1.5% for a typical jet which deposits of ~ 50% of its energy into the EM and ~ 50% into the HAD compartment. Because each particle in a jet (jet fragment) usually carries only a small fraction of the parent parton momentum its energy measurement is rather sensitive to deviations from a linear behaviour of the calorimeter at low momenta. In summary, the energy resolution for electrons and photons is $\Delta E/E = 15\%/\sqrt{E}$ (E in GeV) in the central part ($|\eta| < 0.8$), $\Delta E/E = 30\%/\sqrt{E}$ in the edge cells and $\Delta E/E = (17\%/\sqrt{E} + 1\%)$ in the end-caps. The energy resolution, $\Delta E/E$, for single pions varies for the CC from 32% at 1 GeV to 11% at 70 GeV, approximately proportional to $E^{-1/4}$, wheras for the EC it can be described as $68\%/\sqrt{E}$ below 25 GeV and as $30\% \cdot E^{-1/4}$ above (E in GeV). Because of the improvement of the calibration system itself the systematic error on the energy scale was reduced to 1.0% in the CC [17], wheras for the EC it is 3%. In conclusion, the calorimeter deterioration makes the calibration monitoring difficult, but thanks to extensive calibrations UA2 has been able to control the absolute energy scale uncertainty of the central EM calorimeter to better than 1% over a period of more than 4 years.

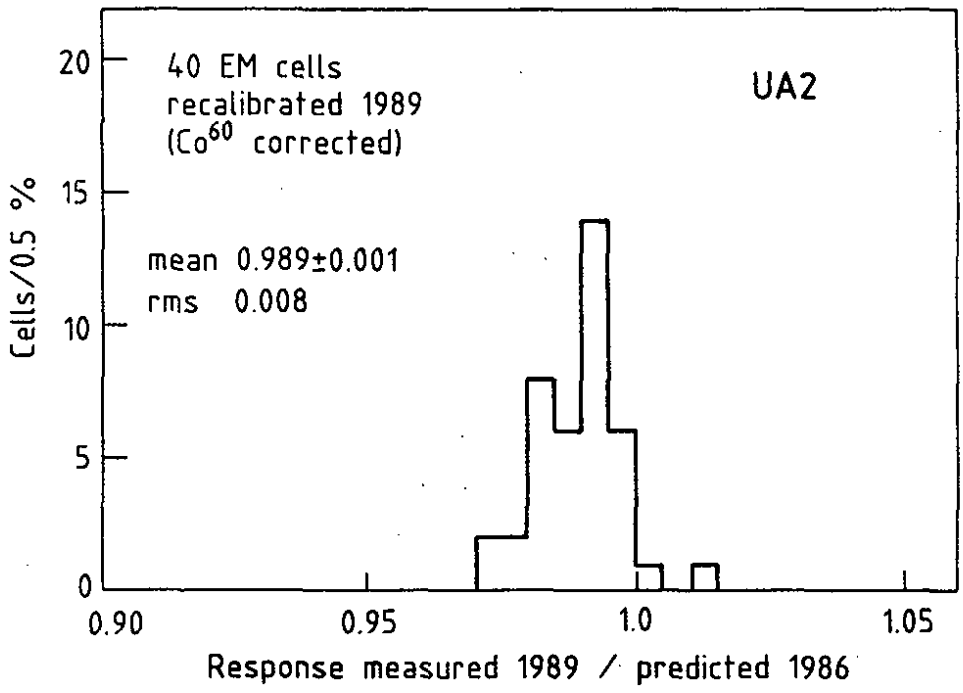

Figure 8
Response measured in summer 1989 over prediction from summer 1986

In CDF the calibrations involve the momentum scale for the central tracking chamber (CTC) and the energy scales for the EM and the HAD calorimeters.

i. The alignment of the CTC was adjusted using electrons from W decays such that the ratio of the track momentum to the calorimeter energy was charge independent. Constraining the W - decay tracks to come from the beam axis gives a measured resolution of the CTC of $\Delta p_T/p_T^2 = 0.0011$ (GeV/c)$^{-1}$. The CTC alignment and the magnitude of the magnetic field were verified by studying $K_S^0 \rightarrow \pi^+\pi^-$, $J/\Psi \rightarrow \mu^+\mu^-$ and $\Upsilon(1S) \rightarrow \mu^+\mu^-$ decays [24]. Vertex constraints were applied to the latter two data samples. The reconstructed J/Ψ mass (3.0963 ± 0.005 GeV/c^2) and Υ mass (9.457 ± 0.005 GeV/c^2) are shown in Figs. 9a and 9b. They agree well with the world average values, PDG [25], $[m_{J/\Psi}^{CDF} - m_{J/\Psi}^{PDG}] = -0.6 \pm 0.5$ MeV and $[m_{\Upsilon}^{CDF} - m_{\Upsilon}^{PDG}] = -3.3 \pm 5.0$ MeV. Based on these measurements the error on the energy scale is estimated to be less than 0.1% due to systematic momentum-scale uncertainties. Residual alignment errors have been checked with cosmic ray events.

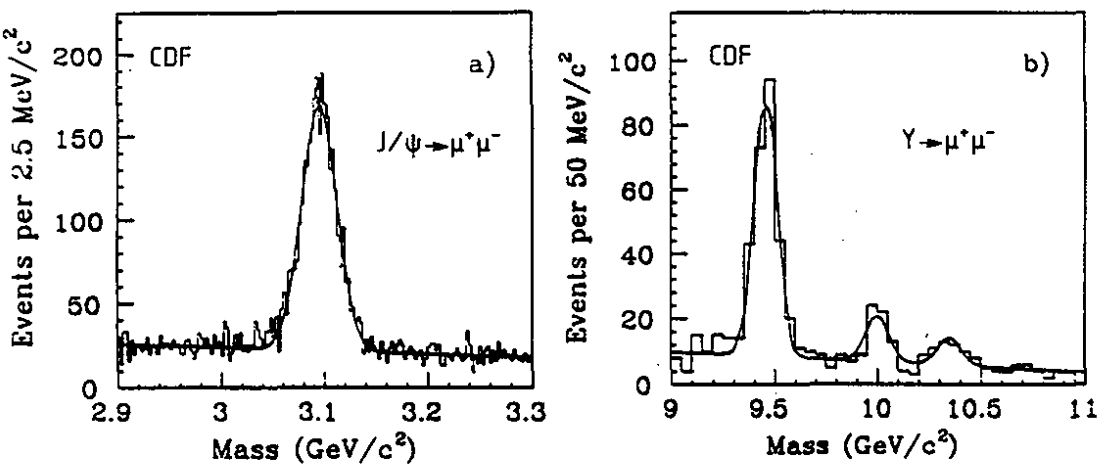

Figure 9
a) Invariant mass distribution of $J/\Psi \rightarrow \mu^+\mu^-$
b) Invariant mass distribution of $\Upsilon \rightarrow \mu^+\mu^-$

ii. The central EM (CEM) calorimeter was initially calibrated in a test beam. This calibration was found to be reproducible to ± 4% when towers were recalibrated after a period of one month. In situ energy - momentum matching has been used for energy scale calibrations [24]. A sample of 17000 inclusive electrons allows a relative cell-to cell calibration with an averaged statistical accuracy for each tower of 1.7% which

becomes a constant term in the energy resolution. The measured energy resolution is $(\Delta E/E)^2 = \{(13.5\%/\sqrt{E\sin\theta})^2 + (1.7\%)^2\}$ where the $\sin\theta$ factor reflects the fact that the sampling fluctuations increase when showers traverse the calorimeter at an angle different from normal incidence. Once the relative differences between towers have been removed, the overall energy scale was set by matching the predicted and measured E/p distributions for electrons from $W \rightarrow e\nu$ decays. The accuracy of this derivation of the energy scale from the momentum scale is $\pm$ 0.24%. Since the EM energy scale is derived from the momentum scale, uncertainties in the momentum scale will be common to both the calorimeter and the tracking mass scale.

iii. The energy scales for the plug and the forward EM calorimeters were verified using the Z mass peak from $Z \rightarrow e^+e^-$, where one of the electrons is in the central region. The plug calorimeter has an energy resolution for electrons and photons of $(\Delta E/E)^2 = \{(28\%/\sqrt{E})^2 + (2.0\%)^2\}$ (E in GeV). The systematic error on this calibration has been estimated from repeated test beam calibrations to be less than 3%.

iv. All HAD calorimeters have been calibrated with pion test beams. The response of the central HAD calorimeter has been studied using isolated charged pions from $\bar{p}p$ interactions. For the energy scale of the other HAD calorimeters the di-jet balancing technique was used. In di-jet events little transverse energy imbalance is expected. By studying di-jet events with one jet in the central calorimeter and the other in a gas calorimeter the relatively well known central energy scales are transferred to the gas calorimeters. Due to the non-linear response of the calorimeter for jets (including the effect of cracks, magnetic field and underlying event) the cluster energy has to be corrected to get the true parton momentum. It has been found for example that the observed jet transverse energy for $E_T^{jet} = 10$ GeV has to be multiplied by a factor of ~ 1.5. Such a correction is made as a function of the jet energy and the impact point on the calorimeter. This correction was checked using direct γ samples.

From the energy resolution $\Delta E/E$ quoted by the UA1, UA2 and CDF experiments to measure electrons in the EM calorimeters, a mass resolution $\Delta m/m$ can be deduced which corresponds to $\Delta m \approx 1.4$ GeV/c^2 for UA1 and UA2 and $\Delta m \approx 1.6$ GeV/c^2 for CDF for a mass $m \sim 90$ GeV/c^2 (i.e. for a $Z \rightarrow e^+e^-$ decay). In case of momentum measurement, the quoted momentum resolution can be translated into a mass resolution Δm which gives $\Delta m/m^2 = 7.1 \cdot 10^{-3}$ $(\text{GeV}/c^2)^{-1}$ for UA1 and $\Delta m/m^2 = 3.9 \cdot 10^{-4}$ $(\text{GeV}/c^2)^{-1}$ for CDF. For a track of 45 GeV/c momentum, which is typical of an electron from a $Z \rightarrow e^+e^-$ or a muon from a $Z \rightarrow \mu^+\mu^-$ decay, and with a direction perpendicular to the magnetic field, UA1 has now a measurement error of $\Delta p/p \sim 90\%$, corresponding to a mass resolution $\Delta m \approx 57$ GeV/c^2 which is worse by more than one order of magnitude compared to electrons measured in the EM calorimeter. In CDF, despite the beautiful

performance of the central tracking chamber with a high momentum resolution, the same example would give a measurement error of $\Delta p/p \sim 5\%$ with the vertex constraint resulting in a mass resolution of $\Delta m \approx 3$ GeV/c^2 for a single event, which still is about a factor of two worse than the calorimetric measurement.

Note that in case of momentum measurement $\Delta m/m$ increases linearly with m whereas for calorimetry $\Delta m/m$ decreases as $m^{-1/2}$, which is a strong argument for the use of the electron channel in searching for possible new particles with masses larger than those of the IVBs.

4. THEORETICAL PREDICTIONS OF THE STANDARD MODEL

In this section the main predictions of the Standard Model (SM), obtained without using $\bar{p}p$ collider data, are summarized for later comparison with the collider data.

4.1 The W and Z masses

The SM of the electro-weak interactions based on the SU(2) x U(1) gauge group has four independent parameters (if one ignores the Higgs and Fermion masses and the Kobayashi-Maskawa matrix elements). Expressed in a physical choice of the parameters these are

α, G_F, m_W and m_Z,

which are the fine structure constant, the Fermi coupling constant, and the masses of the W and Z bosons.

If the Higgs-sector of the theory is sufficiently simple (i.e. it consists of a limited number of SU(2) doublets of Higgs fields) an additional relation between the boson masses can be defined. According to the Sirlin renormalization scheme [26] extended to a non-minimal electroweak theory, the W and Z masses are related to the parameters of the SM in the following way

$$\sin^2\theta_W = 1 - \frac{m_W^2}{\rho \cdot m_Z^2} \qquad (7)$$

with θ_W being the electro-weak mixing angle or Weinberg angle, which is used to define the mixing of neutral fields and ρ being a parameter, which defines the relative strength of the charged and the neutral weak couplings in the effective Hamiltonian. The simplest theory, the Minimal Standard Model (MSM), has only one complex Higgs doublet, which manifests itself as a single physical Higgs particle, H^0, after spontaneous symmetry breaking. In this MSM the parameter ρ is identical to unity, but in case of a more complex Higgs sector it can be different from unity.

The fine structure constant α can be defined by the Thomson cross section,

$$\sigma_{Thomson} = \frac{8\pi\alpha^2}{3m_e^2} \quad , \tag{8}$$

with m_e being the mass of the electron, and is related to the electric charge e by $e^2 = 4\pi\alpha$. It has been precisely determined from the electron magnetic moment anomaly (g-2). The Fermi coupling constant G_F sets the Fermi scale and is related to the vacuum expectation value v of the Higgs field by $G_F^{-1} = \sqrt{2}v^2$. G_F itself is defined by the muon lifetime at a scale of $Q^2 \approx 0$,

$$\Gamma(\mu \rightarrow e\bar{\nu}_e\nu_\mu) \approx \frac{m_\mu^5 \cdot G_F^2}{192\,\pi^3} \cdot [1 - \frac{8m_e^2}{m_\mu^2}\{1 + \frac{\alpha}{2\pi} \cdot (\frac{25}{4} - \pi^2)\}] \tag{9}$$

with m_e and m_μ being the masses of the electron and the muon, respectively. From existing data the fine structure constant α at $Q^2 = m_e^2$,

$$\alpha^{-1} = 137.0359895 \pm 0.0000061 \tag{10}$$

and the Fermi coupling constant G_F

$$G_F = (1.16637 \pm 0.00002) \cdot 10^{-5}\ GeV^{-2} \tag{11}$$

are known with very high accuracy [25]. Therefore, we only have to deal with two unknowns, which can be any pair combination of m_W, m_Z, $\sin^2\theta_W$.

The previous discussion only included predictions at the tree level. Since the theory is renormalizable, corrections from higher orders, which contain virtual loops, will modify the predictions at the tree level. These effects have been calculated for the MSM ($\rho \equiv 1$) at

lowest order [27] in the renormalizable scheme given by Ref. [26], which is defined by the relation

$$\sin^2\theta_W \equiv 1 - \frac{m_W^2}{m_Z^2} \tag{12}$$

In this minimal scheme the predictions of the masses of the W and Z bosons [28] appear in the following form

$$m_W^2 = \frac{A^2}{(1 - \Delta r)\sin^2\theta_W} \tag{13}$$

$$m_Z^2 = \frac{A^2}{(1 - \Delta r)\sin^2\theta_W \cos^2\theta_W}, \tag{13'}$$

where A is defined by

$$A^2 = \frac{\pi\alpha}{\sqrt{2}\, G_F} \tag{14}$$

and has been computed to be

$$A = 37.2805 \pm 0.0003 \text{ GeV} \tag{14'}$$

using the experimental measurements of α and G_F given above.

The variable Δr stands for the radiative corrections to order α, which come from the loops in the gauge boson propagator and correspond to the evolution of α from low energy ($Q^2 \approx 0$) to $Q^2 = m_W^2$ or $Q^2 = m_Z^2$. The value of Δr is not yet known from experimental data and has to be calculated theoretically. Three different contributions have to be considered in the calculation of Δr, namely those from the Higgs - and gauge boson loops, those from the leptonic loops and those from the hadronic contributions of the quark loops [29]. This has the consequence that the value of Δr depends only weakly on the Higgs mass [$\sim \ln (m_H^2/m_Z^2)$], but strongly on the mass of the top-quark, m_{top}, [$\sim m_{top}^2/m_W^2$]. For a value of $m_{top} = 100$ GeV/c^2 and $m_H = 100$ GeV/c^2 Δr is calculated [30] to be

$$\Delta r = 0.0574 \pm 0.0013, \tag{15}$$

while Δr nearly vanishes for a mass of the top-quark, $m_{top} \sim 200$ GeV/c^2 ($\Delta r = 0.0187 \pm 0.0013$). The mass of the top-quark being unkown the radiative corrections cannot be tested in principle, but the relation given above can be used to determine boundaries to the mass of the top-quark.

The missing unknown is the value of the electro-weak mixing angle, $\sin^2\theta_W$. This can be determined by experiment and renormalized to the appropriate mass scale, in our case at $Q^2 = m_W^2$ or $Q^2 = m_Z^2$. A rather accurate determination of $\sin^2\theta_W$ comes from a recent comprehensive fit to all existing data from deep-ineleastic neutrino-scattering experiments [31]. The value of $\sin^2\theta_W$ is extracted from the ratio of neutral-current to the charged-current cross section. The major source of uncertainty in this ratio is the charm-quark mass, since the charm-quark contributes to the charged-current and not to the neutral-current. The contribution of this uncertainty has been estimated by leaving the mass of the charm-quark, m_c, free in the full fit. This gives an additional systematic error of 0.0043, which has been added in quadrature (see Ref. [31]). Using the value of $m_c = 1.5$ GeV/c^2 an average value of

$$\sin^2\theta_W = 0.2309 \pm 0.0029 \pm 0.0049 \qquad (16)$$

has been determined, with the first error being the experimental and the second error the combined theoretical uncertainty.

As an example, assuming 100 GeV/c^2 for the mass of the top-quark as well as for the Higgs mass, theory predicts within the MSM the following values for the masses of the W and Z bosons, m_W and m_Z, using the relations (7) to (16) and the experimental inputs from α, G_F and $\sin^2\theta_W$

$$\begin{aligned} m_W &= 79.95 \pm 0.99 \text{ GeV}/c^2 \\ m_Z &= 91.17 \pm 0.79 \text{ GeV}/c^2, \end{aligned} \qquad (17)$$

where the error is dominated by the uncertainty on the weak mixing angle $\sin^2\theta_W$. No uncertainties from the unknown masses of the top-quark and of the Higgs particle have been taken into account. Under the same assumptions theory predicts also a mass ratio, m_W/m_Z, of

$$\frac{m_W}{m_Z} = 0.8770 \pm 0.0032 \qquad (18)$$

reflecting just the relation of Eq. (12), and, often used by e^+e^- experiments, a mass difference, $m_Z - m_W$, of

$$\Delta m = m_Z - m_W = 11.22 \pm 0.30 \text{ GeV}/c^2, \qquad (19)$$

which provides another test of the SM by studying the correlation between m_W and $m_Z - m_W$. Note that the central value of Δm in Eq. (19) can be easily deduced from Eqs. (17) and (18), but because of the correlated errors of m_W and m_Z which cancel in the mass ratio the uncertainty on Δm is not trivial to calculate.

The predictions for the masses, the mass ratio and the mass difference can be checked by the $\bar{p}p$ collider experiments. Further measurements such as i) $\sin^2\theta_W$, or ii) the ρ parameter or iii) Δr can be performed from the experimental measurements of the W and Z masses. In particular, precise determination of the radiative corrections are of primary importance, because the value of Δr would be different from the theoretical value if a new fermion family with large mass splitting would exist or if the mass of the top-quark would be very large.

4.2 The W and Z partial and total widths

Having discussed the masses of the Intermediate Vector Bosons (IVBs), we can consider the rates of production and decay in $\bar{p}p$ collisions. Using the couplings of the SM we find that the leptonic decay modes have partial widths, Γ_W^ℓ and Γ_Z^ℓ, given by

$$\Gamma_W^\ell = \frac{G_F\, m_W^3}{6\pi\sqrt{2}} = 224 \pm 8 \text{ MeV}/c^2 \text{ and} \qquad (20)$$

$$\Gamma_Z^\ell = \frac{G_F\, m_Z^3}{24\pi\sqrt{2}} [(1 - 4\sin^2\theta_W)^2 + 1] = 83 \pm 2 \text{ MeV}/c^2, \qquad (21)$$

with $\Gamma_W^\ell = \Gamma(W \to \ell\, \nu_\ell)$ and $\Gamma_Z^\ell = \Gamma(Z \to \ell^+\ell^-)$ for $\ell = e, \mu, \tau$. For the numerical values the predicted W and Z masses (Eq. (17)) have been used. The partial width of the hadronic decay mode of the W boson, Γ_W^h, can be expressed in terms of the Γ_W^ℓ as

$$\Gamma_W^h = 3 \cdot 2 \cdot \Gamma_W^\ell \cdot K_{QCD} = 1388 \pm 50 \text{ MeV}/c^2 \qquad (22)$$

with $\Gamma_W^h = \Gamma(W \to \text{hadrons})$, where the factor 3 arises from colour, the factor 2 stands for two families of massless quarks (therefore ignoring any contribution from a top-quark), and the factor $K_{QCD} = \{1 + \alpha_s(Q^2)/\pi + 1.411 \cdot \alpha_s^2(Q^2)/\pi^2\}$ at $Q^2 = m_W^2$ takes into

account QCD effects which enhance the hadronic partial width compared to the leptonic one by ≈ 4%. The partial width of the neutrino decay mode of the Z boson, Γ_Z^ν, is given by

$$\Gamma_Z^\nu = \frac{G_F\, m_Z^3}{12\pi\sqrt{2}} = 166 \pm 4 \text{ MeV/c}^2, \qquad (23)$$

for each light neutrino, with $\Gamma_Z^\nu = \Gamma(Z \to \nu_\ell \bar{\nu}_\ell)$. The partial width of the hadronic decay mode of the Z boson, Γ_Z^h, can be expressed in terms of Γ_Z^ν, and is given by the strength of the weak neutral couplings

$$\begin{aligned}\Gamma_Z^h &= 3\cdot\{2\cdot[(1-\tfrac{8}{3}\sin^2\theta_W)^2+1] + 3\cdot[(1-\tfrac{4}{3}\sin^2\theta_W)^2+1]\}\cdot\Gamma_Z^\nu\cdot K_{QCD} \qquad (24)\\ &= 1731 \pm 42 \text{ MeV/c}^2,\end{aligned}$$

with $\Gamma_Z^h = \Gamma(Z \to \text{hadrons})$ summed over 5 flavours, the u, d, s, c and b quarks (ignoring again any top-quark contribution), the factor 3 stands for colour and K_{QCD} at $Q^2 = m_Z^2$ has the same meaning as above. Under the assumption of three fermion families and three neutrino generations, $N_\nu = 3$, the total widths of the IVBs, Γ_W and Γ_Z, are then given by

$$\Gamma_W = \Gamma_W^h + 3 \cdot \Gamma_W^\ell = 2.059 \pm 0.074 \text{ GeV/c}^2 \quad \text{and} \qquad (25)$$

$$\Gamma_Z = \Gamma_Z^h + 3 \cdot \Gamma_Z^\ell + N_\nu \cdot \Gamma_Z^\nu = 2.478 \pm 0.060 \text{ GeV/c}^2 \qquad (26)$$

where the errors are mainly due to the uncertainties on the IVB masses. Correlations from the determination of the partial widths of the IVBs have been taken into account in the error evaluation of the total widths. From the total widths the branching ratios into the lepton channels, B_W^ℓ and B_Z^ℓ, are deduced to be

$$B_W^\ell = 10.86\% \quad \text{and} \qquad (27)$$

$$B_Z^\ell = 3.36\%,$$

respectively. From Eqs. (25) and (26) the ratio of the total widths of the W boson to the Z boson, Γ_W/Γ_Z, is computed to be

$$\frac{\Gamma_W}{\Gamma_Z} = 0.831 \pm 0.010. \qquad (28)$$

with the assumption of a heavy top-quark ($m_{top} > m_W$) and three neutrino generations.

4.3 The W and Z cross sections

The inclusive production cross sections are more difficult to compute since we cannot perform experiments with monoenergetic quark beams. In $\bar{p}p$ collisions we must therefore integrate over the fluxes of incident partons, imposing the condition that the total energy in the parton-parton centre-of-mass is equal to the IVB mass. For example, if the two partons have an initial momentum fraction x_1 and x_2 of their respective baryons, and the beam c.m.s. energy is $\sqrt{s}$, we require

$$x_1 x_2 s = m_{IVB}^2 , \tag{29}$$

where m_{IVB} is the mass of the Intermediate Vector Boson, if these are produced with no transverse momentum.

The quark-quark cross sections are simple to compute in leading order, where the initial transverse momenta of the quarks are zero, i.e. a typical subprocess is

$$u\bar{d} \rightarrow W^+, \tag{30}$$

whose cross section is given by (neglecting the W width)

$$\sigma(u\bar{d} \rightarrow W^+) = \sqrt{2} \cdot \pi \cdot G_F \cdot m_W^2 \cdot \cos^2\theta_C \cdot \delta(x_1 x_2 s - m_W^2) \tag{31}$$

with θ_C being the Cabibbo angle.

In order to compute the total production cross section, the density of all parton flavours at all x is required, and an integration over the total width, Γ_W or Γ_Z, must be performed. The best information on parton density functions comes from deep-inelastic lepton-scattering experiments [32]. In addition, one must include the contributions from higher-order diagrams which increase the cross section and complicate the calculation by giving transverse momenta to the colliding partons and to the IVBs. We have redone the calculation of Ref. [33] which includes full QCD corrections to order α_s using the mass values of the IVBs as given by Eq. (17) and a more recent set of proton density functions (DFLM) with the QCD scale factor Λ_{QCD} = 160 MeV [35]. In the calculation also partial QCD corrections to order α_s^2 from Ref. [34] have been included. With these inputs theory predicts the values given in Table 2 for the total production cross sections of the W and Z bosons at centre-of-mass energies of 630 GeV and 1.8 TeV with $\sigma_W = \sigma(\bar{p}p \rightarrow W + X)$ and $\sigma_Z = \sigma(\bar{p}p \rightarrow Z + X)$.

Table 2 : Theoretical predictions of the total W and Z cross sections

cross section	DFLM Λ_{QCD} = 160 MeV	Range
$\sqrt{s}$ = 630 GeV		
σ_W	6.488	5.864 - 7.157
σ_Z	2.015	1.822 - 2.175
$\sqrt{s}$ = 1.8 TeV		
σ_W	21.039	17.147 - 22.916
σ_Z	6.413	5.289 - 6.917
all cross sections are given in nb		

The ranges indicated in Table 2 are due to the structure function uncertainties and ambiguities in the Q^2 scale. For an evaluation of the theoretical uncertainties which amount to $\sim \pm 8\%$ at $\sqrt{s}$ = 630 GeV and to $\sim \pm 12\%$ at $\sqrt{s}$ = 1.8 TeV) 14 different sets of proton density functions [35,36,37] obtained from next-to-leading order calculations performed either in the $\overline{MS}$ or in the DIS regularisation scheme were used. These parametrisations take into account a reasonable variation of the ratio of the valence quarks, d_V/u_V, when considering all the available data sets. It should be pointed out that despite the fact that more and more contributions from sea quarks for which $u_{sea} = d_{sea}$ are expected as $\sqrt{s}$ increases and that therefore uncertainties in the d_V/u_V ratio should decrease, the predictions of the W and Z cross sections become more and more uncertain as $\sqrt{s}$ increases (i.e. at LHC energies $\sigma_{W,Z}$ varies by a factor of $\sim$ 2 [38]). These theoretical uncertainties become larger, due to larger differences in shape of the sea-quark distribution for the different sets of structure functions as $\sqrt{s}$ increases and also because the contributions of the u and d valence quarks are not so tiny as one would expect at higher energies. Due to the quality of the newly available data [39] from deep-inelastic lepton-nucleon scattering processes, from prompt photon production and from Drell-Yan processes which tightly constrain the different combinations of parton density functions, a variety of new sets of structure

functions has recently become available [37]. Altogether they do not at all reduce the theoretical uncertainties on the evaluation of the cross sections and related quantities. New sets of structure functions which then will hopefully reduce these uncertainties, should be obtained when results from HERA, which probe proton densities to much smaller momentum fractions of the partons (x_1, $x_2 \geq 10^{-4}$) and at much higher Q^2 values than present data, become available in the near future [40]. Earlier sets of structure functions performed to leading order evolutions only (i.e. Duke-Owens set 1 and 2, Eichten et al. [41]) which preferred large values of Λ_{QCD}, do not agree with the ratio of u and d quarks in the nucleon derived from present data and are therefore ignored.

Imposing the above values (see Eq. (27)) for the leptonic branching ratios, B_W^ℓ and B_Z^ℓ, the following partial cross sections can be calculated using the DFLM structure function set with $\Lambda_{QCD} = 160$ MeV

$$\sigma_W^\ell = 704 \text{ pb} \qquad \text{at } \sqrt{s} = 630 \text{ GeV} \tag{32}$$

$$\sigma_W^\ell = 2283 \text{ pb} \qquad \text{at } \sqrt{s} = 1.8 \text{ TeV}$$

and

$$\sigma_Z^\ell = 68 \text{ pb} \qquad \text{at } \sqrt{s} = 630 \text{ GeV} \tag{33}$$

$$\sigma_Z^\ell = 216 \text{ pb} \qquad \text{at } \sqrt{s} = 1.8 \text{ TeV}$$

with $\sigma_W^\ell = \sigma_W \cdot B_W^\ell = \sigma(\bar{p}p \to W + X \to \ell\nu_\ell + X)$ and
$\sigma_Z^\ell = \sigma_Z \cdot B_Z^\ell = \sigma(\bar{p}p \to Z + X \to \ell^+\ell^- + X)$ for $\ell = e, \mu, \tau$. These cross sections and decay branching ratios are sufficiently large to have made the detection of the IVB leptonic decays relatively straightforward at the CERN $\bar{p}p$ collider and are comfortably high at TEV-I energies. However, because of the much higher transverse motion of the W at $\sqrt{s} = 1.8$ TeV (p_T^W is about twice as high as at $\sqrt{s} = 630$ GeV), the Jacobian peak of the decay lepton is smeared out, thus making the statistical error on the W mass somewhat larger than at $\sqrt{s} = 630$ GeV for the same number of events. The more difficult experimental task of observing the hadronic decay modes of the IVBs is discussed in Section 5.4.

One may obtain more precise predictions for ratios of cross sections since the errors on the structure functions cancel to the extent that the quark subprocesses are the

same. For example, the dependence of the cross sections on the centre-of-mass energy is predicted to be

$$\frac{\sigma_W(\sqrt{s} = 1.8\ \text{TeV})}{\sigma_W(\sqrt{s} = 630\ \text{GeV})} = 3.25 \quad \text{and} \tag{34}$$

$$\frac{\sigma_Z(\sqrt{s} = 1.8\ \text{TeV})}{\sigma_Z(\sqrt{s} = 630\ \text{GeV})} = 3.17$$

with almost no theoretical errors.

Both the theoretical uncertainties in the cross sections and most of the experimental systematic uncertainties tend to cancel in the ratio of the cross sections at fixed centre-of-mass energies. The ratio of the cross sections in $\bar{p}p$ collisions for W production to that of Z production with subsequent decays into lepton-neutrino and lepton-lepton pairs can be expressed as

$$R = \frac{\sigma_W^{\ell}}{\sigma_Z^{\ell}} = \frac{\sigma_W}{\sigma_Z} \cdot \frac{\Gamma_W^{\ell}}{\Gamma_Z^{\ell}} \cdot \frac{\Gamma_Z}{\Gamma_W} \tag{35}.$$

Imposing the above values for σ_W^{ℓ} and σ_Z^{ℓ} the ratio R is predicted to be

$$R = 10.40\ ^{+\ 0.23}_{-\ 0.13} \qquad \text{at } \sqrt{s} = 630\ \text{GeV} \quad \text{and} \tag{36}$$

$$R = 10.59\ ^{+\ 0.22}_{-\ 0.27} \qquad \text{at } \sqrt{s} = 1.8\ \text{TeV}.$$

From R the ratio of the total widths, Γ_Z/Γ_W, can be extracted, since the ratio of the total production cross sections, σ_W/σ_Z, can be calculated from the proton structure functions and the ratio of the partial widths for leptonic decays, $\Gamma_W^{\ell}/\Gamma_Z^{\ell}$, are given by the SM couplings and the masses of the Intermediate Vector Bosons (see Eqs. (20) and (21)). With the same 14 sets of structure functions as used for the total cross section evaluation we get a theoretical uncertainty of $\sim \pm 3\%$ at $\sqrt{s} = 630$ GeV and of $\sim \pm 5\%$ at $\sqrt{s} = 1.8$ TeV for the ratio. Recent measurements from the SLC and LEP experiments [42] of the total width of the Z, Γ_Z, allow the calculation of the total width of the W, Γ_W, with a much smaller uncertainty than obtained by direct measurements (see Section 5.1.1). It could be pointed out that this method to determine Γ_W will probably remain the most precise one even when the study of W^+W^- pairs will become possible at LEP II.

5. EXPERIMENTAL RESULTS ON W AND Z PRODUCTION AND DECAY PROPERTIES

In this chapter the experimental measurements on the W and Z production and decay properties are presented, compared to the predictions of the SM given in the previous sections and possible deviations to the predictions from the Minimal Standard Model (MSM) are investigated.

The Intermediate Vector Bosons, $W^{\pm}$ and Z^{o}, have been first detected by the UA1 and UA2 collaborations at the CERN $\bar{p}p$ collider in 1983 [2]. Since then, in two more running periods until 1985 where the collider energy was increased from $\sqrt{s}$ = 546 GeV to 630 GeV, more data have been accumulated corresponding to a total integrated luminosity of 0.748 ± 0.060 pb^{-1} for the UA1 and of 0.910 ± 0.080 pb^{-1} for the UA2 experiment. By 1985 the two collaborations had collected together about 800 $W^{\pm}$ and 100 Z^{o} particles decaying semi-leptonically into $W^{\pm} \rightarrow \ell^{\pm}(\bar{\nu})$ and $Z^{o} \rightarrow \ell^{+}\ell^{-}$ (ℓ = e, μ, τ), respectively. These statistics allowed a direct test of the predictions of the SM by means of measurements of the IVB production properties, their masses, their widths, and their branching ratios [43, 44].

After the upgrade of the CERN $\bar{p}p$ collider, in three more running periods until 1989 a total integrated luminosity of 5.4 pb^{-1} in UA1 and of 7.8 pb^{-1} in UA2 has been collected. At the same time CDF at the FNAL $\bar{p}p$ collider has accumulated data for a total integrated luminosity of 4.7 pb^{-1} at a centre-of-mass energy of 1.8 TeV. Results on these data providing a substantial improvement on the precision of the SM parameters, have recently been published. The large increase in statistics was used to significantly improve the measurement of :

- The partial W and Z production cross sections, σ_W^{ℓ} and σ_Z^{ℓ}, by the UA1, the UA2 and the CDF experiments, giving a more precise comparison to the improved theoretical predictions which include full QCD corrections to order (α_s) and partial QCD corrections to order (α_s^2) (see Ref. [34]).

- The ratio R of W to Z production cross section, $\sigma_W^{\ell}/\sigma_Z^{\ell}$, by the UA1, UA2 and CDF experiments, allowing for the first time a precise determination of the total width of the W, Γ_W, by using the measured total width of the Z boson from SLC and LEP experiments.

- The significance of tests on lepton universality by the UA2 and CDF experiments. This has been done via a measurement of the ratio of the partial cross sections, $\sigma \cdot B$, for the various W and Z decay modes into electrons and taus and for CDF also into muons.

- The distribution of the transverse momenta of the IVB bosons, p_T^W and p_T^Z, by the UA2 and CDF experiments. This distribution is an important test of perturbative QCD, and any significant discrepancy between data and theory at high transverse momenta of the IVBs would indicate new physics beyond the SM. Furthermore, a detailed understanding of the p_T^W measurement is essential in order to obtain a precise determination of the W mass.

- The Z decay angular distribution by the CDF experiment, resulting in an independent measurement of the Weinberg angle, $\sin^2\theta_W$.

- The hadronic decay modes of the W and Z bosons by the UA2 experiment. This measurement serves a double purpose, as a check of the SM predictions and as a test-case for jet spectroscopy at future hadron colliders as a method to discover possible new heavy particles decaying to hadronic jets.

- The IVB masses, m_W and m_Z, by the UA2 and CDF experiments. The errors of the measured masses at the CERN collider are dominated by the systematic uncertainties on the energy scale, which are common to m_W and m_Z. Therefore precise tests of the SM can be made using the ratio m_W/m_Z, where these uncertainties cancel.

- The SM parameters such as the weak mixing angle $\sin^2\theta_W$, the ρ parameter and the radiative corrrections Δr from the precise measurements of the W and Z masses and their ratio by the UA2 and CDF experiment. The mass ratio can also be used to place lower and upper bounds on the mass of the top-quark within the MSM scheme.

- Finally, a firm lower limit on the top-quark mass has been placed from direct searches by the UA1, the UA2 and the CDF experiments.

A summary of these new measurements together with a discussion of their implications on the SM parameters are given in the next sections.

5.1 Inclusive W and Z production cross sections

The cross section times branching ratio for the inclusive IVB production, $\bar{p}p$ = W/Z + anything, followed by a W/Z leptonic decay, is obtained from the relation

$$\sigma_{IVB} \cdot B^{\ell}_{IVB} = \frac{N_{obs} - N_{bkd}}{\varepsilon \cdot \eta \cdot L}, \qquad (37)$$

where N_{obs} is the number of observed events, N_{bkd} is the number of background events, ε is the overall efficiency which includes trigger, selection, identification and reconstruction losses, η is the geometrical acceptance for the applied kinematical cuts and L is the integrated luminosity.

UA1 has made a new analysis of the muon channel only [45], based on an integrated luminosity of 4.7 pb^{-1} from the 1988 and 1989 $\bar{p}p$ collider runs to get a new measurement of the W and Z cross section. For the electron and the tau channels only measurements from the 1982 - 1985 $\bar{p}p$ collider runs are available [44]. UA2 has recently published a new W and Z cross section measurement [46] in the electron channel using the increased statistics from the 1988 and 1989 data taking periods, which correspond to a total integrated luminosity of 7.4 pb^{-1}. For CDF, the W and Z cross sections are taken from a recent report [47] based on the full statistics of the 1988 - 1989 data of 4.21 pb^{-1} which greatly improves the previous cross section measurements [48].

In UA1, as described in Section 2.1 and 3.3, the energy measurement for the 1988 and 1989 collider run relied on the hadron calorimeters alone. Furthermore, because the central drift chamber (CD) was operated in a new mode the momentum resolution was worsened to about $\Delta p/p^2 = 0.02$ $(GeV/c)^{-1}$. The limited CD resolution has the effect that the Jacobian peak expected for the transverse mass distribution of the muon-neutrino pair system, $m_T^{\mu\nu}$, is strongly distorted into a distribution where many W's are reconstructed at low transverse masses which is a region where large backgrounds from muons coming from semi-leptonic heavy flavour decays and from pion and kaon decays in flight are expected. To remove these backgrounds the following kinematical cuts have been applied : $p_T^{\mu} > 15$ GeV/c and $m_T^{\mu\nu} > 30$ GeV/c^2. Good track quality, track isolation, muon isolation ($\Sigma p_T < 10$ GeV/c in a cone with $\Delta R \leq 0.4$ and $\Sigma E_T < 5$ GeV in a cone with $\Delta R \leq 0.7$, where $\Delta R = \sqrt{(\Delta\phi^2 + \eta^2)}$ is a cone around the muon direction and the muon itself is excluded from the momentum and the energy sums) and a veto on events where jets are nearby or back to to back with the muon are also required. After these cuts a total of 305 events were retained which have been classified as good after scanning. After background subtraction from misidentified $Z \rightarrow \mu\mu$ and Drell-Yan events, from $W \rightarrow \tau\nu$

with subsequent $\tau \rightarrow \mu\nu\nu$ decay and from semileptonic decays of b and c quarks, $259 \pm 17(\text{stat}) \pm 7(\text{syst})$ $W \rightarrow \mu\nu$ events have been identified. In order to determine a W cross section a two parameter maximum likelihood fit of the signal and background has been done based on the shape of the $m_T^{\mu\nu}$ distribution. The result is shown in Table 3. For the Z sample similar cuts as the ones described in the W selection are applied on the first muon track. The second muon should exceed a transverse momentum of $p_T^{\mu} > 8$ GeV/c and have a muon isolation of $\sum p_T < 10$ GeV/c in a cone with $\Delta R \leq 0.4$ and $\sum E_T < 10$ GeV in a cone with $\Delta R \leq 0.7$. The effective mass of the muon pair system, $m_{\mu\mu}$, should exceed 50 GeV/c^2. With these cuts 60 events are retained after inspection, of which 2 ± 1 are expected from Drell-Yan pairs. The Z cross section measurement is also shown in Table 3.

In UA2 the $W \rightarrow e\nu$ events are selected from a sample of electron candidates satisfying the kinematical cuts $p_T^e > 20$ (15) GeV/c and $p_T^{\nu} = \not{p}_T > 20$ (15) GeV/c for electrons in the central (endcap) region, with an additional cut on the transverse mass of the electron-neutrino system, $m_T^{e\nu} > 40$ GeV/c^2, for electrons in the endcap region (EC). Fiducial cuts have been applied to the edge cells of the CC and to the EC calorimeter to reduce the background contribution from fake electrons and to ensure that the efficiencies can be well measured. A total of 1676 (365) events in the CC (EC) region survive these cuts. The acceptance for electrons from $W \rightarrow e\nu$ decays in the CC region, η_W, including the geometrical and the kinematic cuts, amounts to $(53.0 \pm 1.7)\%$ in the CC and $(8.9 \pm 0.8)\%$ in the EC region. The global electron reconstruction efficiency, ε_W, in the CC region is measured to be $\{64 \pm 1(\text{stat.}) \pm 1(\text{syst.})\}\%$ and $\{75 \pm 2(\text{stat.}) \pm 2(\text{syst.})\}\%$ in the EC region, respectively. These efficiencies have been obtained by tightening the kinematic cuts to get a background-free sample and relaxing the electron identification cuts, and by using extensive testbeam results. The background contribution to the $W \rightarrow e\nu$ sample is small and is essentially due to hadronic events from QCD processes. It is estimated to be $(1 \pm 1)\%$ in the CC and $< 5\%$ in the EC region. For a total integrated luminosity of 7.4 pb^{-1}, after background subtraction, corrections for geometrical acceptances and electron efficiencies the W production cross section is measured as given in Table 3, in good agreement with the previous measurements [43, 44]. An independent analysis by using data taken with a trigger based on the $\not{p}_T$ measurement only has also been performed giving essentially the same result providing a robust cross check on the detector performance and on the estimate of the overall efficiency. The Z sample is selected from events containing two or more EM clusters with an invariant mass above 40 GeV/c^2 in the CC-CC and CC-EC configuration. The invariant mass spectrum, m_{ee}, for events with both legs satisfying the calorimeter electron selection criteria already shows a clear peak in the Z region around 90 GeV/c^2. Above a mass of $m_{ee} = 76$ GeV/c^2, 169 events are found, using slightly looser electron identification cuts on one leg. The background

contribution to this sample is estimated to be less than 0.5% in the central and about $(3 \pm 2)\%$ in the forward region. The Drell-Yan and the γ^*Z interference contribution in that mass region is estimated to be 1.7%. After background subtraction, corrections for efficiencies and geometrical acceptance and taking into account the integrated luminosity, the Z production cross section is measured as given in Table 3, also in good agreement with the previous measurements [43, 44].

CDF has presented an analysis in the electron channels, $W \rightarrow e\nu$ and $Z \rightarrow e^+e^-$. The event selection for electron candidates follows the criteria described in Section 3.1.1. The kinematical cuts applied to the data sample are $p_T^e > 20$ GeV/c for the first electromagnetic cluster and $p_T^e > 10$ GeV/c if there is a second electromagnetic cluster in the event. Fiducial cuts have been applied to remove events close to edges and cracks. A cut on the missing transverse momentum $\not{p}_T > 20$ GeV/c has been made in case of a W candidate. In case of a Z candidate the cuts on the shower characteristics on the second cluster have been loosened. The Z mass range has been defined to $65 < m_{ee} < 115$ GeV/c^2. A total sample of 2688 W candidates and 271 Z candidates have been selected. The background to the W sample has been estimated as 254 ± 77 events resulting mainly from $W \rightarrow \tau\nu$ events (90 ± 10) with subsequent semileptonic τ decays, $Z \rightarrow e^+e^-$ events (54 ± 27), where the second electron has been lost in a crack, and dominantly from QCD background (102 ± 51) faking the electron signature. The background in the Z sample is small (3%) and amounts to 8 ± 4 events. The acceptance has been determined to $(35.3 \pm 1.5)\%$ for $W \rightarrow e\nu$ decays and to $(37.3 \pm 0.7)\%$ for $Z \rightarrow e^+e^-$ decays. The total efficiency has been estimated to $(77.7 \pm 3.0)\%$ in the central region including the efficiency for the vertex requirement in the W case and to $\sim (86 \pm 5)\%$ in the Z case.

The available partial IVB cross section measurements at $\bar{p}p$ colliders by the UA1 [44,45], UA2 [46] and the CDF [47, 48] experiments are summarized in Table 3. The first error reflects the statistical and the second error the systematic uncertainty. For UA1 and UA2 the errors are dominated by the large uncertainty on the total inelastic cross section measurement [49] which contributes to a uncertainty of 8% and 5%, respectively, in the luminosity determination. For CDF the uncertainties are dominated at present by the estimated accuracy of ±15% on the absolute luminosity of the TEV-I collider, therefore the errors on the cross section measurements of CDF are still large.

Table 3 : Partial W and Z production cross sections measurements

Reaction	UA1	UA2	CDF
	$\sqrt{s}$ = 630 GeV	$\sqrt{s}$ = 630 GeV	$\sqrt{s}$ = 1.8 GeV
$W \to e\nu$	580± 50±70*)	660±15±37	2060±40±130±310(Lumi.)
$W \to \mu\nu$	609±41±94		
$W \to \tau\nu$	580±130±90*,+)		
$Z \to e^+e^-$	68±14±7*)	70.4±5.5±4.0	197±12±10±30(Lumi.)
$Z \to \mu^+\mu^-$	58.6±7.8±8.4		

*) Values from 1985

+) Including data at $\sqrt{s}$ = 546 properly corrected for $\sqrt{s}$ = 630 GeV

all cross sections are given in pb

These measured partial W and Z cross sections are shown in Fig. 10 as a function of the centre-of-mass energy, $\sqrt{s}$. Also shown are the theoretical predictions, which are based on a recent QCD calculation [33] to order α_s and partial QCD corrections to order α_s^2 [34], with three neutrino generations and no top-quark contribution, using as input parameters the IVB mass values and the $\sin^2\theta_W$ value from Eqs. (16) and (17), respectively. The theoretical uncertainties indicated as a band have been obtained from a study using most of the presently available sets of parton distribution functions (14 different sets have been tested). These uncertainties amount to ~ ± 8% at $\sqrt{s}$ = 630 GeV and to ~ ± 12% at $\sqrt{s}$ = 1.8 TeV (see Section 4.3) and are therefore of the same order of magnitude as the experimental errors. The dependence on the values assumed for m_Z, m_W and $\sin^2\theta_W$ is small (~ ±1%). Within the statistical and the systematic uncertainties the measured values for the W and Z cross sections at CERN and at TEV-I energies agree well with theoretical predictions (see Eqs. (32) and (33)).

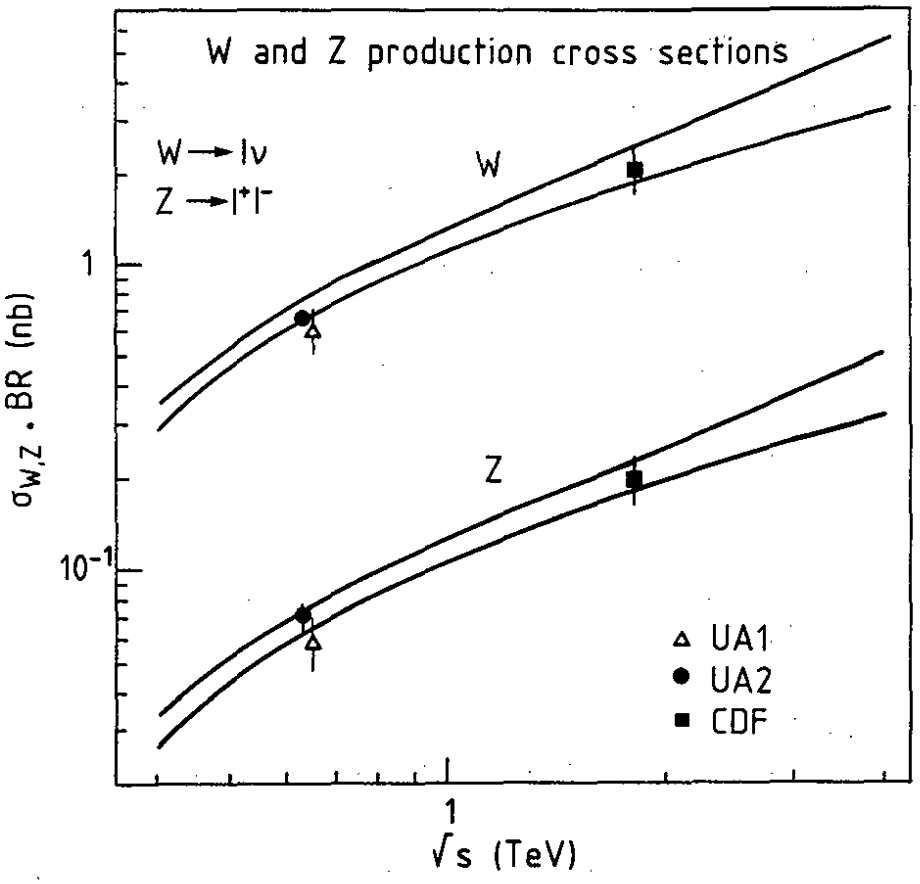

Figure 10

Partial W and Z cross sections, σ_W^{ℓ} and σ_Z^{ℓ}, as a function of $\sqrt{s}$

The increase of the W and Z boson cross sections with centre-of-mass energy $\sqrt{s}$ is measured to be

$$\frac{\sigma_W(\sqrt{s} = 1.8 \text{ TeV})}{\sigma_W(\sqrt{s} = 630 \text{ GeV})} = 3.12 \pm 0.55 \quad \text{and} \tag{38}$$

$$\frac{\sigma_Z(\sqrt{s} = 1.8 \text{ TeV})}{\sigma_Z(\sqrt{s} = 630 \text{ GeV})} = 2.80 \pm 0.55$$

which agrees within statistics with the theoretical expectations (see Eq. (34)).

5.1.1 Determination of Γ_W from the ratio of the W and Z production cross sections

While the cross sections σ_W^{ℓ} and σ_Z^{ℓ} are affected by large experimental and theoretical uncertainties, most of these uncertainties cancel in the ratio R (see Eq. 35):

$$R = \frac{\sigma_W^{\ell}}{\sigma_Z^{\ell}} = \frac{\sigma_W}{\sigma_Z} \cdot \frac{\Gamma_W^{\ell}}{\Gamma_Z^{\ell}} \cdot \frac{\Gamma_Z}{\Gamma_W}$$

The ratio R depends significantly on the top-quark mass, because for a mass of the top below 45 GeV/c^2 both decay channels $W \rightarrow t\bar{b}$ and $Z \rightarrow t\bar{t}$ are allowed, while for a top mass in the range $45 < m_{top} < 75$ GeV/c^2 only the decay $W \rightarrow t\bar{b}$ is allowed. For the UA1 [45] and UA2 [46] experiments the ratio R is computed from the W and Z partial production cross sections as given in the previous sections. For UA1 the recent measurement from the muon decay channel is used combined with the old result from the electron channel from the 1982 - 1985 data [44]. CDF [50] measures the ratio R directly by using the ratio of the number of observed W and Z events corrected for acceptance and efficiency losses. The recent measurement of R from the production cross sections [47] agrees well within errors. The ratio R of the W and Z partial production cross sections is summarized in Table 4 for the three experiments.

Table 4 : Ratio R of the W to the Z boson production cross section

Reaction	**UA1**	**UA2**	**CDF**
e-channel	$9.1\ ^{+1.7}_{-1.2}$ *,+)	$9.38\ ^{+0.82}_{-0.72} \pm 0.25$	$10.2 \pm 0.8 \pm 0.4$ 10.5 ± 0.7(stat.)++)
μ-channel	$10.4\ ^{+1.8}_{-1.5} \pm 0.8$**)		
combined	$(9.5\ ^{+1.1}_{-1.0}$ (stat + syst))		

*) Values from 1985 +) Electron and muon channels combined
**) Values from 1988/89
++) From the cross section ratio $\sigma_W^\ell / \sigma_Z^\ell$

The results from the three experiments are compared to the SM predictions. Most of the theoretical uncertainties, including the effect of higher order QCD corrections, are expected to cancel almost completely [33, 51] in the ratio R. The dependence of the ratio R as a function of $\sqrt{s}$ is shown in Fig. 11. The theoretical prediction shown as a band uses the same calculations already described in the previous section. Ignoring any top-quark contribution, the main uncertainties still come from the structure functions probing smaller and smaller x values as $\sqrt{s}$ increases, despite the fact that the effects of the uncertainties on the absolute values of the parton density functions cancel. The residual uncertainty is mainly due to the poor knowledge of the ratio of the valence density functions, d_V/u_V. The

theoretical uncertainty on R amounts to ≈ 3.4% at the CERN and to ≈ 4.6% at the TEV-I energy and increases to about 8% at LHC energies. Within the still large experimental uncertainties (about 8%) there is reasonable agreement with the theoretical predictions (see Eq. (36)), although the central value of all three recent measurements, as well as the old values from UA1 and UA2, are systematically below expectations.

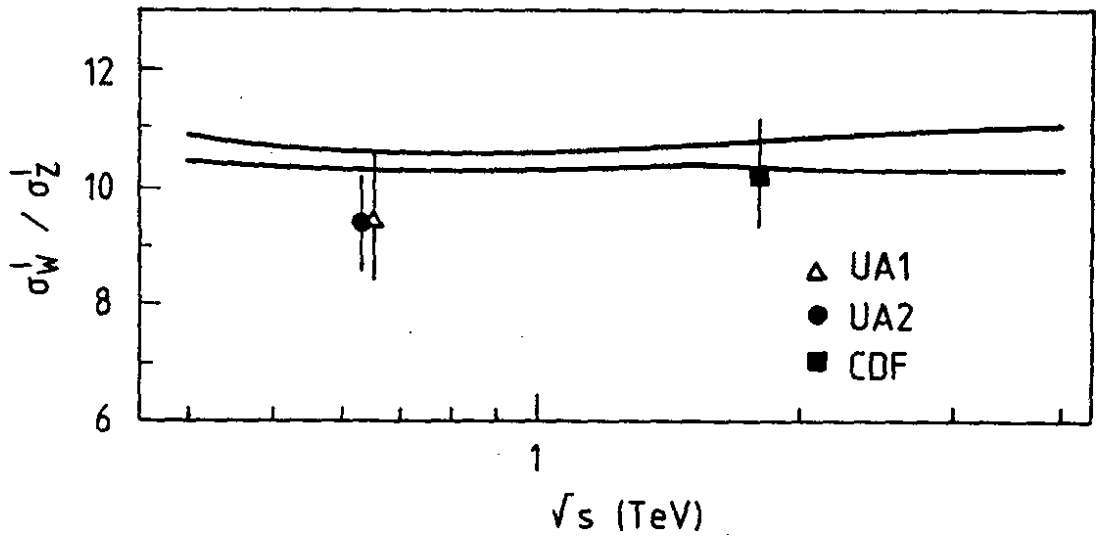

Figure 11
Ratio R as a function of $\sqrt{s}$

Within the context of the SM it is possible to use the observed value of R to extract a measurement of the total width of the W boson by inverting Eq. (35) to give a relation for the ratio of the total widths of the W to the Z boson

$$\frac{\Gamma_Z}{\Gamma_W} = \frac{\sigma_W}{\sigma_Z} \cdot \frac{\Gamma_W^\ell}{\Gamma_Z^\ell} \cdot \frac{1}{R} . \qquad (39)$$

The ratio of the total production cross sections, σ_W/σ_Z, are precisely calculable from the structure functions, and the ratio of the partial widths for leptonic decays, $\Gamma_W^\ell/\Gamma_Z^\ell$, are given by SM couplings and the masses of the IVBs alone (see Eqs. 20, 21 and 13, 13'). Note that these two ratios of the right hand side of Eq. (39) do not depend on the value assumed for the mass of the top-quark. Recent results from the SLC and LEP experiments [42] provide a measurement of the Z mass, m_Z, and its width, Γ_Z, to a precision of ~ 30 MeV/c^2. The weighted average of the LEP and SLC Z mass measurements including the current 30 MeV uncertainty on the LEP energy scale gives

$$m_Z = 91.177 \pm 0.031 \text{ GeV}/c^2, \tag{40}$$

and the weighted average of the total width of the Z boson gives

$$\Gamma_Z = 2.496 \pm 0.016 \text{ GeV}/c^2. \tag{41}$$

The individual measurement of m_Z and Γ_Z, together with their weighted average are shown in Figs. 12a and 12b. For the individual measurements only the experimental (statistical and mainly systematical) error is shown, whereas for the average value the LEP energy scale uncertainty is included.

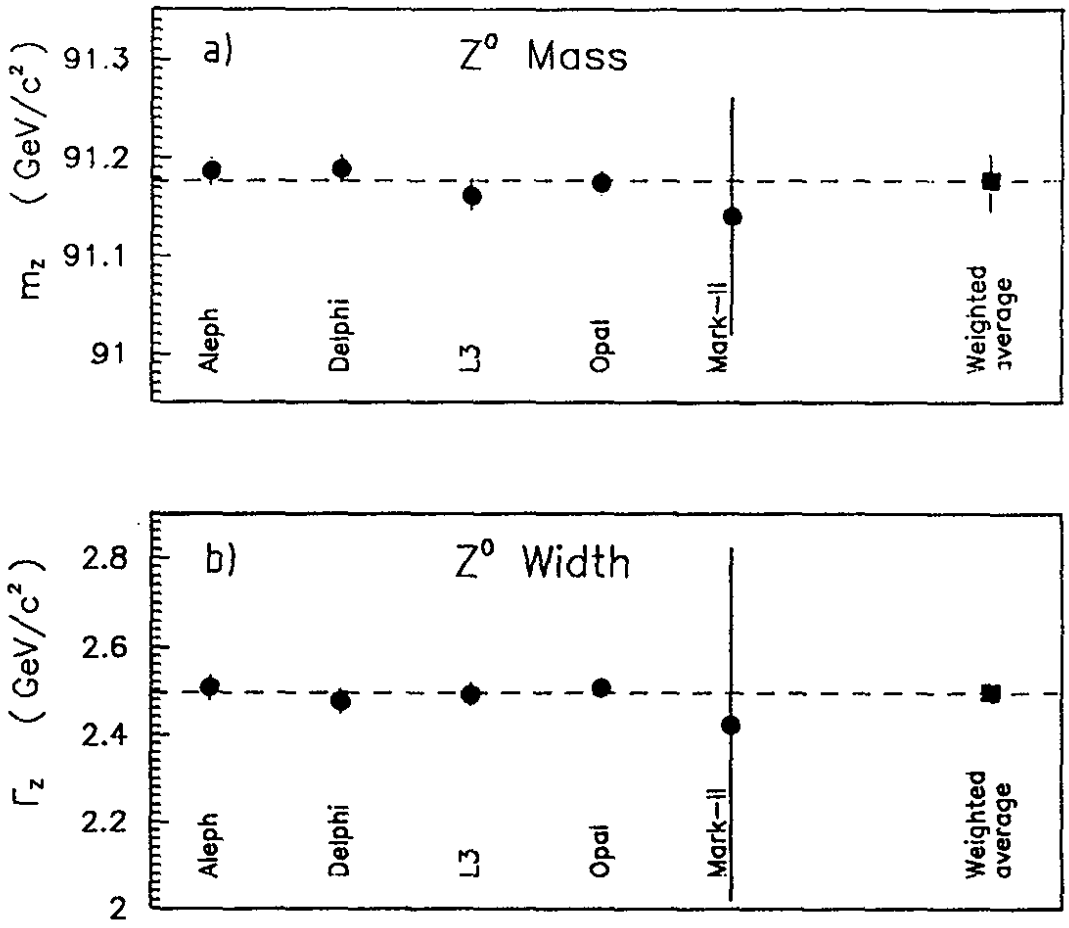

Figure 12

a) Measurement of the Z boson mass from LEP and SLC

b) Measurement of the Z boson width from LEP and SLC

Using the weighted average from LEP and SLC for m_Z, and a value for the mass ratio, m_W/m_Z, as measured by each of the $\bar{p}p$ collider experiments, fixing thereby the value of $\sin^2\theta_W$ (see Tables 9 and 11) for each experiment, the ratios $R_\sigma = \sigma_W/\sigma_Z$ and $R_\Gamma^\ell = \Gamma_W^\ell/\Gamma_Z^\ell$ have been computed based on the same QCD calculations as described in Section 5.1. Both the cross section ratio, R_σ, and the ratio of the partial leptonic witdhs, R_Γ^ℓ, depend on $\sin^2\theta_W$, explicitely through the neutral-current couplings and implicitly via the IVB masses. However, their product is constant to better than 1% over the range of $\sin^2\theta_W = 0.220 \pm 0.010$. A slightly larger uncertainty (~ 2.5%) results from the use of different sets of structure functions in the calculation of R_σ. The results of this calculation are shown in Table 5.

A value for Γ_W can be deduced from Eq. (39) using the weighted average of LEP and SLC results [42] for the total width of the Z boson. Recent results from the $\bar{p}p$ collider experiments on Γ_W are

$$\begin{aligned} &\Gamma_W = 2.19 \pm 0.20 \text{ (stat. + syst.) GeV/c}^2 && \text{from CDF [50],} \\ &\Gamma_W = 2.30 \pm 0.19 \text{ (stat.)} \pm 0.06 \text{ (syst.) GeV/c}^2 && \text{from UA2 [46] and} \\ &\Gamma_W = 2.18 \,{}^{+0.26}_{-0.24} \text{ (stat.)} \pm 0.04 \text{ (theory) GeV/c}^2 && \text{from UA1 [45]} \end{aligned} \qquad (42)$$

using the method described above. For UA1, because the combined electron and muon decay channels do not have similar systematic uncertainties the result should be taken with some care. All experiments have used different theoretical input assumptions for the evaluation of the cross section ratios, and different normalisation values for the total width of the Z boson. For consistency and to be able to compare the measurements we have derived a value of Γ_W from each experiment based on the input assumptions listed in Table 5, which uses for m_W and for $\sin^2\theta_W$ the value measured by each experiment but uses for the theoretical assumptions the same set of structure functions. We have convoluted properly the statistical and systematic uncertainties from the experimental R measurement and accounted for the theoretical uncertainties from R_σ and R_Γ^ℓ in a combined systematic error. The dependence of Γ_W/Γ_Z on the input assumptions is also shown in Table. 5 for the UA1, UA2 and CDF experiments.

Table 5 : Recomputed ratios of IVB cross sections, partial and total widths

cms energy	experiment	$\sin^2\theta_W$	$\frac{\sigma_W}{\sigma_Z}$	$\frac{\Gamma(W \to e\nu)}{\Gamma(Z \to e^+e^-)}$	$\frac{\Gamma_W}{\Gamma_Z}$
630 GeV	UA1+)	0.211±0.039	3.050±0.074	2.737±0.023	0.839±0.115
630 GeV	UA2	0.220±0.009	3.129±0.074	2.716±0.022	0.906±0.078
1.8 TeV	CDF+)	0.228±0.008	3.263±0.081	2.692±0.022	0.861±0.076

+) Electron and muon channels combined

Using the measured ratios Γ_W/Γ_Z from Table 5 and the weighted average from LEP and SLC for Γ_Z we obtain consistent measurements for Γ_W which are summarized in Table 6 for the three experiments. There is good agreement between all experiments.

Table 6 : Total width of the W boson, Γ_W

Reaction	UA1	UA2	CDF
e-channel	2.09±0.29(stat+syst)+)	2.26±0.18±0.06	2.15±0.17±0.09+)

+) Electron and muon channels combined

all widths are given in GeV/c^2

These three measurements of Γ_W can be statistically combined. To take into account the correlation through Γ_Z from LEP we have taken the weighted average of the statistical and experimental systematic uncertainty and convoluted the theoretical uncertainty on R_σ and R_Γ^ℓ to the total systematic error on the measured ratio Γ_W/Γ_Z from

the three experiments. The result is

$$\frac{\Gamma_W}{\Gamma_Z} = 0.875 \pm 0.050, \qquad (43)$$

where the error quoted is the statistical and systematic error added in quadrature. This measurement is in good agreement with theoretical expectations (see Eq. 28) for no top-quark contribution. Using Γ_Z from LEP [42] we then obtain for Γ_W

$$\Gamma_W = 2.184 \pm 0.124 \text{ GeV}/c^2 \qquad (44)$$

which is the best measurement of Γ_W with the present $\bar{p}p$ collider data. It is in good agreement with the MSM prediction without contribution from a top-quark (see Eq. (25)).

The measurement of Γ_W can be used as an indirect estimate on the mass of top-quark, m_{top}. In the SM the width of the W boson is expected to decrease from 2.8 GeV/c^2 to 2.1 GeV/c^2 as the mass of the top-quark is increased from zero to m_W. The dependence of Γ_W as a function of m_{top} is shown in Fig. 13. The measured values are in agreement with the SM expectations in case of a heavy top-quark, and are inconsistent with a light top-quark. From the measurement of Γ_W a lower limit on m_{top} can be deduced which is independent of any assumptions on the decay of the top-quark. The value obtained is

$$m_{top} > 52 \text{ GeV}/c^2 \qquad (45)$$

at the 95% confidence level.

5.1.2 Lepton universality

The ratios of the partial cross sections, $\sigma \cdot B$, for the various W and Z decay modes provide a unique test of the universality of the weak charged and neutral couplings to electrons, muons and taus at the scale $Q^2 = m^2_{IVB}$. This ratio has the advantage that it is not affected by uncertainties in the luminosity measurement. Defining the weak charged coupling constant g_i and the weak neutral coupling constant k_i for the ith lepton, we have

$$\frac{\sigma_W \cdot B(W \to \ell_i \nu_i)}{\sigma_W \cdot B(W \to \ell_j \nu_j)} = \left(\frac{g_i}{g_j}\right)^2 \qquad (46)$$

and

$$\frac{\sigma_Z \cdot B(Z \to \ell_i^+ \ell_i^-)}{\sigma_Z \cdot B(Z \to \ell_j^+ \ell_j^-)} = \left(\frac{k_i}{k_j}\right)^2 \qquad (47)$$

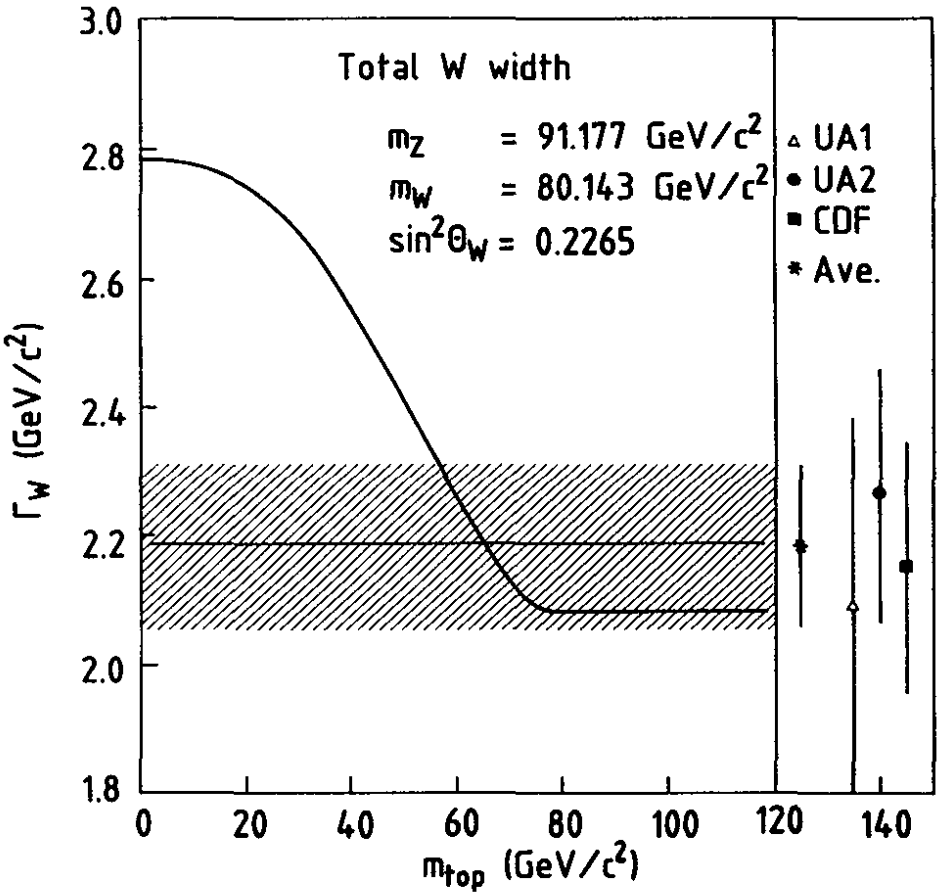

Figure 13

Total width of the W boson, Γ_W, as a function of the mass of the top-quark

All three expected leptonic decays of the W ($W \to \ell\nu$, ℓ = e, μ, τ) and Z ($Z \to \ell^+\ell^-$, ℓ = e, μ) decay modes have been seen and their cross sections have been measured by UA1 [41]. For the charged-current couplings UA1 has obtained the following results in combining the $\sqrt{s}$ = 546 GeV and $\sqrt{s}$ = 630 GeV data samples from the 1982 - 1985 collider runs

$$\frac{g_\mu}{g_e} = 1.00 \pm 0.07 \pm 0.07 \qquad (48)$$

$$\frac{g_\tau}{g_e} = 1.01 \pm 0.10 \pm 0.06,$$

and for the neutral-current couplings using $Z \to \mu^+\mu^-$ and $Z \to e^+e^-$ decays

$$\frac{k_\mu}{k_e} = 1.02 \pm 0.15 \pm 0.04, \qquad (49)$$

where the first error is the statistical and the second the systematic uncertainty. These

results provide a direct test for e-μ-τ universality at $Q^2 = m^2_{IVB}$. They are consistent with unity as expected in the SM to better than 15%.

UA2 has measured a cross section for the $W \rightarrow e\nu$ decay using the data from the 1988 and 1989 $\bar{p}p$ collider run and extracted a tau signal [22] as described in Section 3.1.4. The following preliminary results have been obtained for the charged-current couplings

$$\frac{g_\tau}{g_e} = 0.993 \pm 0.057 \pm 0.049 \qquad (50)$$

in good agreement with SM expectations.

CDF has electron and muon detection capabilities, and is able to identify taus with the method described in Section 3.1.4. An analysis on this subject is in progress, but no result has yet been announced from the CDF experiment.

The best measurement of lepton universality comes from the LEP experiments for the neutral-current couplings. All LEP [42] experiments have measured the leptonic partial width of the Z boson in the electron channel. ALEPH, DELPHI and OPAL have measured also those for the muon and tau channels. L3 measures those for the muon and tau channels correlated to the electron leptonic width. We have taken a weighted average for the electron, muon and tau partial widths whenever there was a published value available and calculated the ratios. Ignoring possible correlations among the partial widths we obtain the following values for the neutral-current couplings from the LEP experiments

$$\frac{k_\mu}{k_e} = 1.009 \pm 0.017 \qquad (51)$$

$$\frac{k_\tau}{k_e} = 0.996 \pm 0.019$$

which is consistent with lepton universality to better than 2%.

5.2 Inclusive W and Z transverse momentum spectra

While at leading order, the Intermediate Vector Boson production can be described by the Drell-Yan $q\bar{q}$ annihilation process, QCD corrections to the Drell-Yan mechanism result in a sizable IVB transverse momentum. The W and Z transverse momentum distributions provide therefore a good test of QCD. Any deviations from these predictions

yielding an excess of events at high p_T^{IVB} may be an indication of new physics processes. A detailed understanding of the p_T^W measurement is also essential, because it influences substantially the precision of the determination of the mass of the W, m_W. And finally, counting the number of jets produced in association with the Intermediate Vector Boson provides a measurement of α_S at the scale $Q^2 = m^2_{IVB}$.

The IVB transverse momentum, p_T^{IVB}, is obtained by adding the measured lepton ($\ell = e, \mu$) and the neutrino transverse momentum vectors in case of the W boson or by adding the measured lepton pair ($\ell^+ = e^+, \mu^+$ and $\ell^- = e^-, \mu^-$) transverse momentum vectors in case of the Z boson. As explained in Section 3.1.3 the neutrino transverse momentum is determined experimentally by the total transverse momentum vector of all recoiling hadrons in the event, $\vec{p}_T^{\,hadrons}$, measured in the calorimeters,

$$\vec{p}_T^{\,W} = \vec{p}_T^{\,\ell} + \vec{p}_T^{\,\nu} \cong - \vec{p}_T^{\,hadrons}, \qquad (52)$$

$$\vec{p}_T^{\,Z} = \vec{p}_T^{\,\ell^+} + \vec{p}_T^{\,\ell^-} \cong - \vec{p}_T^{\,hadrons}. \qquad (52')$$

There are two relevant ranges in p_T^{IVB}: the first, at moderate values of p_T, is dominated by multiple radiation of soft gluons; the second, in the region of large p_T, where contributions from processes like $q\bar{q} \rightarrow IVBg$ and $qg \rightarrow IVBq$ leading to IVB + jets in the final states are expected. Multiple radiation of soft gluons cannot be described by perturbative QCD and soft-gluon resummation techniques at all orders in α_S have been used [33]. At higher p_T, where perturbative QCD can be used, order α_S^2 calculations have been performed [52].

UA1 finds 357 $W \rightarrow \ell\nu$ events with an estimated background of 30 ± 5 events, and 51 $Z \rightarrow \ell^+\ell^-$ events with negligible background from the 1982-1985 data [44]. The p_T^W distribution peaks at a value of ~ 4 GeV/c, which primarily reflects the experimental resolution on the measurement of $p_T^{hadrons}$. The p_T^W distribution is shown in Fig. 14. The expected association of jet production at large p_T^W is observed in the data. There are two events at the highest p_T^W values, which contain a high-mass two-jet system recoiling against the W. Such a configuration is rather unlikely but not excluded as a standard QCD W + 2 jet event (event rates of 0.05 ± 0.03 events are expected). Within measurement errors, the values for the two-jet invariant mass, M(jj), are consistent with either m_W or m_Z, and also M(Wjj) is consistent with a unique value around 290 ± 30 GeV/c^2. It is tempting, therefore to interpret these events in terms of WW or WZ production. However, the production of pairs of gauge bosons by standard mechanisms is much too low to be observable with the statistics of the UA1 data sample (event rates in the most favourable production and decays of W^+W^- pairs of at most 0.001 event are expected).

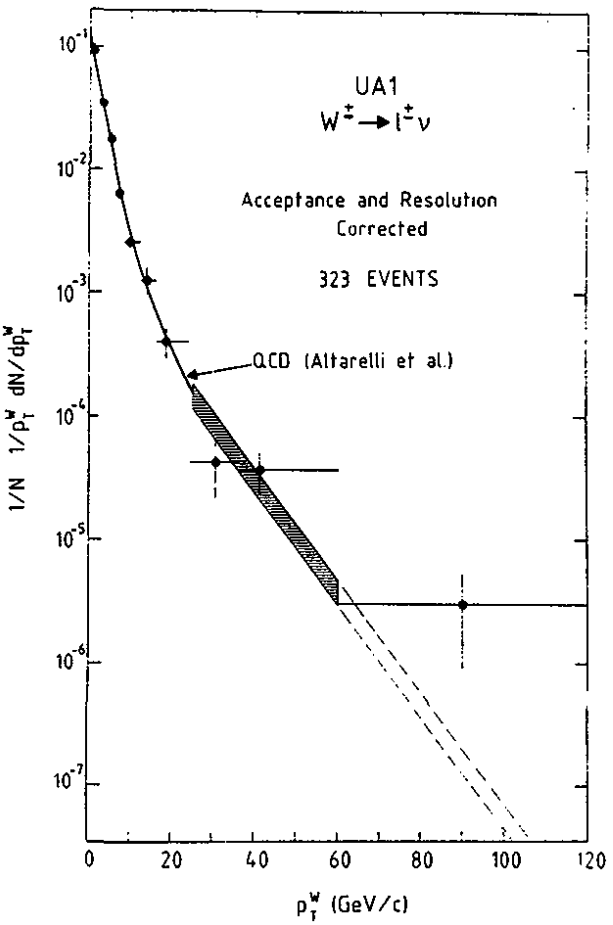

Figure 14
W transverse momentum distribution, p_T^W, from UA1

UA2 has made an analysis of p_T^W from the 1988 - 1989 data [53] which uses a sample of 1676 $W \rightarrow e\nu$ events with the decay electron detected in the CC region only, after releasing the fiducial cuts but with an additional transverse mass cut ($m_T^{e\nu} > 40$ GeV/c^2). The expected background from QCD processes amounts to less than 10 events. A comparison between experimental distributions and theory is performed by a Monte Carlo simulation which generates events according to theoretical predictions and then applies the effects of the detector response. The p_T^W resolution is derived from a study of the $Z \rightarrow e^+e^-$ sample, by comparing $(\vec{p}_T^{\,e^+} + \vec{p}_T^{\,e^-})$ with $\vec{p}_T^{\,hadrons}$ (see Eq. 52'). Fig. 15a shows the experimental p_T^W distribution below 30 GeV/c, together with the theoretical prediction (solid line) [33], where DFLM structure functions with $\Lambda_{\overline{MS}} = 160$ MeV and $Q^2 = m_W^2$ have been used [35], convoluted with an average detector response (see Section 3.1.3). Also shown is the range of uncertainties due to different sets of structure functions with larger $\Lambda_{\overline{MS}}$ values. All curves are normalized to the total number of observed events.

For $p_T^W > 20$ GeV/c, 83 events are observed. Fig. 15b shows the observed fraction of events as a function of p_T^W. The lower solid line represents the theoretical prediction of Ref. [51] with scale $Q^2 = m_W^2$, $\Lambda_{\overline{MS}} = 160$ MeV and DFLM structure functions. Other ranges of $\Lambda_{\overline{MS}}$ ($\Lambda_{\overline{MS}} = 360$ MeV) and other values for the scale ($Q^2 = p_T^2$) are barely distiguishable from the solid line. The upper solid line is a calculation of Ref. [54] with a somewhat extreme scale ($Q^2 = 0.25\ p_T^2$) showing that the theoretical and the experimental uncertainties are of the same order. The agreement between data and theory is good. It is especially interesting that the high p_T^W tail agrees well with recent order α_S^2 calculations, and shows no significant excess indicative of new physics processes.

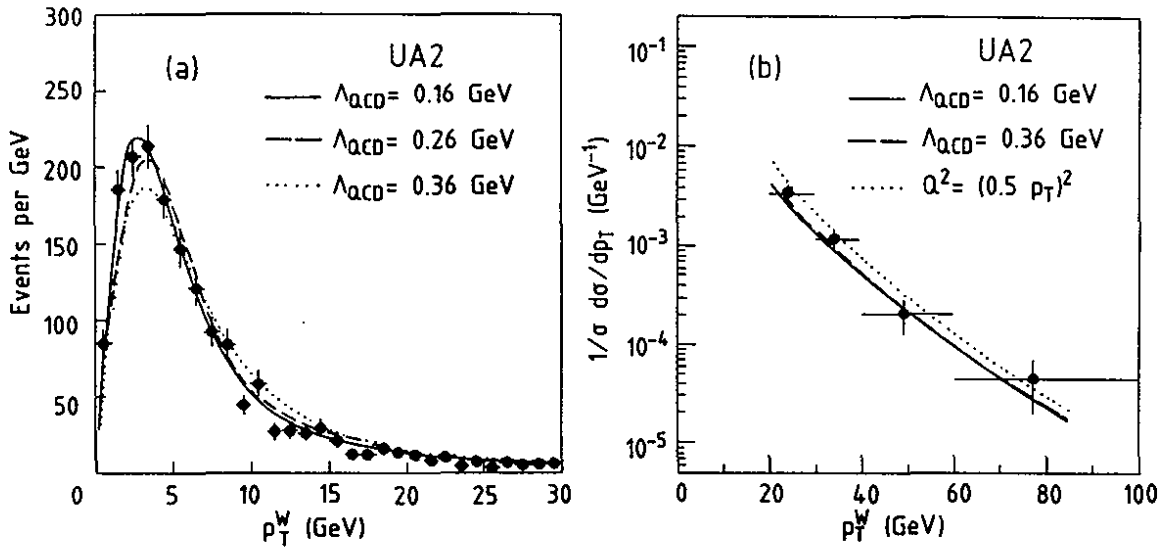

Figure 15

a) W transverse momentum distribution with p_T^W below 30 GeV/c from UA2

b) W transverse momentum distribution with p_T^W above 20 GeV/c from UA2

The transverse momentum distribution of the Z, $p_T^Z = p_T^{e^+e^-}$, is shown in Fig. 16. The measurement errors on p_T^Z are dominated by the energy resolution of the calorimeter, and are estimated to be about 2 GeV/c. The mean value for $p_T^Z < 30$ GeV/c amounts to $\langle p_T^Z \rangle = 7.0 \pm 0.4 \pm 0.1$ GeV/c, after correction for acceptance and resolution effects, where the first error is statistical and the second corresponds to the systematic uncertainties in the calorimeter resolution. Superimposed on the data shown in Fig. 16 are QCD predictions based on the same calculations as in the W case.

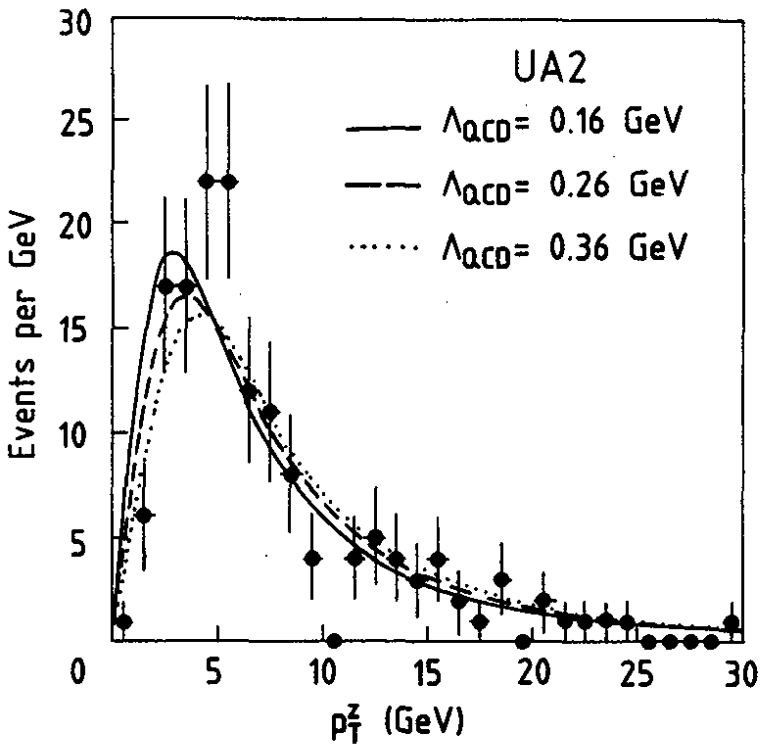

Figure 16
Z transverse momentum distribution, $p_T^{e^+e^-}$, from UA2

In CDF [47] the W and Z samples for the p_T^{IVB} measurements were selected with similar cuts to those used in the cross section ratio. For the W sample, an additional cut on the significance of the uncorrected missing transverse momentum, S_{E_T}, was applied to prevent a mismeasurement of $\not{p}_T$ by jet energy fluctuations in the event, and a cut on the uncorrected transverse mass of the electron-neutrino system was made. For the Z sample, the invariant mass of two electrons was restricted to the region $75 < m_{ee} < 105$ GeV/c^2 where the second electron was required to be in the central or plug region. Those selection cuts left 2685 W events and 220 Z events. The p_T distribution for the weak boson production is given in the form

$$\frac{1}{\sigma} \cdot \frac{1}{p_T} \cdot \frac{d\sigma}{dp_T} \quad . \tag{53}$$

In this form, some theoretical and experimental uncertainties from the weak couplings, parton distribution dependence and luminosity measurements tend to cancel. The p_T distributions from the data and a theoretical prediction are shown in Figs. 17a and 17b for the W and Z samples, respectively. The data points are corrected for acceptance and

efficiencies. The solid curves are a particular theoretical calculation which includes a part of the complete order α_s QCD calculation [33] using the MRSB parton distribution functions.

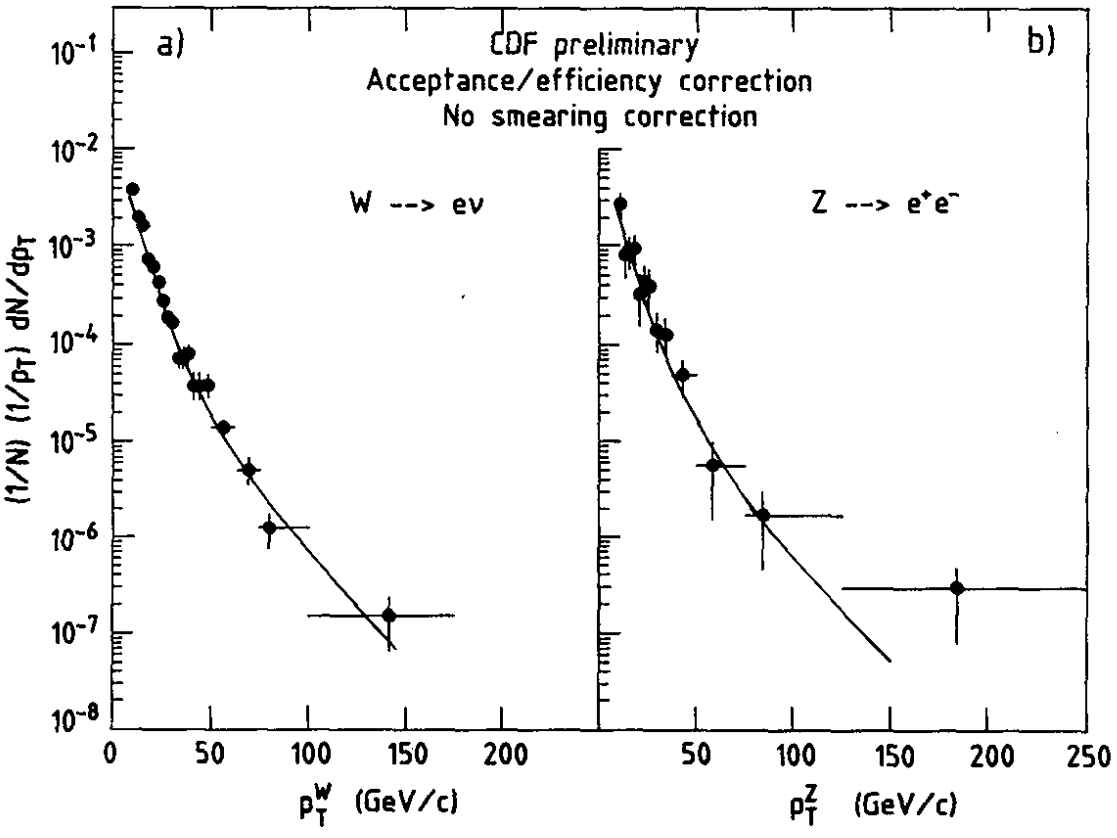

Figure 17
a) W transverse momentum distribution, p_T^W, from CDF
b) Z transverse momentum distribution, $p_T^{e^+e^-}$, from CDF

For the W sample, the background contamination is estimated to increase to ~ 20% in the region $p_T^W > 80$ GeV/c. The correction for the spectrum smeared by the calorimeter resolution is estimated to be roughly 15% for $p_T^W > 80$ GeV/c. In Figures 17a and 17b, such corrections are not yet applied. However, the agreement with the theoretical prediction is still reasonable even if corrections of such size are taken into account for the data points.

As a conclusion, we note that the p_T^{IVB} distributions of both experiments, UA2 and CDF, do not show any significant deviations from the theoretical predictions, once all uncertainties have been taken into account.

5.3 Inclusive W and Z angular distributions

The decay angular distributions of the intermediate vector bosons provide a test of the V - A structure of the electroweak theory. The couplings of the fermions to the Z boson are sensitive to the Weinberg angle. Therefore the $Z \rightarrow \ell^+\ell^-$ decay angular distribution can be used as an independent measurement of $\sin^2\theta_W$.

5.3.1 $W^{\pm}$ decays

For W's produced in valence quark - anti-quark annihilation processes, the decay leptons are expected to show a pronounced charge and angular asymmetry due to the pure V - A coupling of the charged currents. At low transverse momenta the W's are fully polarised along the beam direction. At CERN collider energies contributions from sea-sea quark annihilation can be neglected and the decay angular distribution in the centre-of-mass system of the W can be written in the simple form :

$$\frac{dN}{d(\cos\Theta^*)} = (1 + \cos\Theta^*)^2 \qquad (54)$$

where Θ^* is the angle between the electron and the proton direction (or positron and antiproton direction) in the W rest frame.

The mean value of the decay angular distribution times the W charge, Q_W, is directly correlated with the spin J of the W :

$$\langle Q_W \cdot \cos\Theta^* \rangle = \frac{\langle \lambda \rangle \langle \mu \rangle}{J(J+1)} \quad \text{for } J > 0 \qquad (55)$$

$$= 0 \quad \text{for } J = 0$$

where μ and λ are the global helicities of the production system ($u\bar{d}$ or $\bar{u}d$) and the decay system ($e\nu$), respectively. A value of 0.5 is expected for a W of spin 1 where initial and final fermion states are fully polarized ($\langle\lambda\rangle = \langle\mu\rangle = \pm Q_W$) and sea-sea contributions are ignored.

The W decay angular distribution as measured by UA1 [44] from the 1982 - 1985 data is shown in Fig. 18 for events with $p_T^W < 15$ GeV/c as a function of $Q_W \cdot \cos\Theta^*$. The distribution is corrected for background, acceptance and resolution effects and the bias introduced in choosing one of the two solutions for the longitudinal momentum of the neutrino, p_L^ν. The p_L^ν is necessary for defining the Lorentz transformation between the

laboratory and the W rest frame. There is agreement with the $(1 + \cos\Theta^*)^2$ behaviour expected for pure V - A coupling. The shaded band shows the small sea-sea contribution of 2 - 4% depending on the choice of the structure functions. An additional uncertainty in the value of $\langle Q_W \cdot \cos\Theta^* \rangle$ arises when the W's are produced with non-zero transverse momentum which distorts the W alignment with the beam axis.

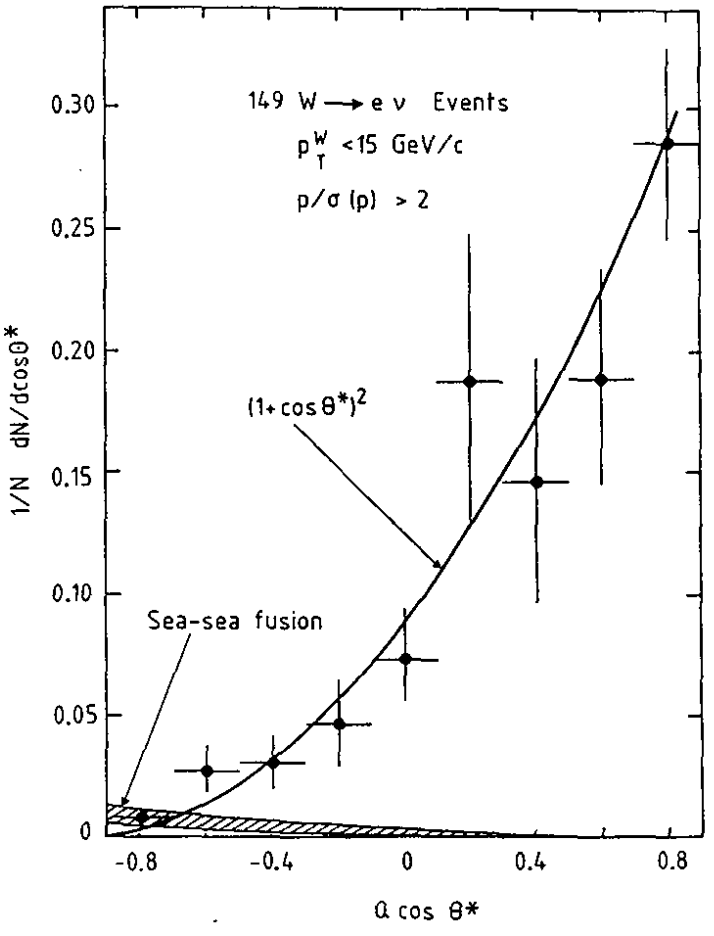

Figure 18
Decay angular distribution of $W \rightarrow e\nu$ from UA1

CDF has measured the forward-backward asymmetry, A_W^{FB}, for the W decaying in electrons and muons [55] which is defined as

$$A_W^{FB} = \frac{N_{\cos\theta^* > 0} - N_{\cos\theta^* < 0}}{N_{\cos\theta^* > 0} + N_{\cos\theta^* < 0}}, \qquad (56)$$

with θ^* being the decay angle of the electron in the centre-of-mass system of the W boson. The data sample has been restricted to a transverse mass of the lepton-neutrino system in excess of 50 GeV/c^2. The distributions of A_W^{FB} as a function of the pseudorapidity of the

leptons are shown in Figs 19a and 19b for the muon and electron decay, respectively. Also shown in that figure are QCD predictions from different sets of parton density functions. It can be seen from that figure that the forward-backward asymmetry might be a useful variable to distinguish between different sets of structure functions. The presently available statistics do not allow a detailed conclusion yet.

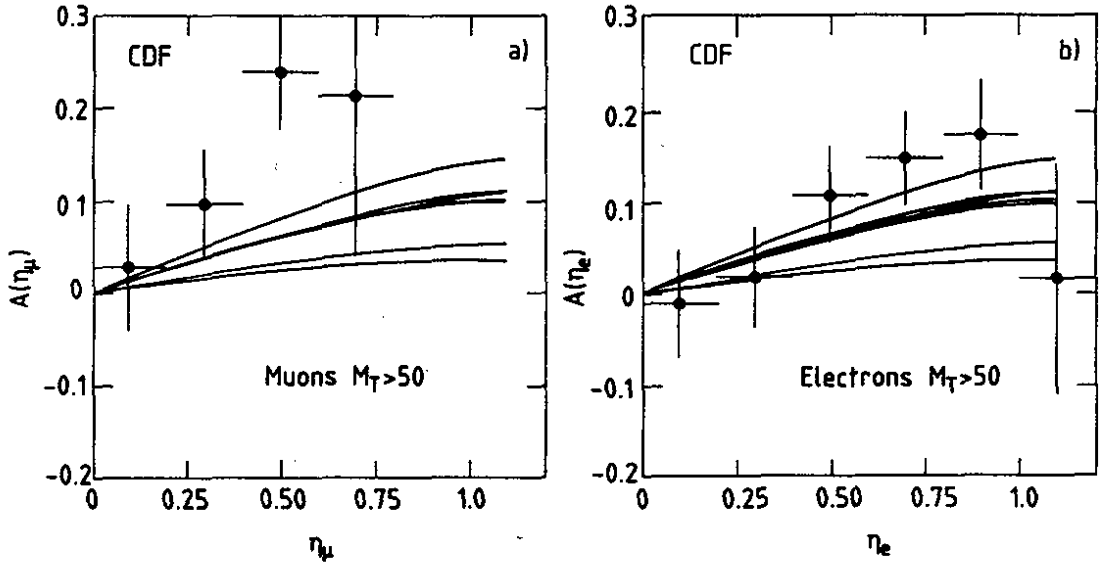

Figure 19
a) Forward-backward asymmetry of $W \rightarrow \mu\nu$ from CDF for muons
b) Forward-backward asymmetry of $W \rightarrow e\nu$ from CDF for electrons

5.3.2 Z^o decays

Because the Z coupling to charged leptons is almost purely axial vector coupling, the expected decay angular asymmetry is small. The angular distribution can be parametrized as

$$\frac{dN}{d\cos\theta^*} \sim (1 + 2 \cdot k \cdot \cos\theta^* + \cos^2\theta^*), \qquad (57)$$

where k depends on the vector and axial-vector parts of the couplings of the fermions to the Z, and is thus sensitive to $\sin^2\theta_W$.

CDF has measured the forward - backward asymmetry, A_Z^{FB}, from the Z sample [56], where A_Z^{FB} is defined in a similar way to the W case (see Eq. (56)). The angular

distribution for $Z \rightarrow e^+e^-$ as measured by CDF is shown in Fig. 20.

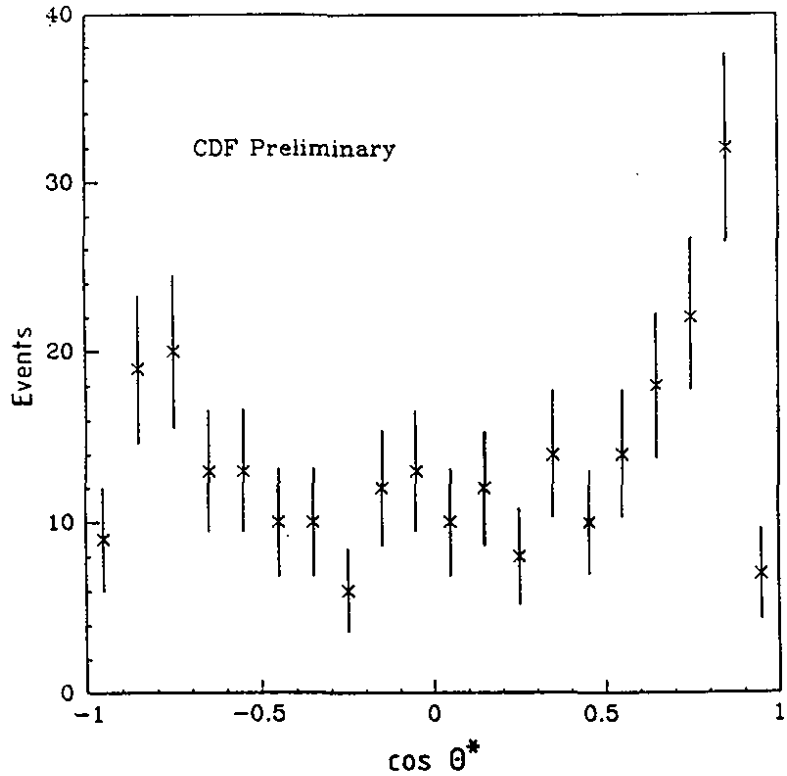

Figure 20
Decay angular distribution of $Z \rightarrow e^+e^-$ from CDF

From a log likelihood fit after corrections for background subtraction, QCD corrections to the p_T^Z spectrum and QED corrections the following preliminary result on A_Z^{FB} has been obtained

$$A_Z^{FB} = 0.058 \pm 0.059 \pm 0.006, \tag{58}$$

with the first error being the statistical and the second error the systematic uncertainty. This measurement provides an independent evaluation of $\sin^2\theta_W$ which is measured to be

$$\sin^2\theta_W = 0.229 \pm 0.016 \pm 0.002. \tag{59}$$

The systematic uncertainty results from uncertainties in background subtraction, the fitting procedure, efficiencies of the electron trigger, track reconstruction and electron selection, structure function and QED corrections.

5.4 Hadronic decay modes

In the SM of electroweak interactions, the Intermediate Vector Bosons, W and Z, are expected to decay mainly into quark-antiquark pairs with well defined branching fractions. Excluding decays with a top-quark in the final state, which is assumed to be too heavy to contribute, the SM predictions are:

$$\frac{\Gamma(W \to q\bar{q})}{\Gamma(W \to e\nu)} \approx 6, \text{ and} \qquad (60)$$

$$\frac{\Gamma(Z \to q\bar{q})}{\Gamma(Z \to e^+e^-)} \approx 20.$$

The observation of such decays is an important check of the predictions of the SM. In addition it provides also a first test case of the ability of future collider experiments to reconstruct the invariant mass of multi-jet systems as a way to discover possible new heavy particles.

The experimental difficulties in detecting this signature at hadron colliders arise from the presence of a copious background of two-jet events produced by strong interactions (QCD) between the colliding partons. The expected decay rates are large compared to the leptonic ones, but a signal of only a few percent is expected over an enormous QCD background with very similar final states, therefore excluding an analysis on an event-by-event basis. Instead the peak structure from hadronic W and Z decays has to be observed as a departure from the two-jet mass spectrum from QCD processes. Therefore, a good two-jet mass resolution and a large integrated luminosity are required in searching for IVB $\to$ jet + jet events. The UA2 experiment has reported the result of such a search from the 1985 data sample [57], showing a signal of about three standard deviations significance. From the 1988 - 1989 running period a data sample which is 6 times larger corresponding to 4.7 pb^{-1} has been used, and a new analysis has been performed [58]. The cuts used to extract a signal are as follows :

a) a vertex constraint of $|z| < 20$ cm using the TOF counters has been applied,
b) the two jets are well contained in the CC calorimeter region, $|\eta| < 0.7$,
c) a veto on additional jet activity of $E_T^{jet} < 20$ GeV,
d) a veto on $Z \to e^+e^-$ using the EM energy fraction, f_{EM}^1, $f_{EM}^2 = \frac{E_{EM}}{E_{TOT}} < 80\%$ and
e) a veto on jets not fully contained in the calorimeters, because of late showering, of f_{EM}^1, $f_{EM}^2 > 20\%$ have been applied.

With these cuts, the new data show a clear evidence for an excess of two-jet events in the mass region where the hadronic decays of the IVBs are expected to appear, as shown in Fig. 21.

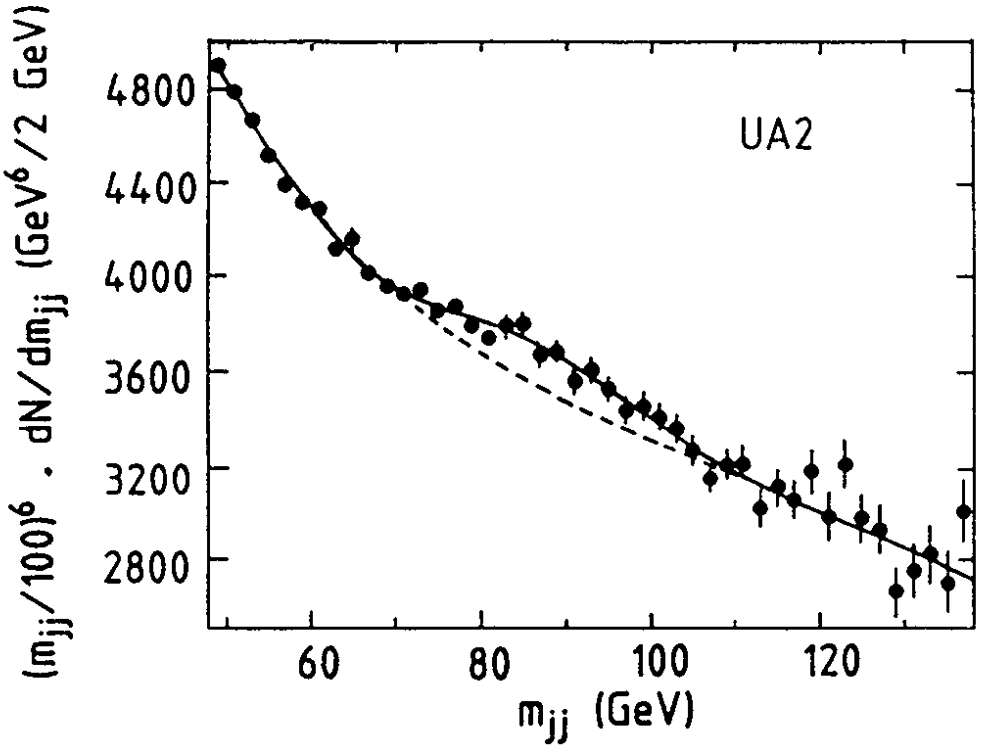

Figure 21
Two-jet mass spectrum from UA2. Vertical scale weighted by $(m/100)^6$

Various attempts have been made, using smooth functions, such as for example $m^{-\alpha} \cdot e^{-\beta m} \cdot e^{-\gamma m^2}$, to parametrize the two-jet mass distribution. These have failed, and the discrepancy turned out to occur mainly within a mass window of ~ 30 GeV/c^2 around 85 GeV/c^2. Contributions from the W and Z bosons with the following parameters for the line shape have therefore been introduced :

i. a fixed value for the mass ratio, $m_Z/m_W = 1.13$,
ii. a fixed value for the ratio of the partial widths, $\Gamma(Z \rightarrow q\bar{q})/\Gamma(W \rightarrow q\bar{q}) = 0.397$ assuming five flavours,
iii. a double gaussian peak according to the measured resolution.

Together with a free normalisation the result shown in Fig. 21 has been obtained, where the vertical scale has been multiplied by a factor $(m/100)^6$ to improve visibility. The dashed line represents the contribution of the two-jet background alone in the region around 85 GeV/c^2.

Due to QCD-electroweak interference effects in the quark scattering process, the signal in the two-jet mass distribution is not simply an incoherent superposition of W and Z resonances on the rapidly falling QCD continuum. A calculation of the interference term and of its manifestation in the experimentally observed two-jet mass distribution has been carried out in Ref. [59]. This interference term increases the signal by 11 ± 21% and shifts its apparent mass by +1.8 ± 1.3 GeV/c^2. Given the large uncertainties we conclude that the current measurement is not sensitive to such details of the line shape. The two-jet mass peak shown in Fig. 21 contains 5618 ± 1334 events in the mass range of $70 < m_{jj} < 100$ GeV/c^2 compared to an expectation of 4718 ± 167 events from W and Z decays including the interference effects mentioned above. The expectations have been calculated by normalizing to the measured leptonic cross section from UA2 (see Section 5.1). The mass resolution obtained is $\Delta m/m = (9.9 \pm 2.5)\%$. The W and Z signals cannot be separated. The significance of the signal is a four standard deviation effect. The fitted mass is $m_W = 79.9 \pm 1.1$ GeV/c^2, which is consistent with SM expectations. The background subtracted distribution as a function of the two-jet invariant mass is shown in Fig. 22 for the data (black points), the excess of events over the fitted QCD background together with the overall W, Z fit (solid line) and the contributions from W and Z separately (dashed lines). The maximum value obtained for the signal/background ratio is 5%.

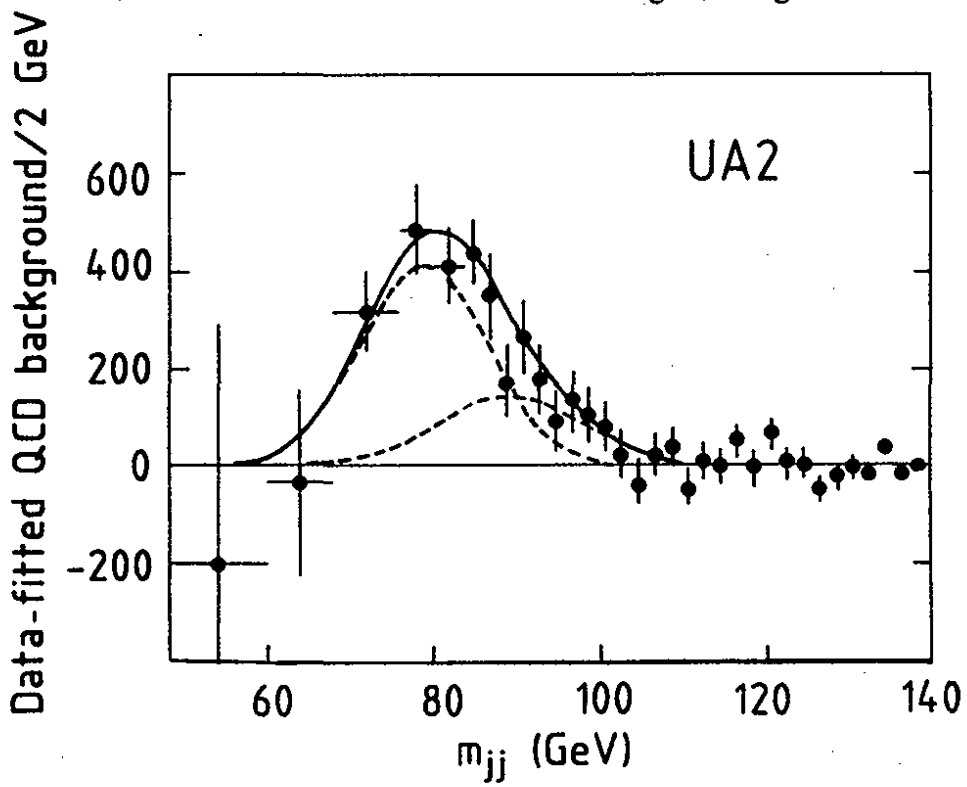

Figure 22

Background subtracted two-jet mass spectrum from UA2

Because of triggering problems, of threshold settings and of resolution effects on the jet determination, none of the other $\bar{p}p$ collider experiments are expected to obtain results on this subject.

5.5 Measurement of the W and Z masses

A precise measurement of the W and Z masses, fixes the theory of electroweak interactions and allows to test for deviations from the MSM and to study the effects of higher order radiative corrections. These masses are the two parameters of the SM which can be directly measured by the CERN and TEV-I collider experiments. Although the most precise values for the Z mass are now obtained from the SLC and LEP experiments [42] - an accuracy of better than 30 MeV/c^2 has been achieved -, hadron colliders still provide the only measurement of the W mass. At the CERN collider the uncertainties in the mass measurements are dominated by the energy scale error, whereas for CDF the statistical error and the uncertainty of the E/p calibration dominate (see section 3.3).

For the Z boson, the mass can be determined in a straightforward way from the invariant mass spectrum of the lepton pairs in the e^+e^- and $\mu^+\mu^-$ final states. Monte Carlo methods (maximum likelihood techniques) are used to extract m_Z taking into account the experimental mass resolution due to detector effects and the relativistic Breit-Wigner shape of the Z peak, its finite width and the asymmetric production due to the structure functions.

To determine the Z boson mass, UA2 uses two independent data samples. The first sample contains only events where both electrons are contained in the fiducial region of the central calorimeter, well away from cell edges and cracks. This sample contains 54 well measured $Z \rightarrow e^+e^-$ decays in the mass range of $70 < m_{ee} < 120$ GeV/c^2 satisfying the cuts described above. A second independent sample has been used where only one of the two electrons is contained in the fiducial region of the central calorimeter. The other electron should be either in the endcap region or in edges or cracks of the central calorimeter. To transport the mass scale of the well measured sample to the second sample, the total momentum constraint from electrons and hadrons has been used ($\vec{p}_T^{\,e} + \Sigma \vec{p}_T^{\,hadrons} = 0$) to determine the energy of the electron not contained in the fiducial region. The second sample has of course a worse mass resolution and a larger systematic uncertainty due to the worse energy resolution of the hadron energy scale, but this independent event sample which contains 94 events in the mass range of $70 < m_{ee} < 120$ GeV/c^2, reduces the statistical error affecting the measurement of m_Z.

In CDF, 123 $Z^0 \rightarrow \mu^+\mu^-$ in the mass range $75 < m_{\mu\mu} < 105$ GeV/c^2 were obtained using the tracking requirement. For the electron sample the radiative decays affect the measured mass appreciably more strongly than for the muon mode. Consequently, the best measurement of the Z^0 mass is obtained using calorimeter information. 65 $Z^0 \rightarrow e^+e^-$ are fitted in the mass range of $80 < m_{ee} < 100$ GeV/c^2.

The data samples together with the result of the fits to a Breit-Wigner distribution convoluted with the detector resolution are shown in Fig. 23a and 23b for the two UA2 data samples. In Fig. 24a and 24b the same result is shown for CDF using the central tracking chamber for the $Z \rightarrow \mu\mu$ and $Z \rightarrow ee$ data samples respectively, while in Fig. 24c the result in shown for the $Z \rightarrow ee$ data using the calorimeters.

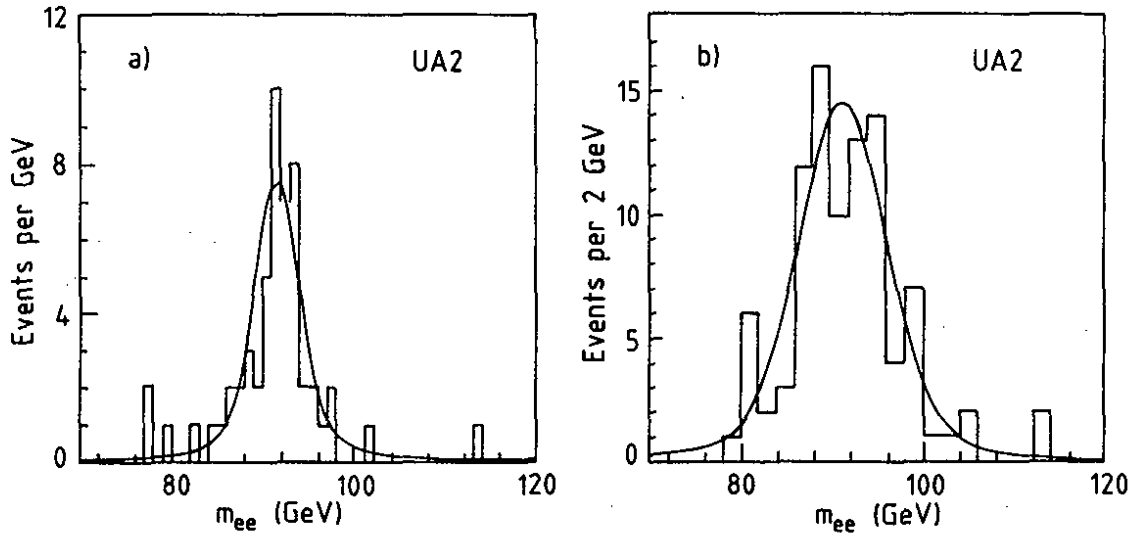

Figure 23
a) Invariant mass distribution, m_{ee}, from UA2
b) Invariant mass distribution, m_{ee}, from UA2 using the p_T constraint

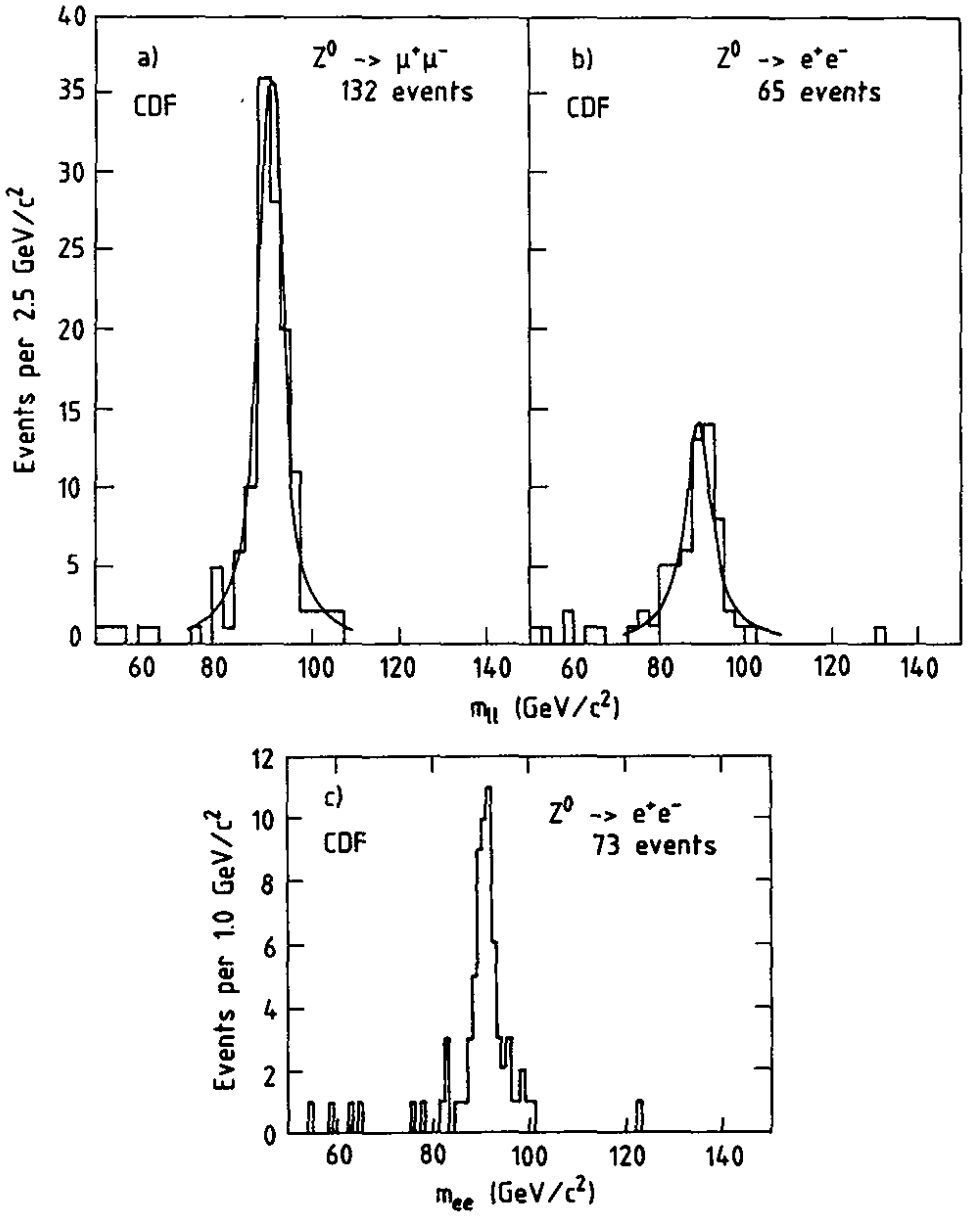

Figure 24

a) Invariant mass distribution, $m_{\mu\mu}$, from CDF

b) Invariant mass distribution, m_{ee}, from CDF using the central tracking chamber

c) Invariant mass distribution, m_{ee}, from CDF using the calorimeters

The final results of the fits from the UA1 [44] (only 1982-1985 data), UA2 [60] and CDF [61] experiments on the Z mass are summarized in Table 7. There is good agreement between experiments and also with the LEP Z mass measurement.

Table 7 : Z mass measurements

Reaction	UA1*)	UA2	CDF
$Z \to e^+e^-$	$93.1 \pm 1.0 \pm 3.1$	$91.49 \pm 0.35 \pm 0.12$(syst.) ± 0.91(scale)	$91.37 \pm 0.34 \pm 0.04$ ± 0.22(scale)
$Z \to \mu^+\mu^-$	$94.1\ ^{+8.4}_{-6.6} \pm 2.8$	-	$90.71 \pm 0.40 \pm 0.04$ ± 0.09(scale)
Z combined	-	-	91.09 ± 0.26(stat+syst) ± 0.22(scale)

*) Values from 1985

all masses are given in GeV/c^2

At hadron colliders the W mass cannot be determined directly from the $W \to \ell\nu$ decays, since the longitudinal momentum of the neutrino cannot be measured, because undetected particles which carry a substantial momentum fraction escape along the beam pipe. Only the transverse components of the neutrino momentum are measured. Therefore the W mass has to be determined by fits to transverse variables, p_T^ℓ, p_T^ν and $m_T^{\ell\nu}$, where p_T^ℓ is the electron, the muon or the tau-jet transverse momentum, p_T^ν the neutrino transverse momentum and $m_T^{\ell\nu}$ the transverse mass of the lepton-neutrino pair. There is only a weak contraint with the W mass value to the decay leptons in the forward region. For this reason the experiments have limited their W sample to leptons in the central region (UA2: electrons in $|\eta| < 0.9$; CDF: electrons and muons in $|\eta| < 1.1$). To minimize the systematic uncertainties from the shape of the p_T^W distribution events with $p_T^W > 20$ GeV/c have also been excluded by UA2. For the same reason and with even more stringent cuts, CDF excludes all events which have a reconstructed jet exceeding 7 GeV/c of transverse

momentum from the analysis. The requirement to reject events with high p_T jets attemps to minimize the uncertainty to the measurement of $\vec{p}_T^{\nu} = - \vec{p}_T^{\ell} - \Sigma\vec{p}_T^{hadrons}$. Events in which one or both leptons hit close to a cell boundary have also been removed to ensure the high quality of the energy reconstruction. Kinematical cuts have been applied to reduce the background to a negligible level. The mass of the W was estimated with a maximum likelihood fit to all three transverse variables. The systematic error on the result receives contributions from structure function uncertainties, the shape of the p_T^W distribution, resolution effects from the p_T of the recoiling hadrons and the scale uncertainty for the missing transverse energy measurement. All these uncertainties contribute in different ways to the three variables to fit the W mass, p_T^{ℓ}, p_T^{ν} and $m_T^{\ell\nu}$.

In UA2, the selection criteria described above, resulted in a W sample of 1203 events in the kinematical region of $40 < m_T^{e\nu} < 120$ GeV/c^2. This sample is dominated by $W \rightarrow e\nu$ decays, with a contribution of 3.8% from the process $W \rightarrow \tau\nu$ followed by the decay $\tau \rightarrow e\nu\bar{\nu}$ which is taken into account in the fit.

In CDF, the final W samples contain 1130 electron and 592 muon candidates. Note that the event samples used by the UA2 and CDF experiments are of comparable size. CDF uses an even slightly smaller event sample in the electron channel than UA2. Apart from the differences in accumulated luminosities by a factor of two this reduction is mainly due to the strong selection criteria necessary to suppress the background to a neglibible level and to the restriction to central electrons. The fit to the transverse mass of the lepton-neutrino system was performed in the mass range of $65 < m_T^{\ell\nu} < 94$ GeV/c^2, while the fit to the lepton or the neutrino spectrum was limited to the region $32 < p_T^{\ell}, p_T^{\nu} < 48$ GeV/c.

Results from the transverse mass fit are shown in Fig. 25a for UA2 to the electron and in Figs. 25b and 25c for CDF to the electron and the muon channel. The result of the fits to the lepton spectrum and the neutrino spectrum are shown in Figs. 26a and 26b for UA2, and in Figs. 26c to 26f for CDF. A summary of all values obtained in the different W decay channels from the UA2 and CDF experiment is given in Table 8. In all cases a one-parameter-fit has been performed where the W mass is the only free parameter (keeping the W width fixed at the SM expectation of 2.1 GeV/c^2 ignoring any contribution from the top-quark). A two-parameter-fit where the W mass and its width are left as a free parameter has also been made yielding a slightly higher W masses. The three fit results agree very well with each other, demonstrating the high qualitity of the measurement, and indicating that the systematic uncertainties are well under control.

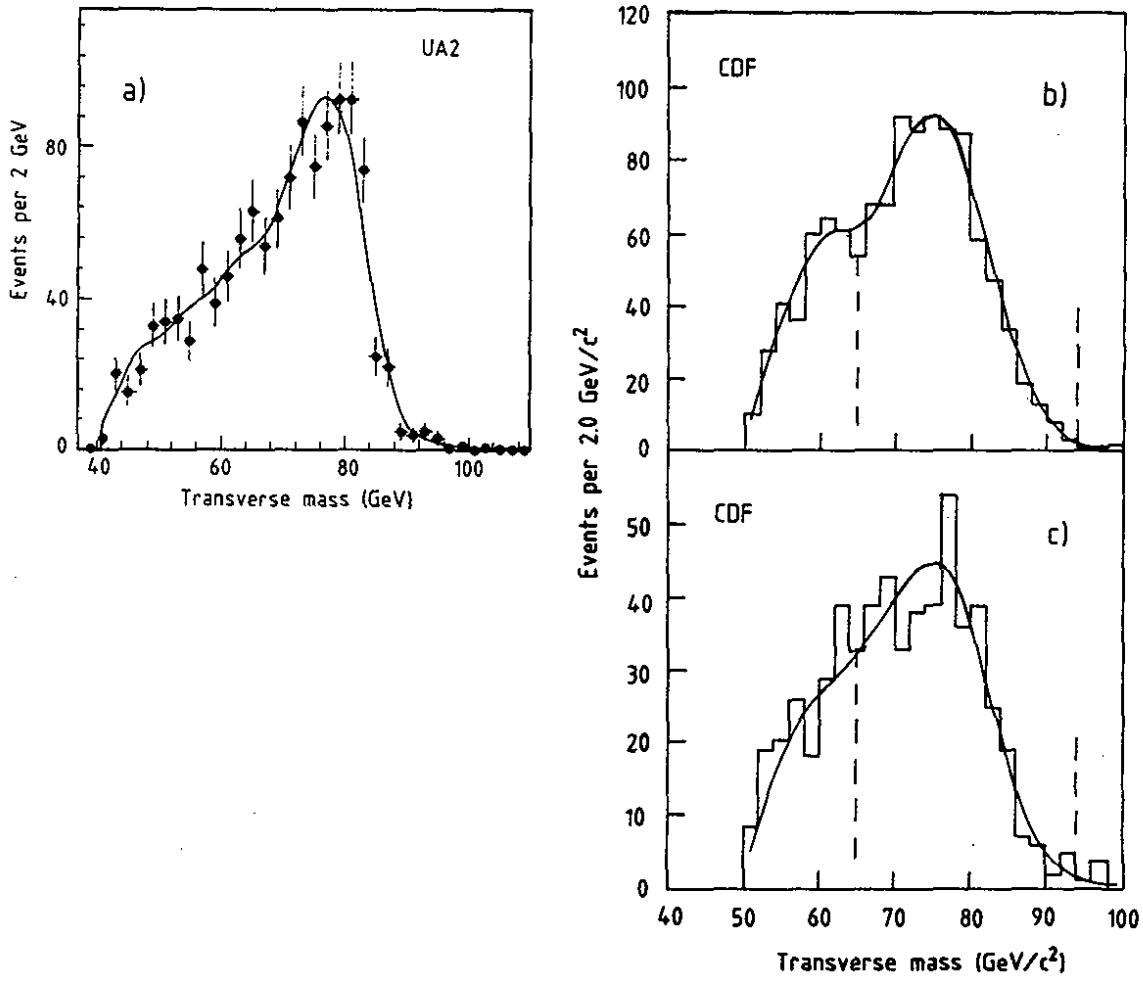

Figure 25

a) Transverse mass distribution, $m_T^{e\nu}$, from UA2

b) Transverse mass distribution, $m_T^{\mu\nu}$, from CDF

c) Transverse mass distribution, $m_T^{e\nu}$, from CDF

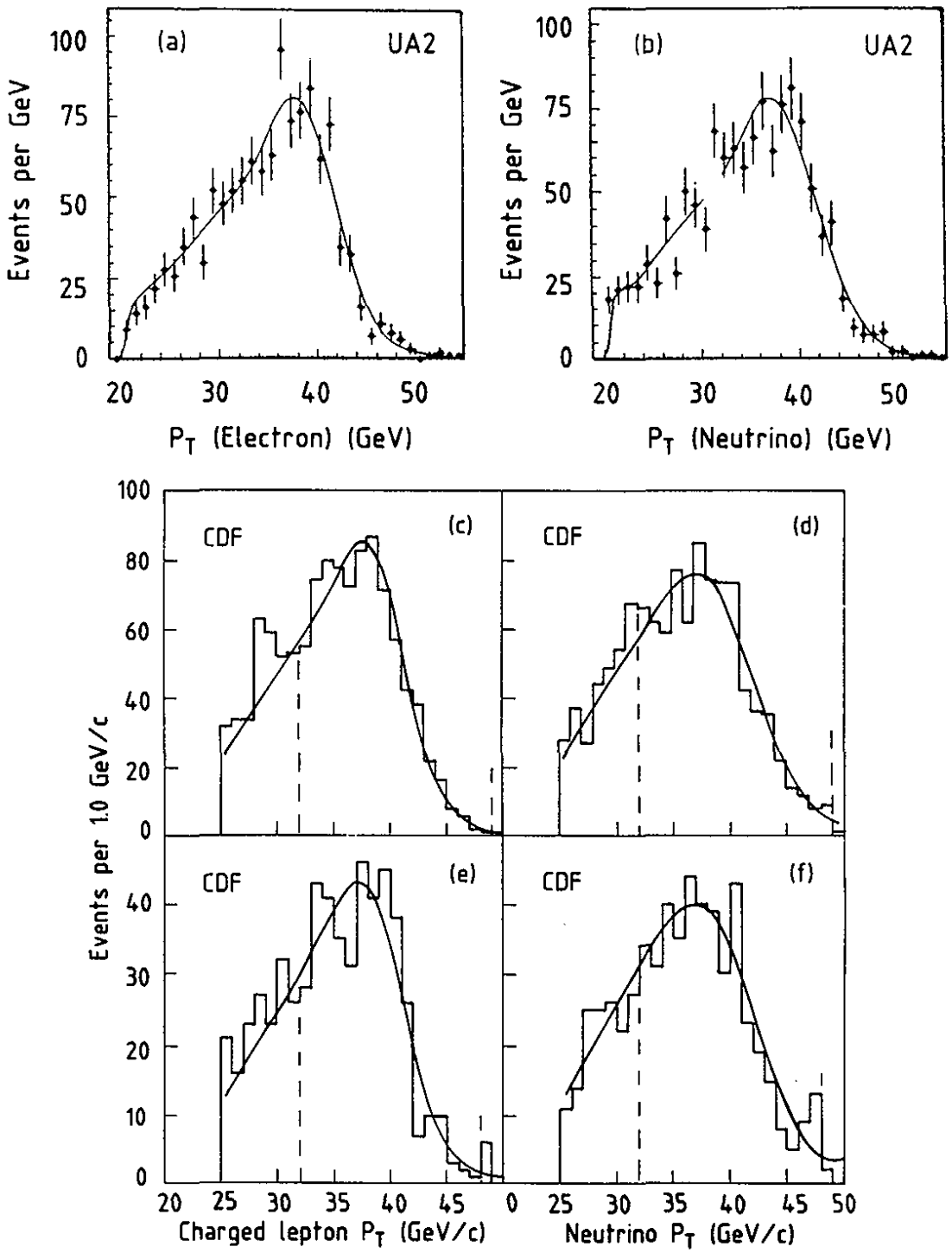

Figure 26

a) Electron transverse momentum distribution, p_T^e, from UA2

b) Neutrino transverse momentum distribution, p_T^ν, from UA2

c) Electron transverse momentum distribution, p_T^e, from CDF

d) Neutrino transverse momentum distribution, p_T^ν, from CDF for electrons

e) Muon transverse momentum distribution, p_T^μ, from CDF

f) Neutrino transverse momentum distribution, p_T^ν, from CDF for muons

Table 8 : W mass measurements

sample	UA1*)	UA2	CDF
Transverse mass			
(electron)	82.7±1.0±2.7	80.79±0.31±0.21 ±0.81(scale)	79.91±0.35±0.24 ±0.19(scale)
(muon)			79.90±0.53±0.32 ±0.08(scale)
p_T-lepton			
(electron)	$81.8\ ^{+6.0}_{-5.3} \pm 2.6$	80.85±0.38±0.30 ±0.81(scale)	80.06±0.40±0.43 ±0.19(scale)
(muon)			79.44±0.56±0.31 ±0.08(scale)
p_T-neutrino			
(electron)	89.0±3.0±6.0	80.48±0.41±0.47 ±0.81(scale)	80.20±0.52±0.55 ±0.19(scale)
(muon)			79.89±0.78±0.48 ±0.08(scale)
W combined from $m_T^{\ell\nu}$	-	-	79.91±0.39(stat+syst+scale)

*) Values from 1985

all masses are given GeV/c^2

All experiments have taken the results from the fit to the transverse mass of the lepton-neutrino pair which gave the smallest uncertainty on the W mass. These values as taken from Refs. of UA2 [60] and CDF [62] are summarized in Table 9 together with a detailed list of the different sources of systematic uncertainties. The first error shown represents the statistical and the second error the systematic uncertainty, which does not include the energy scale uncertainty. This uncertainty is given separately and indicated as such. Due to the low statistics of the old 1982-1985 data UA1 could not make such detailed studies of the different sources of uncertainties, therefore these cannot be given. As can be seen from Table 9 the largest uncertainty on the W mass measurement arises from the insufficient knowledge of the p_T^W measurement and of the detector response to the recoiling hadrons.

Table 9 : Uncertainties on the W mass measurements

	UA2	CDF	
Reaction	$W \to e\nu$ (calorimetry)	$W \to \mu\nu$ (tracking)	$W \to e\nu$ (calorimetry)
W mass	80.79±0.31±0.21 ±0.81(scale)	79.9±0.53±0.32 ±0.08(scale)	79.91±0.35±0.24 ±0.19(scale)
Statistics	**±0.31**	**±0.53**	**±0.35**
Tracking chamber	-	±0.08	±0.08
Calorimetry	±0.81	-	±0.175
Energy scale	**±0.81**	**±0.08**	**±0.19**
Proton structure functions	±0.10	±0.06	±0.06
p_T^W resolution	±0.12	±0.15	±0.145
Parallel balance	±0.09	±0.24	±0.17
Background	negligible	±0.11	±0.05
Fitting procedure	±0.10	±0.05	±0.05
Underlying event	±0.03	±0.03	±0.03
Radiative decays	+0.04±0.04	+0.13±0.01	+0.07±0.01
Systematics	**+0.04±0.21**	**+0.13±0.32**	**+0.07±0.24**

All masses and uncertainties are given in GeV/c^2

The two recent measurements of the W and Z masses from the UA2 and CDF experiment can be combined to derive a value for the ratio, m_W/m_Z. One expects an almost perfect cancellation of the energy scale contribution to the error on the ratio. Deviations from this expectation can arise if the calorimeter response to electrons is not perfectly linear. The mass ratio measured by UA2 and CDF is given in Table 10 where the first error shown is statistical and the second the systematic uncertainty. For completeness we add the old UA1 measurement from the 1982-1985 data as well.

Table 10 : Ratio of the W mass over the Z mass, m_W/m_Z

Reaction	**UA1*)**	**UA2**	**CDF+)**
e-channel	0.8883±0.0144±0.0167	0.8831±0.0048±0.0026	0.8786±0.0040±0.0019

*) Values from 1985
+) Electron and muon channels combined

The weighted average of the values quoted in Table 10 is

$$\frac{m_W}{m_Z} = 0.8806 \pm 0.0034, \qquad (61)$$

where the statistical and systematic uncertainty have been added in quadrature.

The mass ratios can be combined with the most recent results from SLC and LEP [42] on the Z mass to give rescaled measurements of the W mass. In this case, the energy scale uncertainty nearly disappears at the price of an increased statistical error due to the poor Z statistics which has to be taken into account when normalizing to the LEP Z mass value. We have used this procedure of rescaling for the old UA1 and the UA2 data. Because of the small scale error of the CDF Z mass measurement, a rescaling to the LEP Z value is not needed, since it would only increase the quoted error due to the poor Z statistics. For this reason the CDF measurement is not rescaled. The final value for the W mass is given in Table 11 as measured by the $\bar{p}p$ collider experiment with the statistical and the systematic error added in quadrature. There is very good agreement between the three experiments and also with the SM predictions (see Eq. (17)).

Table 11 : Final W mass

Reaction	UA1*,++)	UA2++)	CDF+)
e-channel	80.98±1.90	80.52±0.49	79.91±0.39

*) Values from 1985
+) Electron and muon channels combined ++) rescaled with LEP Z mass

all masses are given in GeV/c^2

The three measurements of the W mass can be statistically combined. The result is

$$m_W = 80.14 \pm 0.31 \text{ GeV}/c^2 \qquad (62)$$

which is the best direct measurement of m_W from the available $\bar{p}p$ data. The error shown reflects the statistical and systematic errors added in quadrature. This result is visualized in Fig. 27. Also shown on the figure are theoretical predictions for m_W assuming different values for the mass of the top-quark. The solid lines are theoretical predictions for $m_{Higgs} = 100$ GeV/c^2, the dotted and dashed lines are the predictions for $m_{top} = 80$ GeV/c^2 and $m_{Higgs} = 44$ and 1000 GeV/c^2, respectively. One can conclude from that figure that a heavy top-quark is preferred by the data.

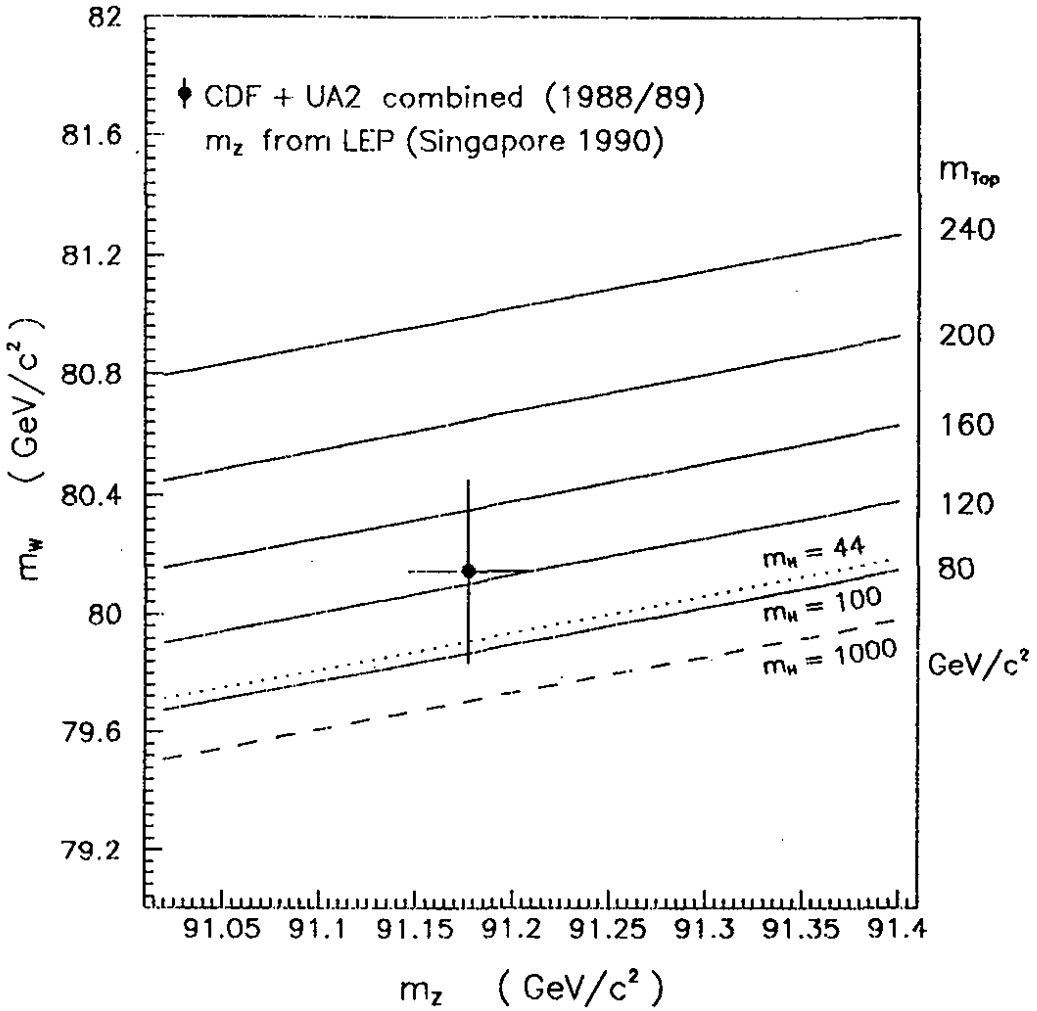

Figure 27
m_W as a function of m_Z

Another way of displaying the same result is shown in Fig. 28, where m_W is directly plotted as a function of m_{top}. The dashed and dotted lines have the same meaning than in Fig. 27. Using the $\bar{p}p$ collider data alone, we can place a lower limit on the top-quark mass from the m_W measurement of

$$m_{top} > 56 \text{ GeV/c}^2 \qquad (63)$$

at the 90% confidence level with $m_{Higgs} > 44$ GeV/c^2 and an upper limit of

$$m_{top} < 219 \text{ GeV/c}^2, \qquad (63')$$

at the 95% confidence level with $m_{Higgs} < 1000$ GeV/c^2. These limits change by + 7 GeV/c^2 (see Eqs. (68) and (68')), if $\sin^2\theta_W$ derived from the weighted average of the mass ratio is used instead. This difference is explained by the fact that in the first case the LEP m_Z mass is used, whereas in the second case m_Z is taken as measured by each of the

$\bar{p}p$ collider experiments. Note that the choice of the upper limit on the Higgs mass is totally arbitrary, therefore these limits should not be over-emphasised.

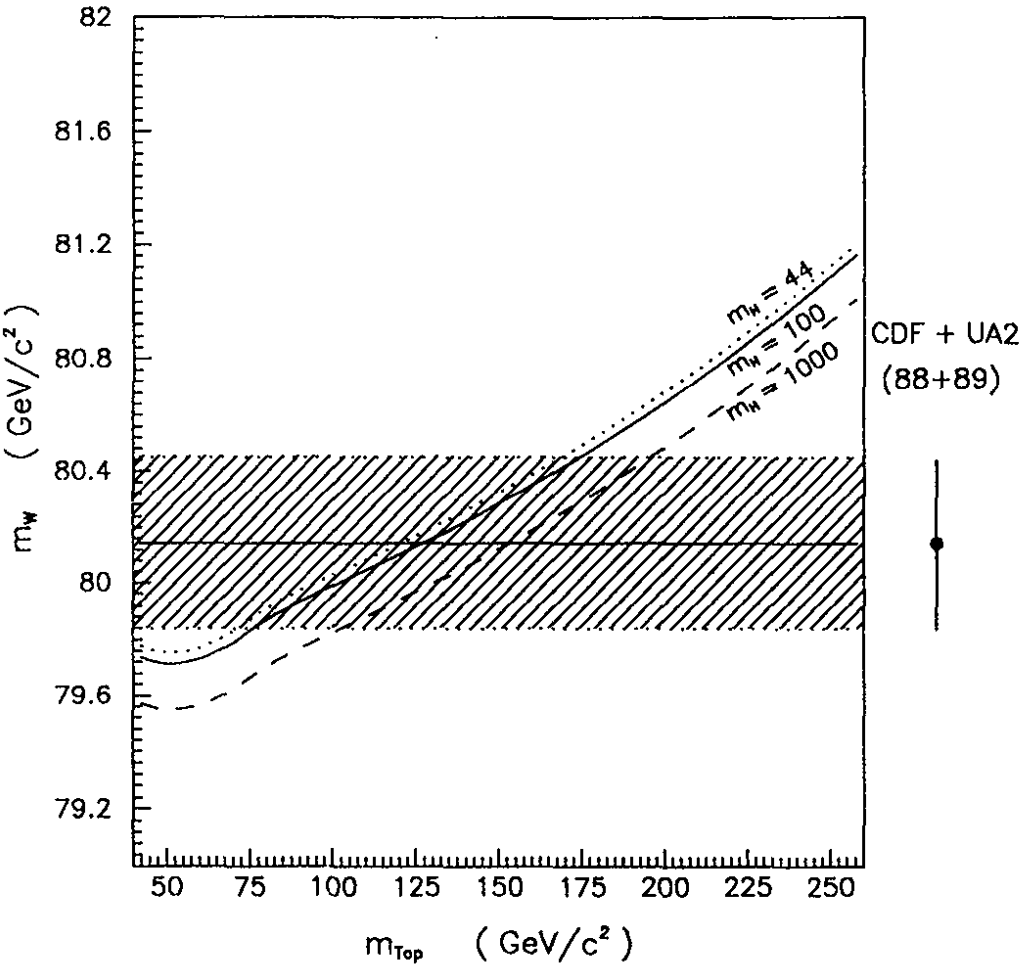

Figure 28
m_W as a function of m_{top}

6. STANDARD MODEL PARAMETERS

To make precision tests of the SM, it is important to measure the fundamental parameters of the theory in many different processes and to ensure that all results are in agreement. The deep-inelastic neutrino-scattering experiments allowed predictions of the W and Z masses through the measurement of the SM parameters. The subsequently measured $\bar{p}p$ and e^+e^- collider values have been in remarkable agreement with these parameters. In return, the measurements of m_W and m_Z allow to check the predictions of the Standard Model, once properly renormalized and radiatively corrected quantities are used.

The Standard Model can be tested by extracting i) $\sin^2\theta_W$, ii) ρ, iii) Δr from the measured values of m_W and m_Z as follows :

i. a) Equation (12) provides a direct measurement of $\sin^2\theta_W$ independent of other experiments and of theoretical uncertainties. In this case, the statistical error is dominated by the poor Z statistics at $\bar{p}p$ colliders and the systematic error is mostly related to uncertainties of the m_W fit, while the mass scale uncertainty cancels out in the ratio m_W/m_Z.

b) A more precise value of the weak mixing angle can be extracted by a simultaneous fit of the measured m_W and m_Z to the theoretical equations (13) and (13') using the precise knowledge of A (see Eq. 14') and a value for the radiative corrections of $\Delta r = 0.0574 \pm 0.0013$ (see Ref. [30]) which assumes $m_{top} = m_{Higgs} = 100$ GeV/c^2. In this case, the systematic error is dominated by the error on the energy scale and the measurement relies on the theoretical assumptions used to calculate Δr.

The UA1, UA2 and CDF measurements of $\sin^2\theta_W$ are given in Table 12 for both methods. All the measurements are in good agreement.

Table 12 : Experimental measurement of the Weinberg angle $\sin^2\theta_W$

Reaction	**UA1*)**	**UA2**	**CDF+)**
a) From $\sin^2\theta_W \equiv 1 - m_W^2/m_Z^2$			
e-channel	0.211±0.025	0.2202±0.0084±0.0045	0.2305±0.0071±0.0030
b) From $\sin^2\theta_W = f(m_W,\alpha,G_F,\Delta r)$ with $m_{top} = m_{Higgs} = 100$ GeV/c^2			
e-Channel	0.219±0.005±0.014	0.2279±0.0017±0.0039	0.2310±0.0014±0.0016
μ-channel	0.223±0.033±0.014		

*) Values from 1985
+) Electron and muon channels combined

The best measurement of $\sin^2\theta_W$ from the $\bar{p}p$ collider experiments can be obtained from the weighted average of the two recent measurements of the mass ratio m_W/m_Z using Eq. (12). The result is

$$\sin^2\theta_W = 0.2265 \pm 0.0062. \qquad (64)$$

The functional dependence of $\sin^2\theta_W$ on the value of m_{top} as given by the SM is shown in Fig. 29 together with the combined experimental measurement from the $\bar{p}p$ colliders (see Eq. (64)). From this figure we can also get a lower limit of m_{top} which is

$$m_{top} > 63 \text{ GeV}/c^2 \qquad (65)$$

at the 90% confidence level with $m_{Higgs} > 44$ GeV/c^2 and an upper limit of

$$m_{top} < 226 \text{ GeV}/c^2, \qquad (65')$$

at the 95% confidence level with $m_{Higgs} < 1000$ GeV/c^2.

The measurement of $\sin^2\theta_W$ from the $\bar{p}p$ collider experiments is in good agreement with the world average [31] derived from neutral-current experiments

$$\sin^2\theta_W = 0.2309 \pm 0.0057,$$

and also with a recent measurement from the LEP experiments [42] where $\sin^2\bar{\theta}_W$ is derived from the measurement of the leptonic width of the Z boson,

$$\sin^2\bar{\theta}_W = 0.2302 \pm 0.0025. \qquad (66)$$

The error given in all three measurements is the combined statistical and systematic uncertainty. Note that the definition of $\sin^2\theta_W$ from the LEP experiments (see below) is not the same as the one used by the $\bar{p}p$ collider and the νN scattering experiments (see Eq. (12)) and therefore the errors on the measurements should not be directly compared, but the measured values should agree if the MSM is valid.

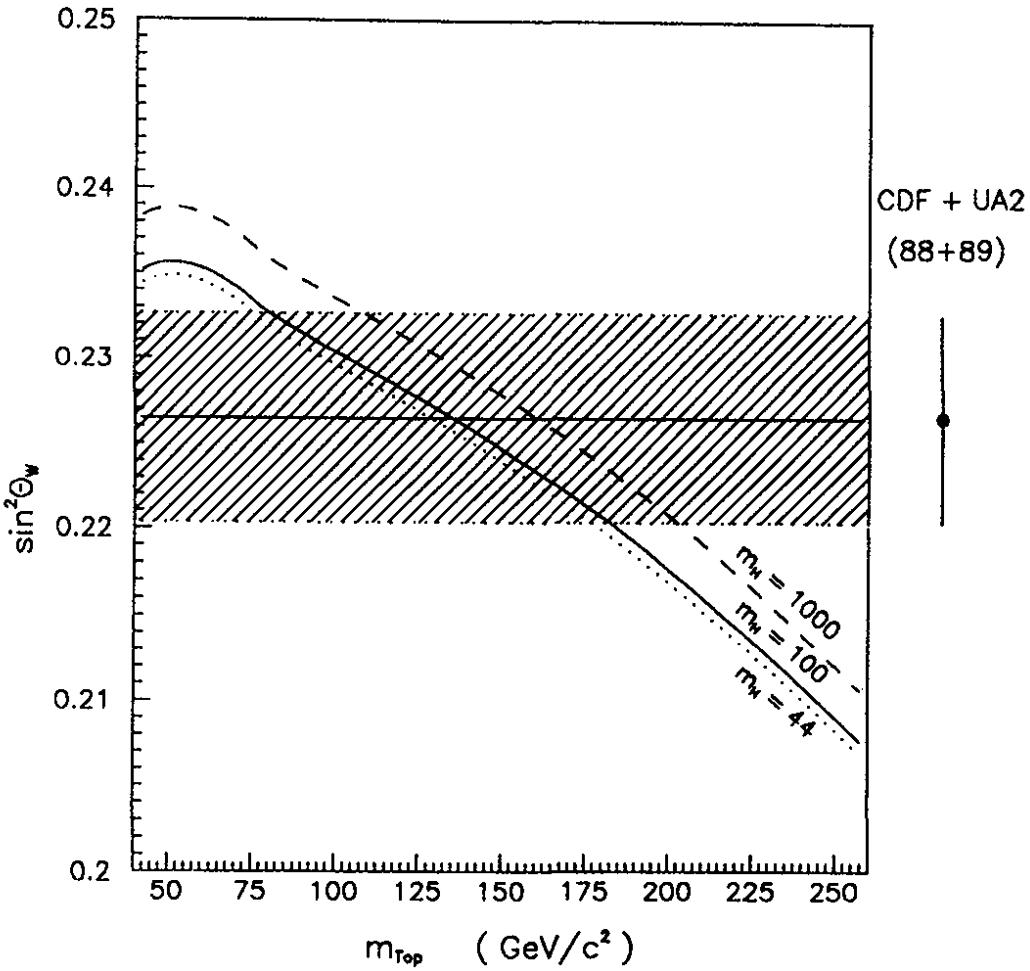

Figure 29
$\sin^2\theta_W$ as a function of m_{top}

The LEP experiments use the definition

$$\sin^2\bar{\theta}_W = 1 - \frac{m_W^2}{\bar{\rho} \cdot m_Z^2} \qquad (67)$$

with $\bar{\rho}$ given by

$$\bar{\rho} = 1 + \frac{3\sqrt{2}\, G_F}{16\pi^2} \cdot m_{top}^2 \qquad (68)$$

This definition of $\sin^2\bar{\theta}_W$ has the advantage that it is independent of m_{top} if it is determined using the leptonic width of the Z boson which is given by

$$\Gamma_Z^{\ell} = \frac{\bar{\alpha} \cdot m_Z}{12 \sin^2\bar{\theta}_W \cdot \cos^2\bar{\theta}_W} [(\frac{1}{2} - 2\sin^2\bar{\theta}_W)^2 + (\frac{1}{2})^2], \qquad (69)$$

where $\bar{\alpha}$ is the fine structure constant extrapolated to $Q^2 = m_Z^2$, and thus its measurement does not require the knowledge of m_{top}. Another independent way of measuring $\sin^2\bar{\theta}_W$ is via its determination through the Z boson mass given by the formula below

$$m_Z^2 = \frac{\pi \cdot \bar{\alpha}}{\sqrt{2}\, G_F \cdot \sin^2\bar{\theta}_W \cdot \cos^2\bar{\theta}_W} \cdot \frac{1}{\bar{\rho}} . \qquad (70)$$

This measurement depends on the top-quark mass. The measurement of $\sin^2\bar{\theta}_W$ derived from the leptonic width of the Z boson together with its determination from the Z boson mass is shown in Fig. 30 as a function of m_{top}. Also shown in Fig. 30 is the measurement of $\sin^2\bar{\theta}_W$ from the combined measurement of the $\bar{p}p$ collider and low energy νN scattering experiments as a function of m_{top}.

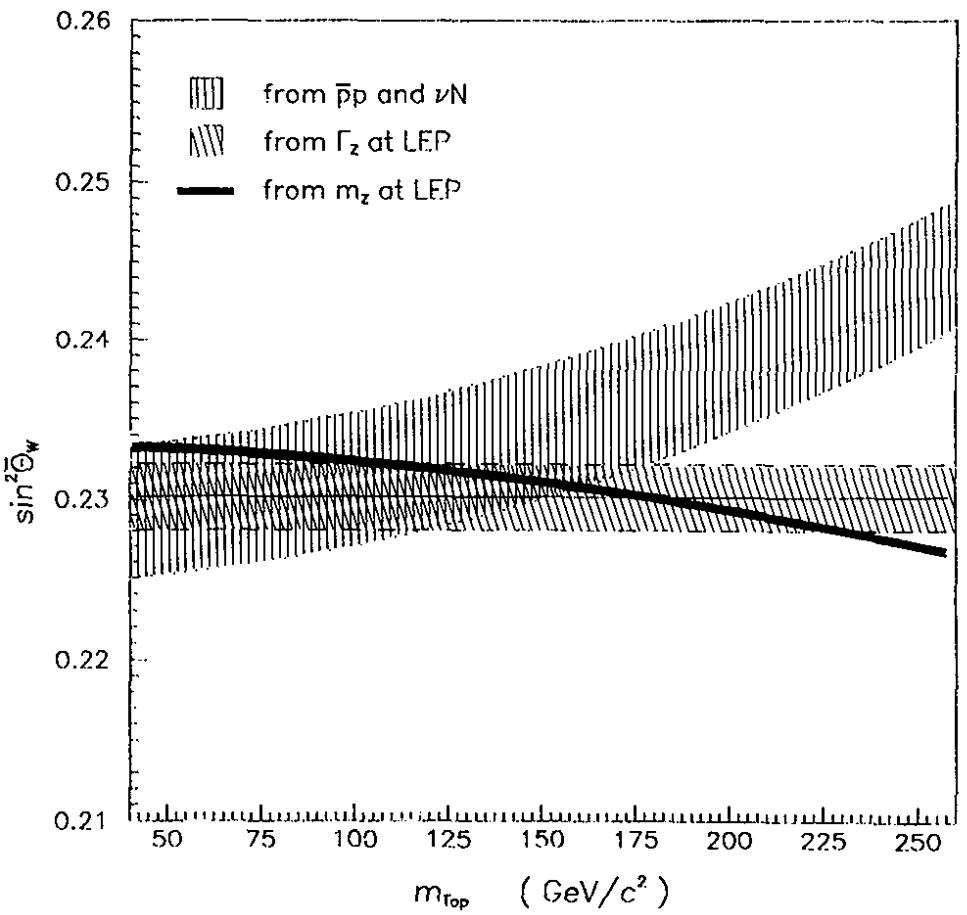

Figure 30
$\sin^2\bar{\theta}_W$ as a function of m_{top}

In the framework of the MSM all these different measurements of $\sin^2\bar{\theta}_W$ should agree with each other. Under this assumption we can use these different measurements from the LEP, UA2, CDF and the νN scattering (CDHS and CHARM) experiments to deduce the most probable value for the mass of the top-quark. Because of the weak dependence of $\sin^2\bar{\theta}_W$ on m_{top} from the LEP measurements, the sensitivity to m_{top} is given by the $\bar{p}p$ collider and the νN scattering results. Combining all these measurements together we determine the mass of the top-quark to be

$$m_{top} = 137 \pm 34 \pm 3 \pm 20 \text{ GeV}/c^2 \qquad (71)$$

where the first error comes from the combined experimental statistical and systematic uncertainty, the second error from the uncertainty on the LEP Z boson mass measurement and the third error from the uncertainty on the unknown Higgs mass varied in the range $44 < m_{Higgs} < 1000$ GeV/c^2. From Eq. (71) we can deduce an upper limit on m_{top} at the 95% confidence level which is

$$m_{top} < 202 \text{ GeV}/c^2. \qquad (71')$$

Using Eq. (71) the MSM predicts the W mass value to be

$$m_W = 80.15 \pm 0.25 \text{ GeV}/c^2. \qquad (72)$$

Note that these results on m_{top} or m_W are not an independent test of the SM, because they are based on the assumption that the MSM is valid, but from the precise measurement of m_Z and of $\sin^2\bar{\theta}_W$ by the LEP experiments the theoretical predictions on m_W could also be substantially reduced compared to Eq. (17).

A summary of all measured $\sin^2\theta_W$ values determined from various reactions including low energy and atomic physics data is shown is Fig. 31 together with their weighted average value which is determined to be

$$\sin^2\theta_W = 0.2290 \pm 0.0028 \qquad (73)$$

leaving the mass of the top-quark arbitrary. It is remarkable that all the results shown in Fig. 31 are in impressive agreement with each other, indicating the quantitative success of the Standard Model. Also this measurement can be used to

deduce an upper limit of the mass of the top-quark. We obtain

$$m_{top} < 177 \text{ GeV/c}^2 \qquad (73')$$

at the 95% confidence level for $m_{Higgs} < 1000$ GeV/c^2.

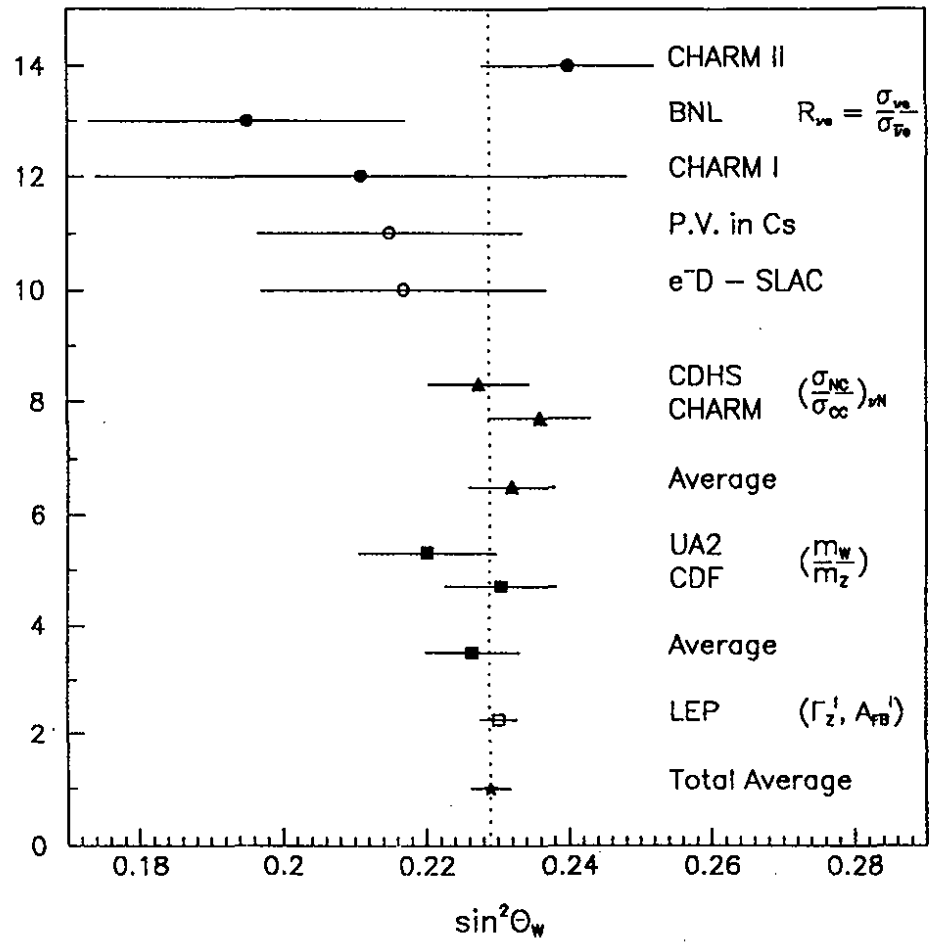

Figure 31
Summary of measurements of $\sin^2\theta_W$

ii. Any departure from the Minimal Standard Model would result in modifications to the formalism presented in Section 4.1. In particular, values of $\sin^2\theta_W$ from Eqs. (12) and (13) and from low-energy neutrino-scattering experiments would in general differ. Although all existing measurements are in agreement with the MSM, they can be used to place limits on possible deviations from the Minimal Standard Model. In particular, the quantity $\rho = m_W^2/(m_Z^2 \cos^2\theta_W)$ is expected to be 1 in the Minimal Standard Model.

The results on the ρ parameter from the $\bar{p}p$ collider experiments using $\sin^2\theta_W$ from low energy νN data are summarized in Table 13. There is good agreement between experiments and no deviation from the MSM is observed.

Table 13 : Experimental measurement of the ρ parameter

Reaction	UA1*)	UA2	CDF
e-Channel	1.010±0.028±0.020	1.014±0.012±0.009	0.995±0.012±0.009
μ-channel	1.050±0.160±0.050		

*) Values from 1985

iii. Finally, the radiative correction parameter Δr can also be extracted from the measured values of m_W and m_Z. Eliminating $\sin^2\theta_W$ from Eqs. (13) and (13') gives the following relation for Δr :

$$1 - \Delta r_1 = \frac{A^2}{m_W^2} \cdot \frac{1}{1 - (\frac{m_W}{m_Z})^2} \quad . \tag{74}$$

A more precise value (Δr_2) can be obtained using the world average $\sin^2\theta_W$ from Eq. (73) as an additional input without any assumption on ρ

$$1 - \Delta r_2 = \frac{A^2}{m_W^2} \cdot \frac{1}{1 - \sin^2\theta_W} . \tag{75}$$

Using the expectation from the MSM for the ρ parameter, ρ = 1, as a further constraint to $\sin^2\theta_W$ from the world average one gets a third estimate for Δr (Δr_3).

The result of the three estimates for Δr are shown in Table 14 for UA1, UA2 and CDF. These estimates are consistent with the expected radiative corrections (see Eq. (15)) assuming a heavy top-quark mass, even though the experimental errors are still too large to provide significant bounds on the mass of the top-quark.

Table 14 : Experimental measurement of the radiative corrections Δr

Reaction	UA1*)	UA2	CDF+)
1.) From Eqs. (13) und (13'), $\bar{p}p$ collider data alone			
e-channel	$0.037\pm0.100\pm0.067$	$0.026\ ^{+0.029}_{-0.032}\pm0.16$	$0.056\pm0.023\pm0.010$
2.) With $\sin^2\theta_W$ from νN Scattering experiments			
e-Channel	$0.128\pm0.023\pm0.060$	$0.072\pm0.011\pm0.019$	$0.052\pm0.011\pm0.006$
3.) With $\sin^2\theta_W$ from νN Scattering experiments and $\rho \equiv 1$			
e-Channel	$0.107\pm0.017\pm0.060$	$0.065\pm0.008\pm0.019$	$0.053\pm0.008\pm0.004$

*) Values from 1985
+) Electron and muon channels combined

Using the best measurement of m_W (see Eq. (62) and the best measurement of the mass ratio, m_W/m_Z (see Eq. (61)) from the $\bar{p}p$ colliders, we get

$$\Delta r = 0.045 \pm 0.020, \qquad (76)$$

where the error is obtained by adding in quadrature the statistical and the systematic uncertainty. The experimental error comes essentially from errors on the W and Z masses, as α and G_F are very well known. The error on Δr is still too large for any conclusions on the existence of radiative corrections from other than known sources. The dependence of Δr as a function of the m_{top} is shown in Fig. 32. The horizontal solid line indicates the experimental result of Eq. (76) and the one standard deviation is shown as a band. The same lower and upper limits on the mass of the top-quark (see Eqs. (65) and (65')) as for the $\sin^2\theta_W$ value are obtained.

We would like to point out that all limits on the top-quark mass should be taken with some care, because no limit on the top-quark mass could be given, if additional fermion doublets or Higgs multiplets would exist. Even if we only use the MSM prediction, it is not clear how valid the loop calculations are when the Higgs width becomes very large at high Higgs masses.

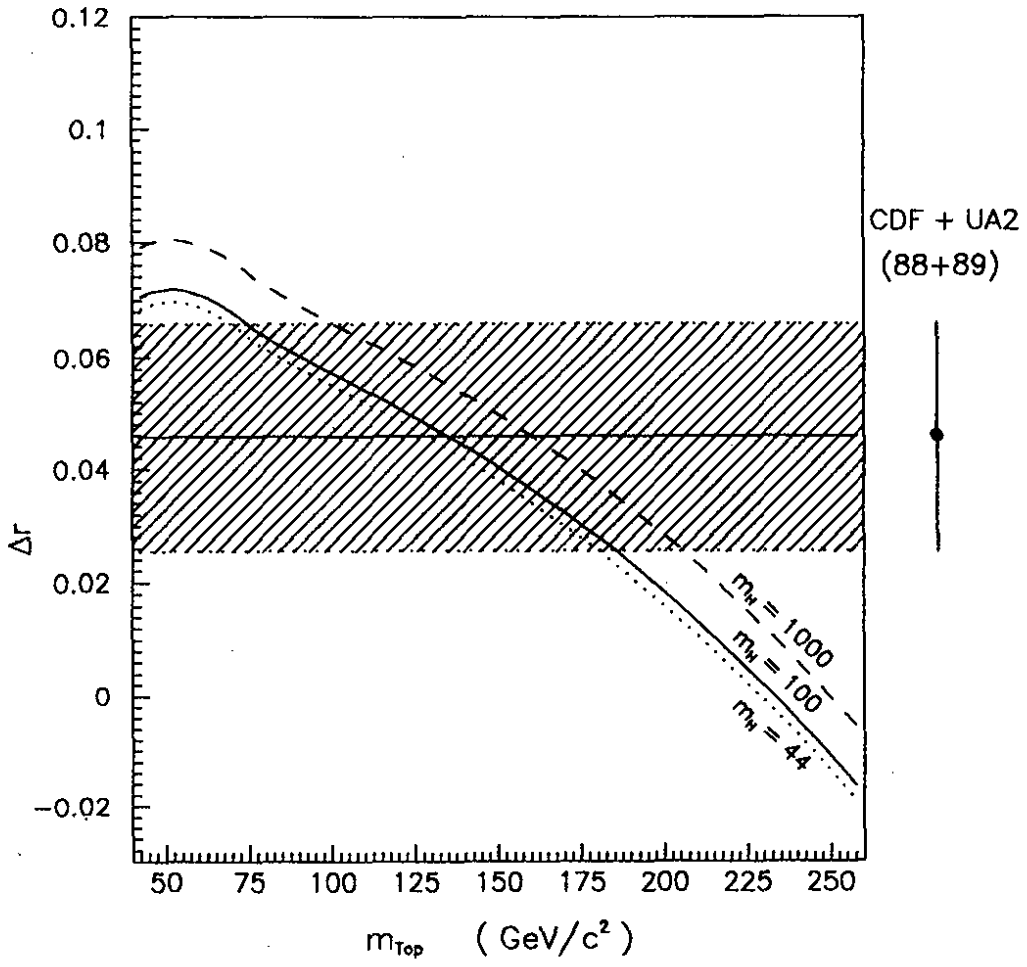

Figure 32
Δr as a function of m_{top}

A similar general test of the SM as shown in Fig. 30 can be made by studying the correlations between m_Z and the mass difference, m_Z - m_W. The mass difference measured in the electron channel by UA1, UA2 and CDF is summarize in Table 15 with the statistical and the systematic uncertainty given separately.

Table 15 : Experimental measurement of the mass difference $m_Z - m_W$

Reaction	UA1*)	UA2	CDF+)
e-Channel	10.4±1.4±0.8	10.70±0.46±0.26	11.19±0.39±0.16

*) Values from 1985
+) Electron and muon channels combined

all mass differences are given in GeV/c^2

From these recent measurements we get a combined value of

$$m_Z - m_W = 10.998 \pm 0.331. \qquad (77)$$

with the statistical and the systematic error added in quadrature.

The experimental results are also summarized in Fig. 33, where correlations between the uncertainties of the m_W and m_Z measurements are shown in the m_Z versus $m_Z - m_W$ plane. The 68% CL ellipses represent the recent UA2 measurement (dotted) and the CDF measurement (dashed). They are compared with the MSM expectations, which are based on the world average value of $\sin^2\theta_W$ from deep-inelastic νN-scattering experiments alone (wide dotted lines) and m_Z from SLC and LEP using the formula

$$m_Z - m_W = m_Z \cdot (1 - \cos\theta_W) \qquad (78)$$

or expressed in terms of A, m_Z and Δr (taking for Δr the average value form the $\bar{p}p$ collider experiments, $\Delta r = 0.045 \pm 0.020$, see Eq. (76)) leading to the formula

$$m_Z - m_W = m_Z - \sqrt{\left[\frac{m_Z^2}{2} + \sqrt{\left(\frac{m_Z^4}{4} - \frac{A^2 \cdot m_Z^2}{1 - \Delta r}\right)}\right]}. \qquad (79)$$

which is also shown in Fig. 33 (dashed lines). A combination of all measurements

from the UA2, CDF, νN and LEP experiments restricts the allowed values for m_Z and m_W to the hatched region.

The present measurements, although in very good agreement with the SM, do not provide a precise determination of Δr, as can be seen from the error ellipses. Substantially more data are needed to reduce the statistical errors which actually dominate the sensitivity on Δr. The importance of a precise measurement of Δr resides in the fact that Δr would deviate from the computed value (see Eq. (15)) if a new fermion family existed with a large mass splitting, or if there were additional gauge bosons, or again if the top quark were very heavy. A measurement of both m_W and m_Z to the 1‰ level ($\Delta m_W \sim 100$ MeV), the error on $(1 - \Delta r)$ would be at the percent level. This accuracy would then be of the same size of what a 1 TeV Higgs particle would contribute. With such an accuracy one would look to the interesting part of the radiative mass shift.

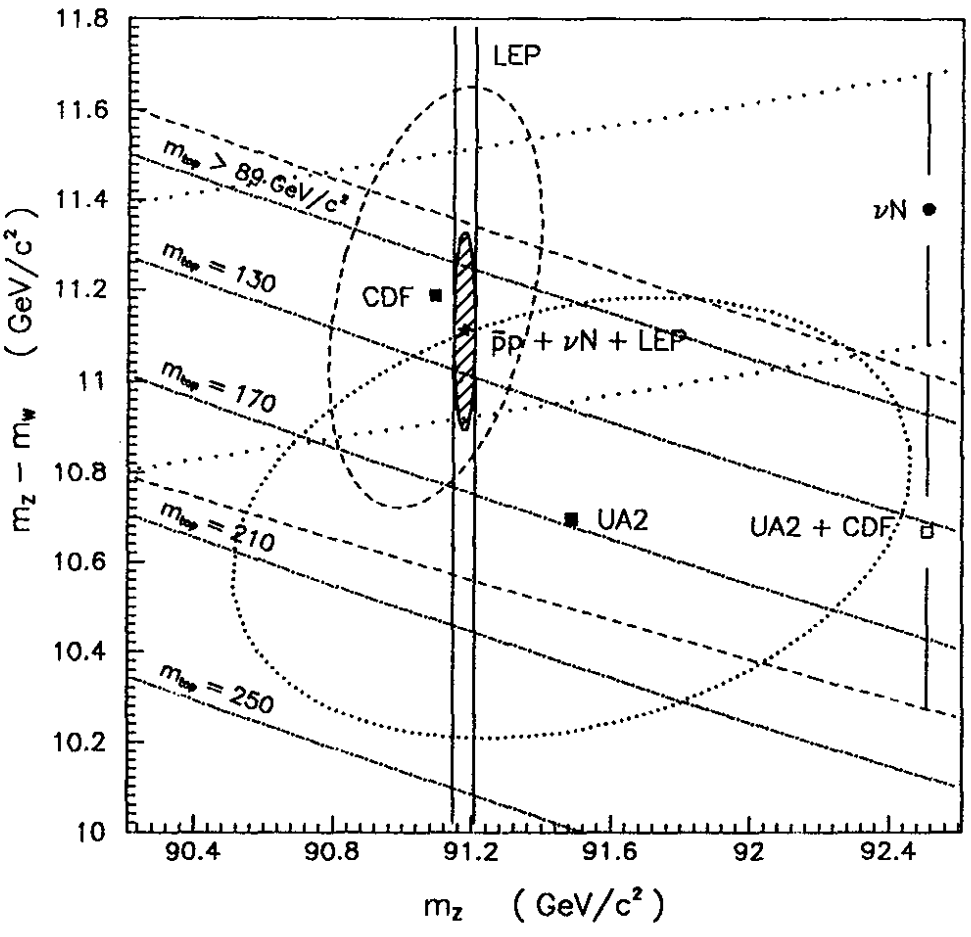

Figure 33
m_Z - m_W as a function of m_Z

7. SEARCH FOR THE TOP-QUARK

One important ingredient in the SM, the top-quark, has been the object of intensive searches over the past few years but has remained unseen. Despite the fact that the top-quark has not been found, indications for its existence are quite strong. The measurement of the b quark asymmetry ($\alpha_b = 1.008 \pm 0.29$ [63]) in e^+e^- annihilation experiments indicates that the b quark has an asymmetry for a member of a left-handed doublet and right-handed singlet structure as expected in the SM of electroweak interactions under SU(2), suggesting that it should have a partner, namely the top-quark. Calculations [64] show that the mass of the top-quark, m_{top}, must be less than ~ 200 GeV/c^2 in the MSM, if the model is to remain consistent within the body of the experimental data. Experimental searches at e^+e^- machines [65] and at hadron colliders [66] have failed to find any evidence for the top-quark with a mass lower than 41 GeV/c^2 at the 95% confidence level. In the previous sections we have given upper and lower bounds on the top-quark mass by indirect methods (see Eqs. (63), (63'), (65), (65') and (71')), while in this chapter we report on recent direct searches for the top-quark.

7.1 Theoretical predictions on top-quark production and decay

Top-quarks could be produced at $\bar{p}p$ colliders from two dominant processes:

i) the weak interaction process ($t\bar{b}$)

This process occurs via W production, $\bar{p}p \rightarrow W + X$ with the W decaying subsequently into $W^+ \rightarrow t\bar{b}$ and $W^- \rightarrow \bar{t}b$, if kinematically allowed ($m_{top} < m_W - m_b$). The production cross section can be precisely estimated from the relation

$$\sigma(W \rightarrow t\bar{b}) = 3 \cdot \sigma(W \rightarrow \ell\nu)\, PS(m_{top}) \cdot K_{QCD} \qquad (80)$$

where $\sigma(W \rightarrow \ell\nu)$ is the cross section for leptonic decays of the W boson which has been measured at the CERN and the TeV-I $\bar{p}p$ collider (see Table 2), $PS(m_{top})$ is a known phase space suppression term, K_{QCD} is a correction factor (> 1) to take into account higher order QCD corrections, which become important if the mass of the top-quark is close to the mass of the W [67], and the factor 3 is due to colour.

ii) the strong interaction process ($t\bar{t}$)

This process ($\bar{p}p \rightarrow t\bar{t} + X$) occurs via $q\bar{q}$ annihilation or gluon-gluon fusion. A recent complete calculation [68] of the next-to-leading order QCD corrections to the

total cross section for $t\bar{t}$ production, $\sigma(t\bar{t})$, has allowed the authors of Ref. [69] to give reliable predictions for top production by using a set of proton density functions which include the latest experimental results [39]. The uncertainty of $\sigma(t\bar{t})$ is estimated to be $\pm$ 30%, mainly due to uncertainties in Λ_{QCD} and the Q^2 scale.

The inclusive production cross section of t or $\bar{t}$ as a function of m_{top} is shown in Fig. 34 for centre-of-mass energies of 630 GeV and of 1.8 TeV as bands indicating the theoretical uncertainties.

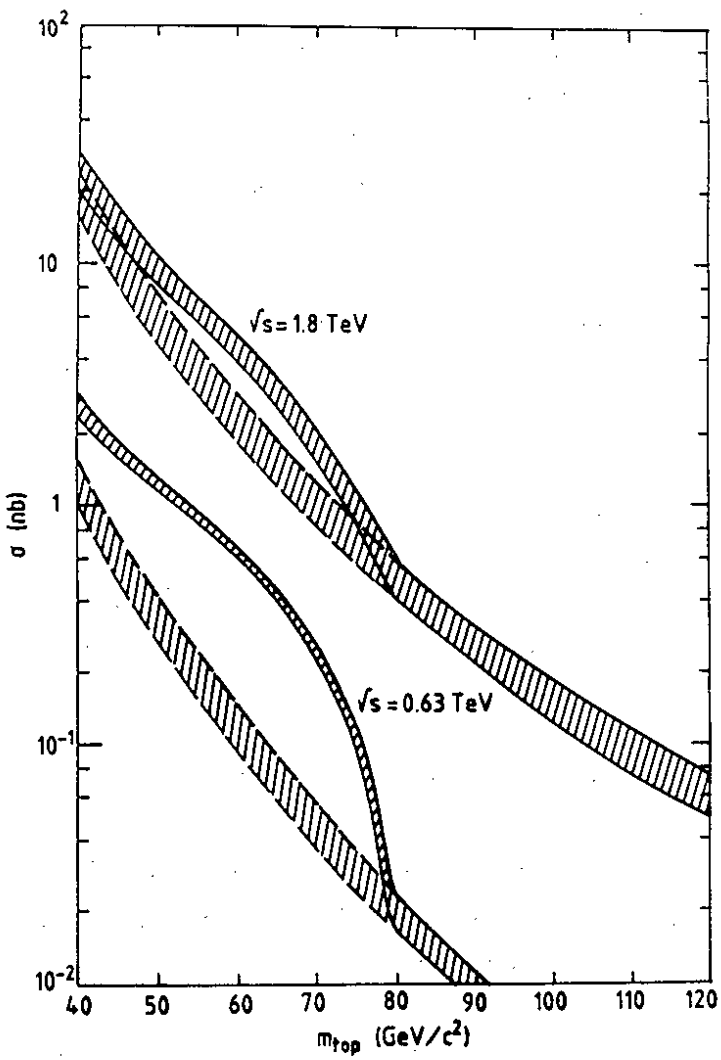

Fig. 34
Inclusive production cross section for t ($\bar{t}$) as a function of m_{top} at $\sqrt{s}$ = 630 GeV and 1.8 TeV

There is a large increase of the inclusive top-quark cross section with the centre-of-mass energy (i.e., at $m_{top} = 80$ GeV/c^2 the increase between $\sqrt{s} = 0.63$ and 1.8 TeV amounts to about a factor of 25, which is a substantial advantage for the FNAL collider). At TEV-I energies $t\bar{t}$ is dominant for any value of m_{top}, whereas at the CERN energy the $W \rightarrow t\bar{b}$ contribution is dominant for top masses in the range of $40 < m_{top} < 75$ GeV/c^2, but the advantage for the FNAL collider is still a factor 4 to 10 depending on the top-quark mass.

Top decay proceeds through virtual W exchange as

$$t \rightarrow (Wb) \rightarrow 3 \text{ jets} \quad \text{or} \quad t \rightarrow (Wb) \rightarrow \ell\nu_\ell + \text{jet}.$$

The final state will therefore consist of at least 4 jets or a charged lepton accompanied by at least two jets in events with missing transverse energy. Given the high rate of multi-jet events from QCD processes, the interesting final states at $\bar{p}p$ colliders are those containing semileptonic decay modes which, at the price of a branching ratio of 1/9 for each charged lepton, give a much cleaner signature.

Background events faking the above signature come mainly from two sources: In the kinematical region of low lepton-neutrino transverse masses and small missing transverse momenta pathological QCD jets and semileptonic $b\bar{b}$ decays dominate, whereas in the region of high transverse masses and large missing transverse momenta contributions from the W + jet(s) production dominate. These backgrounds show an event pattern which is very similar to that expected for top-quark events. Therefore it is impossible to identify the top-quark candidates on an event-by-event basis. Only statistical arguments can be used to extract a top signal.

7.2 Experimental searches for the top-quark

The UA1 experiment has only μ detection capability since 1987. The UA2 experiment can only detect electrons, whereas CDF has both, e and μ detection. New results on searches using (ℓ + n jets) events with the associated quark (t or b) decaying into jets have been reported by UA1 for μ + 2 jets [70], and by UA2 [71] and CDF [72] for e + $\geq$ 1 jet. UA1 has also reported a search for top using ($\mu\mu$ + jet) events [70], and CDF a search for top using (eμ + anything) events [73], which requires that both t and $\bar{t}$ decay semi-leptonically. The lepton plus jets mode has the advantage of higher rate than the lepton pair channel and can therefore probe heavier top masses. The (e-μ) channel has

the largest di-lepton rate, does not suffer from Drell-Yan backgrounds and can be used effectively at low top masses where backgrounds in the e + jet channel are high.

7.2.1 Top searches in ℓ + n jets events

The signature of the semi-leptonic decay of the top-quark consists of events containing one lepton, one or more hadronic jets from the associated t or b quarks, and a transverse momentum imbalance ($\not{p}_T$) due to the neutrino produced in the top decay. Because of the large top mass ($m_{top} > 41$ GeV/c^2) considered here, the lepton and jets will be produced preferentially in the central region, in contrast to most background processes, and the following properties are expected for the signal events:

i) the lepton should be isolated,
ii) there should be a sizeable missing p_T ($\equiv p_T^{\nu}$) in the event,
iii) the angular separation between the highest transverse energy jet and the lepton should have a wide distribution.

For most of the background processes faking the above top signature several of the above conditions are not fulfilled, and can therefore be used for rejection. However, a notable exception is the background with large transverse lepton energy, E_T^{ℓ}, and large missing transverse momentum, p_T^{ν}, due to $\bar{p}p \rightarrow$ W + jets production with subsequent leptonic decay of the W which fulfills all three conditions. At low lepton E_T^{ℓ} and p_T^{ν}, background from b quark production can be suppressed by requiring that the charged lepton be isolated. Both backgrounds are strongly reduced by confining the top searches to a range of moderate ($\ell\nu\ell$) transverse mass values. The relative importance of the various background contributions depends strongly on the event selection. As an example, for the UA1 analysis the largest background contribution is due to $\bar{p}p \rightarrow b\bar{b}$ + X, whereas this background is small in the UA2 and the CDF analysis where the W + jets background is dominant.

7.2.1.1 Top search in μ + 2 jets events

UA1 [70] reported on a top-quark search in μ + 2 jets events based on an integrated luminosity of 4.6 pb^{-1}. The selection criteria are as follows : $p_T^{\mu} > 12$ GeV/c, $E_T^{jet1} > 13$ GeV, $E_T^{jet2} > 7$ GeV and $m_T^{e\nu} < 60$ GeV/c^2. They use an isolation criteria, I_{iso}, on the muon which is characterized by the amount of transverse energy within a cone of radius $\Delta R = \sqrt{(\Delta\eta^2 + \Delta\phi^2)} = 0.7$. The isolation distribution is shown in Fig. 35. A limit on the top mass is derived from a comparison of the isolation distribution for the

event sample with that expected from the background and from a possible top-quark contribution, as shown in Fig. 35. The Monte Carlo simulation is checked using a control data sample where a possible contribution from the top-quark is negligible.

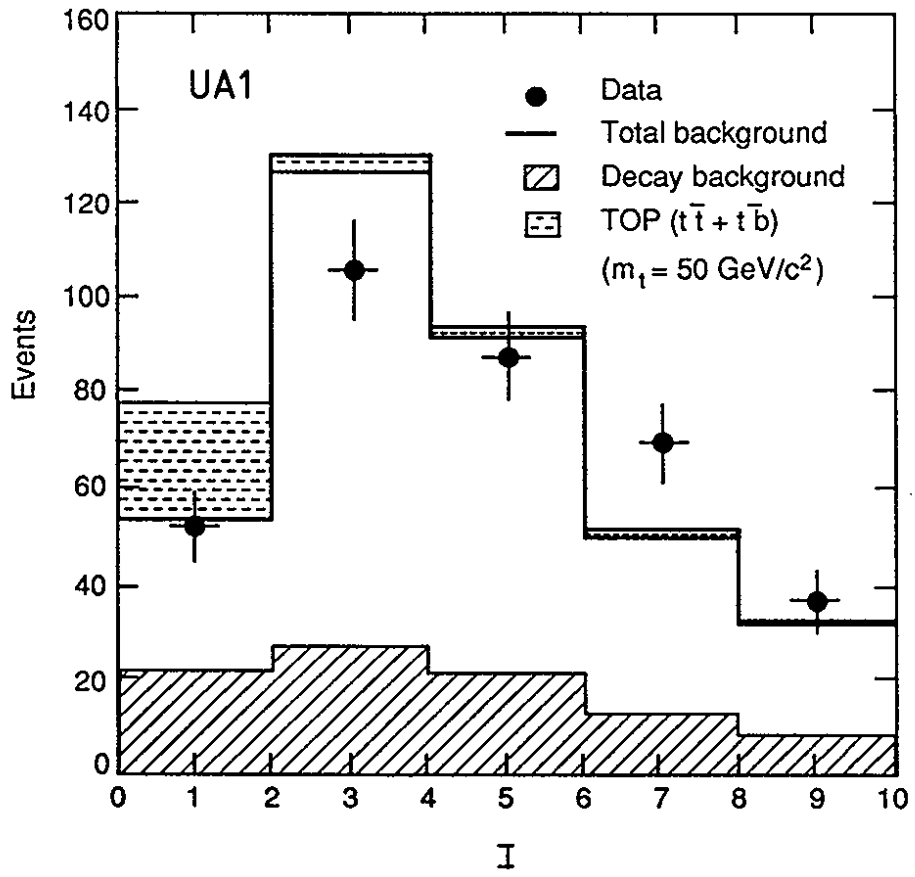

Fig. 35
Distribution on Isolation in μ + 2 jets events from UA1

The first bin of the distribution on the muon isolation in Fig. 35, where most of the top signal would be expected, has 76 events for a calculated background of 77 ± 10 events. The expected contribution from a top-quark decreases from 39 events for $m_{top} = 40$ GeV/c^2 to 5 events for $m_{top} = 70$ GeV/c^2, with an estimated systematic uncertainty of 25%. The lower limit for the mass of the top-quark obtained from this analysis is $m_{top} > 53$ GeV/c^2 at the 95% confidence level.

7.2.1.2 Top search in e + n jets events

A search for the top-quark in e + n jets events ($n \geq 1$) has been reported by UA2 [71] based on an integrated luminosity of 7.4 pb^{-1}, and by CDF [72], based on an integrated luminosity of 4.4 pb^{-1}. Both analyses are very similar. Cuts on the electron transverse energy are used for trigger and event selection, cuts on p_T^{ν} and topological cuts of at least one jet in the final state for background suppression. Limits are then obtained from the e + ≥ 1 jet(s) event rate and from the shape of the $m_T^{e\nu}$ distribution.

The main selection criteria are here:

a) for UA2: $p_T^e > 12$ GeV/c in the range $|\eta| < 1.0$, $p_T^{\nu} > 15$ GeV/c, $E_T^{jet1} > 10$ GeV in $|\eta| < 2.2$ and $\Delta\phi(e, jet1) > 160°$, where jet1 is the highest energy jet in the event. The UA2 electron selection implies isolation.

b) for CDF: which uses somewhat harder cuts; $p_T^e > 20$ GeV/c in the range of $|\eta| > 1.1$, $p_T^{\nu} > 20$ GeV/c, E_T^{jet1} and $E_T^{jet2} > 10$ GeV in $|\eta| < 2.0$, momentum balance of the charged track pointing to the cluster, $E_T < 1.5 \cdot p_T$, and also an isolation cut, $E_T^{iso} < 2.0$ GeV.

Both experiments compare the measured shape of the electron-neutrino transverse mass distribution, $m_T^{e\nu}$, with the expected distribution from top-quark events which has been corrected for acceptance and efficiency losses.

For UA2 the $m_T^{e\nu}$ distribution of the 137 selected events is shown in Fig. 36. Due to the selection criteria used, which strongly reduces other background sources, such as $b\bar{b}$, the W + jets background is dominant, as shown by the Jacobian peak in Fig. 36.

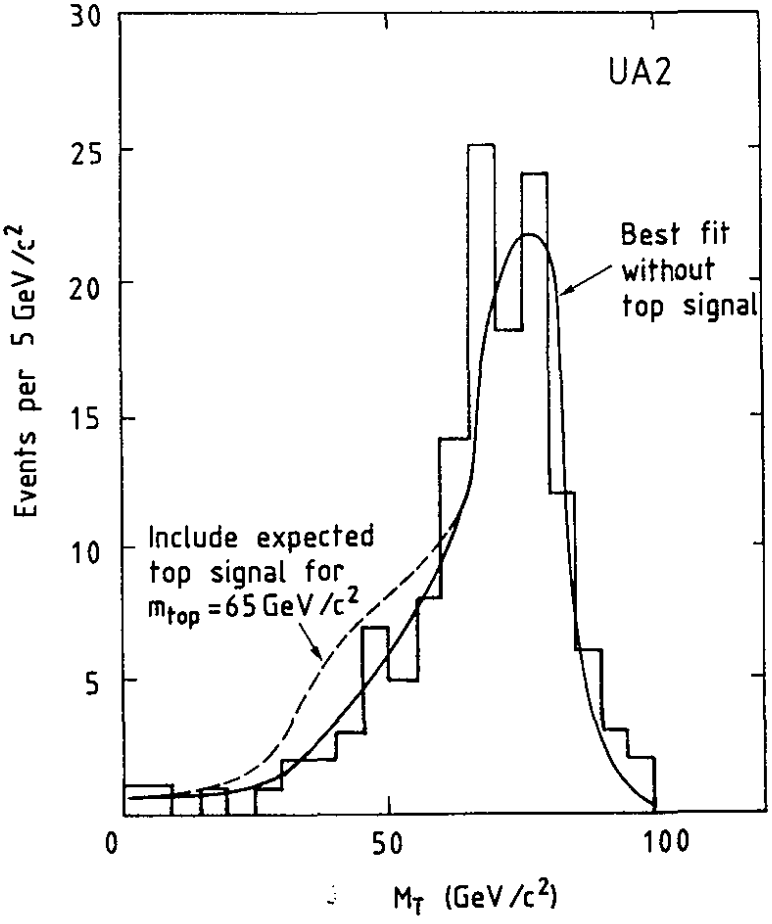

Fig. 36
Transverse mass distribution for e + ≥ 1 jet(s) events from UA2

CDF retains 104 events that satisfy the tight selection, for which the m_T^{ev} distribution is shown in Fig. 37. Shown for comparison are the expected m_T^{ev} distributions for $t\bar{t}$ and W production. Also here the W + jets background is dominant. The $t\bar{t}$ distribution is obtained from a Monte Carlo calculation with $m_{top} = 70$ GeV/c^2. The W + 2 jets events were generated according to a QCD calculation with a W mass of $m_W = 80$ GeV/c^2. The detector response was simulated for both MC event samples.

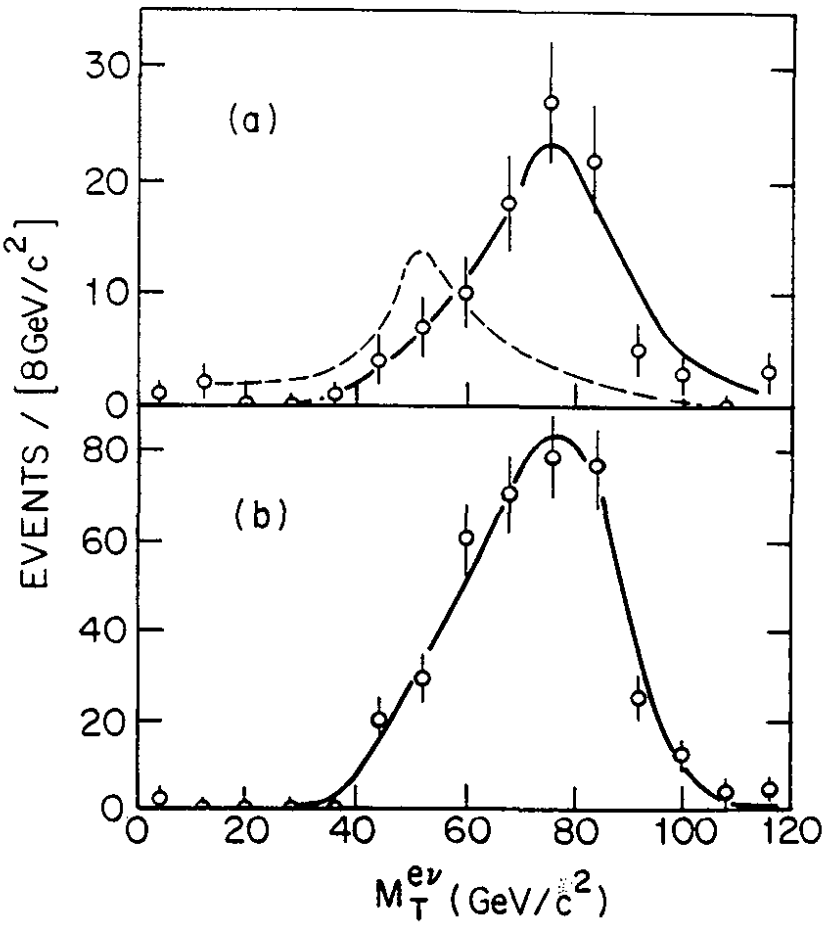

Fig. 37
Transverse mass distribution for e + ≥ 1 jet(s) events from CDF

The data from UA2 as well as from CDF are consistent with W + jet(s) predictions and show no evidence for top-quark production. A limit is extracted from likelihood fits to the observed number of events with two free parameters corresponding to the fraction of the event sample due to top-quark decays and W events. UA2 excludes top-quark masses between $30 < m_{top} < 69$ GeV/c^2, whereas CDF excludes top-quark masses between $40 < m_{top} < 77$ GeV/c^2 at the 95% confidence level.

7.2.2 Top search in lepton pair + jet events

The lepton pair production in association with jets, where each of the top-quarks decays semileptonically is another channel to look for top-quark production.

7.2.2.1 Top search in 2μ + jet events

Although requiring two semileptonic decays to occur within the same event is an efficient way to reduce the background, the extra 1/9 branching ratio factor is a heavy penalty to pay. The low values of the momentum threshold of the two muons, 8 GeV/c and 3 GeV/c, respectively, which are used in the UA1 analysis [70] partially compensate for this loss by increasing the acceptance. The data sample corresponds to an integrated luminosity of 5.4 pb^{-1}. A limit of $m_{top} > 46$ GeV/c^2 at a 95% confidence level is obtained.

7.2.2.2 Top search in eμ + X events

The double-semileptonic decay of a $t\bar{t}$ pair (one top-quark to $e\nu_e b$ and and the other to $\mu\nu_\mu b$) with an assumed branching ratio of 2/81, contributes more than 80% of the signal. By requiring two leptons from different families, backgrounds from Drell-Yan and Z^0 production and QCD production of W + jets are strongly suppressed.

The selected signal region for events with at least one electron and one muon candidate is $E_T^e > 15$ GeV and $p_T^\mu > 15$ GeV/c. From the observation of one eμ candidate in this region (for which a firm conclusion about its origin is not possible), using the expected $t\bar{t}$ event rate and taking into account statistical and systematic uncertainties, CDF excludes top-quark production in the mass range 28 GeV/c^2 < m_{top} < 72 GeV/c^2 at the 95% confidence level.

7.3 Summary of the limits for the top-quark search

In combining the results from all available data on e + jets, μ + jets, μμ + jets and e + μ, from the 1988-1989 runs and from earlier ones, the UA1 experiment reports an overall limit on the top-quark mass $m_{top} > 60$ GeV/c^2 at the 95% confidence level. The UA1 experimental cross section limit as a function of m_{top} is shown in Fig. 38 (hatched area). Also shown are the predictions for the $W \rightarrow t\bar{b}$ contribution alone (dashed line) and for the total inclusive top production cross section (solid line).

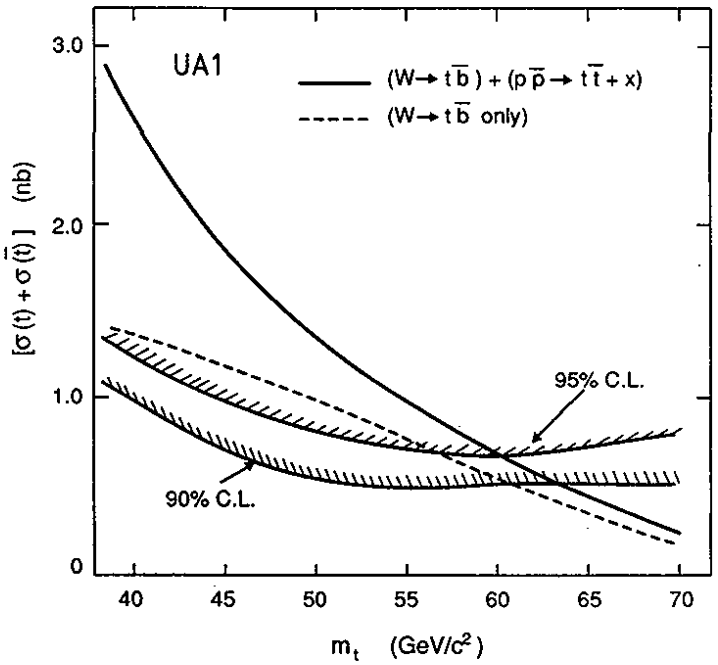

Fig. 38

Inclusive production cross section for t ($\bar{t}$) as a function of m_{top} from UA1

The UA2 results are shown in a similar way in Fig. 39. Their limit on the mass of the top-quark is $m_{top} > 69$ GeV/c^2 at the 95% confidence level.

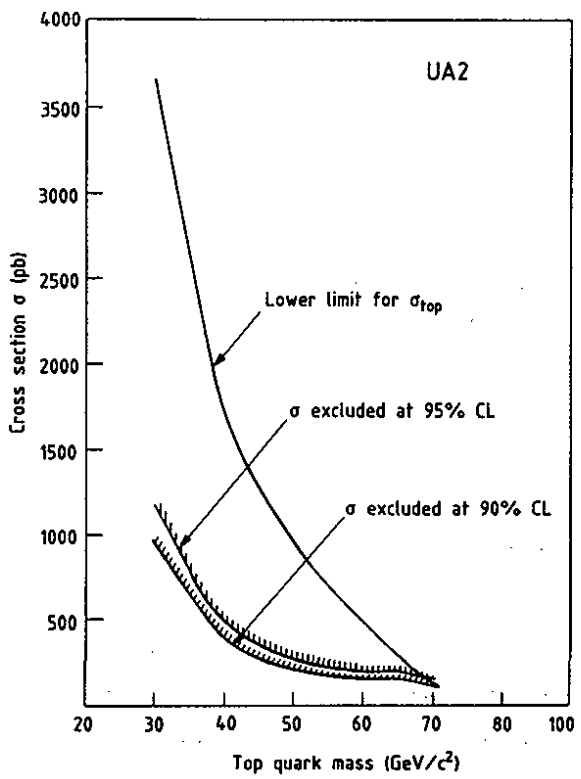

Fig. 39

Inclusive production cross section for t ($\bar{t}$) as a function of m_{top} from UA2

The differences seen in Fig. 38 and 39 between the predicted cross sections for the two experiments come from two sources:

i. For the $t\bar{t}$ cross section UA1 uses the central value with an allowance for a ±30% uncertainty in the fit, whereas UA2 uses the lower theoretical estimate (-30%).
ii. For the $W \rightarrow t\bar{b}$ cross section UA1 uses a radiative correction factor $K_{QCD} > 1.0$ which depends upon m_{top} with an assigned error, whereas UA2 considers that the value of K_{QCD} is not well established and uses conservatively $K_{QCD} = 1.0$.

The combined effects of those differences on the mass limits of the top-quark are not expected to be large.

Lower limits on a hypothetical member of a new quark family (b'), assuming that its partner is too heavy to allow production mediated by the weak interaction and that its decay matrix element is identical to that of a top-quark, were also given. Assuming that the b' branching ratio to a charm quark and a virtual W boson is 100%, the lower limits are $m_{b'} > 41$ GeV/c^2 (UA1) and $m_{b'} > 53$ GeV/c^2 (UA2) at the 95% confidence level.

The results from the CDF experiments for the e + jets search are shown in Fig. 40a. Their limit on the mass of the top-quark is $m_{top} > 77$ GeV/c^2 at the 95% confidence level. From the e - μ channel they exclude a top-quark in the mass range 28 GeV/c^2 < m_{top} < 72 GeV/c^2 at the 95% confidence level. This limit also applies to a hypothetical fourth generation b' quark.

While preparing this review, a new lower limit on the mass of the top-quark of

$$m_{top} > 89 \text{ GeV}/c^2 \qquad (81)$$

at the 95% confidence level has been quoted by CDF [74] which is the most stringent lower bound reached so far. This result is obtained by combining the e-e, e-μ and the μ-μ results together with the results from a new analysis of eν + jets and μν + jets events, in which the large W + jets background is strongly reduced by the additional requirement of a low p_T muon, as expected from b-decay. The lower bound for m_{top} using the expected dependence of the cross section on m_{top} for all measurements for lepton pairs from the CDF experiment is shown in Fig. 40b.

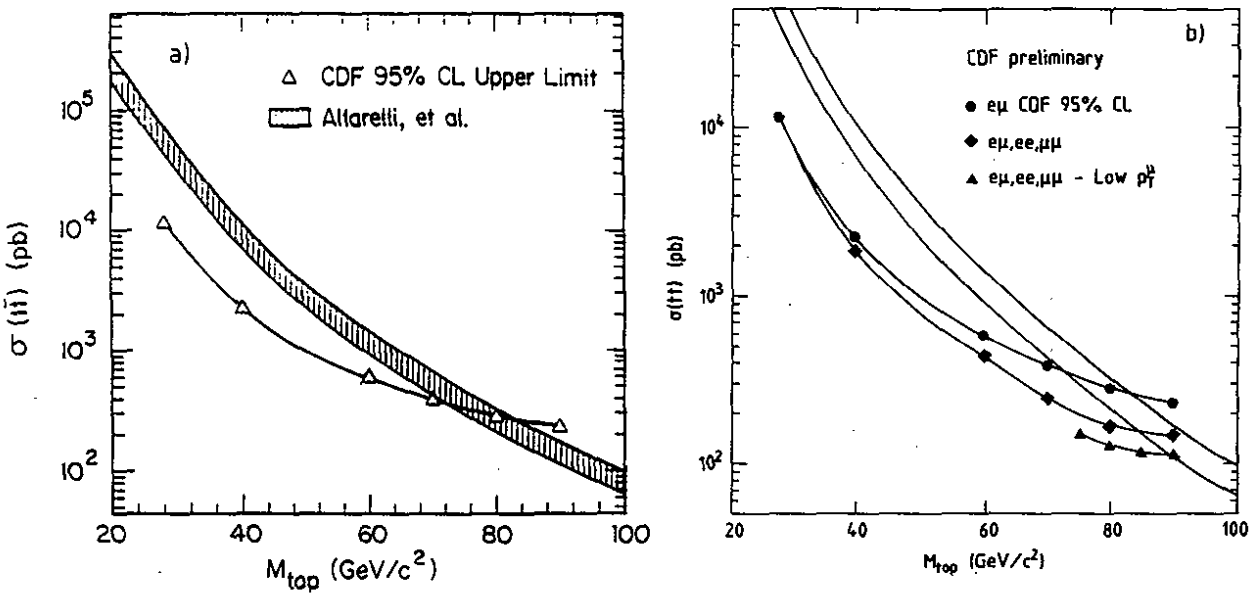

Fig. 40

Inclusive production cross section for $t\bar{t}$ as a function of m_{top} from CDF :
a) for the e + jet sample b) for lepton pairs.

For masses of the top-quark approaching m_W the b jets are softer and therefore it becomes more and more difficult to distinguish $W \rightarrow t\bar{b}$ from W + jets production. On the other hand for the same kinematical reasons the $t\bar{t}$ channel will result in a final state containing a $\ell\nu\ell$ and a two-jet pair with invariant masses close to m_W. These two features makes it very difficult to distinguish the top-quark from the W, if m_{top} is around the W mass. All the present data suggest a mass of the top-quark heavier than the W mass, although it is not completely ruled out that its mass may be slightly below m_W, given the large uncertainties and the small event rates. More data are needed to confirm the first hypothesis. For $m_{top} > m_W$ the most promising channel is $t\bar{t} \rightarrow W^+W^- b\bar{b}$ followed by a semileptonic decay of one of the W's. In view of the much higher cross section at the TEV-I energy and of the already reported limit of 89 GeV/c^2 for the mass of the top-quark by the CDF experiment, the top-quark is probably out of reach for the CERN collider experiments. It will be found by CDF and D0 in the coming runs starting in summer of 1991, if its mass is not heavier than ~ 130 Gev/c^2. If that is not the case then the top-quark is so heavy that it is also out of reach for LEP phase II, and then its detection has to wait until the new hadron colliders, SSC and LHC, become operational.

8. SEARCHES FOR HEAVY IVB', IVB PAIR AND HIGGS PRODUCTION

The results on W and Z production and decay properties show impressive agreement with the current MSM expectations. In this chapter we discuss results on searches for exotic processes like heavy Z's and W's. Also IVB pair and Higgs production are shortly mentioned.

8.1 Search for heavy W' and Z' Vector Bosons

Additional Vector Bosons arise naturally in many possible extensions of the MSM of electroweak interaction, i.e. either through right handed currents, composite models or various models derived from superstring theories [75]. Massive bosons, decaying into lepton pairs, will produce more energetic decay products compared to the standard IVBs, resulting in improved energy resolution and detection efficiency in the electron channel.

UA1 has reported upper limits [44] on W' and Z' production from the 1982 - 1985 data. They have simulated W' (Z') production and decay using standard couplings and different sets of parton density functions. They have taken into account the mass dependent selection efficiencies for W' (Z'), which increase from 61% for $m_W = 80$ GeV/c^2 to 72% for $m_W = 250$ GeV/c^2 and similar for the Z' case. The calculated $\sigma \cdot B_{IVB}$ was renormalized to the measured cross sections for standard IVB production for $\sqrt{s} = 630$ GeV. The $W \rightarrow e\nu$ data at $\sqrt{s} = 546$ GeV have been included in the data sample with appropriate weights to increase the statistics. The events from $W \rightarrow \mu\mu$, $\tau\nu$ and $Z \rightarrow \mu\mu$ are not included in the analysis due to the poorer resolution in the transverse mass or invariant mass distribution. UA1 has obtained an upper limit for the production and decay of massive W (Z)-like objects decaying into lepton pairs of

$$(\sigma \cdot B)_{W'} < 4.1 \text{ pb} \quad \text{and} \quad (\sigma \cdot B)_{Z'} < 4.2 \text{ pb} \qquad (82)$$

at the 90% confidence level. These values can be converted into lower mass limits of the W' and Z'

$$m_{W'} \geq 220 \text{ GeV}/c^2 \quad \text{and} \quad m_{Z'} \geq 173 \text{ GeV}/c^2 \qquad (83)$$

at the 90% confidence level.

Using the 1988 and 1989 data UA2 has performed a preliminary analysis [76] using log likelihood methods. UA2 has obtained an upper limit for the production and decay of massive W (Z)-like objects decaying into lepton pairs resulting in upper limits for W' and Z' masses for standard couplings of

$$m_{W'} \geq 247 \text{ GeV}/c^2 \quad \text{and} \quad m_{Z'} \geq 216 \text{ GeV}/c^2 \qquad (84)$$

at the 95% confidence level.

CDF has inspected their data sample of Drell-Yan pairs for Z^0's from a di-photon hardware trigger which leaves 597 events. These data are consistent with Z^0 and Drell-Yan expectation. The overall efficiency quoted is 66%, and there are no events above $m_{ee} = 200$ Gev/c^2. This provides a preliminary cross section [77] for the production and decay of massive Z-like objects decaying into electron pairs of

$$(\sigma \cdot B)_{Z'} < 1.6 \text{ pb} \qquad (85)$$

at the 95% confidence level, which, for standard couplings, corresponds to a lower limit for the mass of a Z' of

$$m_{Z'} > 380 \text{ GeV}/c^2 . \qquad (86)$$

A similar analysis has been performed for W's. No events have been found with transverse masses above 150 GeV/c^2. With a quoted efficiency of 12% for electrons in the central region ($|\eta| < 1.1$), a preliminary cross section times branching ratio [77] of

$$(\sigma \cdot B)_{W'} < 7.6 \text{ pb} \qquad (87)$$

at the 95% confidence level, which, for standard couplings, corresponds to a lower limit for the mass of a W' of

$$m_{W'} > 478 \text{ GeV}/c^2. \qquad (88)$$

These are the best lower limits obtained so far on heavy W' and Z' production decaying into lepton pairs using standard couplings.

8.2 Search for IVB pair production

The physics potential of studies of electro-weak gauge-boson pair production was recognized long time ago [78]. Unfortunately, the rates for Vector Boson pair production at the present colliders are too low to allow detailed studies of these potentially very interesting events which result from the Vector Boson self-interactions predicted by the Standard Electroweak Theory. Multi-jets from QCD production are produced with substantially higher cross section than Vector Boson pairs . Therefore this background will swamp the purely hadronic signal for Vector Boson pair production. Also the W and Z cross section with associated QCD production is well above the IVB pair production. Therefore only analyses with the gauge bosons decaying semileptonically can be considered. The observation of these events would be a stringent test of the theory. As an example, we have calculated the expected rate for W pair production with subsequent decay of the two W's into a lepton-neutrino pair with each of the leptons exceeding 25 GeV/c transverse momentum in the rapidity range of $|\eta| < 2.5$. Such a rate amounts to 0.18 events for 10 pb^{-1} at TEV-I energy.

LEP II will produce W-boson pairs very close to threshold ($\sqrt{s} \approx$ 180-200 GeV). Any deviation of SM couplings, such as anomalous Vector Boson self-interactions, leads to amplitudes which grow with energy and are therefore more apparent at higher Vector Boson pair invariant masses. This effect may be a good argument for a future hadron collider such as LHC or SSC, because it may be a more sensitive probe of Intermediate Vector Boson self-interactions than at LEP II [79].

Hadron colliders are capable of producing Intermediate Vector Boson pairs in both the charged and neutral channels. We have studied in some detail the WZ pair production with subsequent semi-leptonic decay of both the W and the Z, leading to a final state of three leptons and missing transverse momentum at LHC energies. We have found that the signal is well above the background expected from either $t\bar{t}$ with t or $\bar{t}$ decaying semileptonically and one of the cascaded b's also decaying semileptonically, or Z + jet production with the $Z \rightarrow ee$ and the jet fragments faking an electron, by at least one order of magnitude. We have also found that anomalous couplings could be tested to the 2 - 4% level by comparing the shapes of the transverse mass spectrum of the WZ pair, a variable which is easily measurable by experiment and has no ambiguity due to the unknown longitudinal momentum of the neutrino [80]. This gives about one order of magnitude better sensitivity than LEP II.

8.3 Search for the Higgs boson

The Higgs mechanism [81], which is still not established, is an essential ingredient of the SM. In its minimal version (MSM) the SM predicts the existence of one neutral scalar Higgs particle, H^o, with well defined couplings but undefined mass. At present $\bar{p}p$ colliders, the dominant production mechanism is through gluon-gluon fusion with subsequent decay of the Higgs boson into the heaviest fermion pair ($b\bar{b}$), if m_{Higgs} is larger than 10 GeV/c^2. Because of the enormous background from hadron jets by several orders of magnitude the observation of Higgs production through gluon-gluon fusion is practically excluded even with an experiment optimized for b-quark tagging. A more promissing production process is the so-called Higgs bremsstrahlung mechanism, with the associated W (Z) and Higgs production which is the dominant source of Higgs production at e^+e^- colliders.

CDF has searched for a light Standard Model Higgs boson produced in association with an IVB (W or Z). If a Higgs boson exists with a mass $m_{H^o} < 1$ GeV/c^2 then of the order of 1% of W and Z bosons at the TEV-I energy are expected to be accompanied by a Higgs boson. If the Higgs boson mass lies between the $\mu^+\mu^-$ and $\rho^-\rho^+$ decay thresholds ($2m_\mu < m_{H^o} < 2m_\rho$) it is expected to have a lifetime of less than 10^{-14} sec and large branching fractions to a charged particle pair ($\mu^+\mu^-$, $\pi^+\pi^-$ or K^+K^-). CDF has therefore looked for an excess of events with isolated high transverse momentum track pairs in W and Z events with a mass of the pair in the region $2m_\mu < m < 2m_\rho$. The results [82] are based on an analysis of 5422 W decay candidates and 480 Z decay candidates. No event has been found. A Higgs boson with a mass m_{Ho} in the intervals $211 < m_{H^o} < 820$ MeV/c^2 and $844 < m_{H^o} < 987$ MeV/c^2 can therefore be excluded at the 90% confidence level.

The best experimental limits on the mass of the neutral Higgs particle come from LEP experiments [83] via the reaction $e^+e^- \rightarrow H^oZ^{o*}$ where the virtual Z decays into a pair of fermions. The presently best limit obtained is

$$m_{Higgs} > 44.0 \text{ GeV}/c^2 \qquad (89)$$

by the OPAL experiment [84].

One of the main goals in particle physics is to understand the mechanism of electroweak symmetry breaking which is the source of non-zero mass values for fermions and for the IVB masses. The search for the H^o will be one of the main topics of physics

studies at future accelerators [85]. Since the mass of the H^0 is unknown, the studies must be performed over a large range on m_{Higgs} ($80 < m_{Higgs} < 1000$ GeV/c^2, where the lower range is given by the possible limit of LEP II), requiring new colliders which are capable of providing collisions at the highest luminosities to obtain measurable rates at centre-of-mass energies of ≥ 1 TeV. The various Higgs production mechanisms and experimental signatures are the subject of intensive studies in view of detector design for the multi-TeV machines, LHC and SSC.

9. CONCLUSIONS AND OUTLOOK

After a very successful operation of the CERN and the FERMILAB $\bar{p}p$ colliders in the years 1988 and 1989 large integrated luminosities of 9.2 and 9.1 pb^{-1}, respectively, have been delivered to the experiments of which UA1 has accumulated on tape 5.4 pb^{-1}, UA2 7.8 pb^{-1} and CDF 4.7 pb^{-1}.

These large statistics have been used to obtain rather precise W and Z cross section measurements and their ratio from which, by imposing the measured total width of the Z boson from the LEP experiments, the total width of the W boson could be deduced for the first time. A value of

$$\Gamma_W = 2.184 \pm 0.124 \text{ GeV}/c^2$$

has been found, compatible with Standard Model expectations for a heavy top-quark.

The ratio of the partial cross sections for the various W decay modes have been used for a test of the universality of the weak charged couplings to electrons, muons and taus which is unique for the $\bar{p}p$ colliders. The results are consistent with unity as expected in the Standard Model to better than 10%.

The transverse momentum spectra of the W and the Z boson for both UA2 and CDF do agree well with the perturbative QCD predictions, also at the high tail once the experimental uncertainties due to detector effects have been taken into account, thus showing no significant excess indicative of new physics.

UA2 has extracted a signal of the hadronic decay modes of the W and Z bosons (not separated) with a significance of four standard deviations. The fitted W mass, $m_W = 79.2 \pm 1.7$ GeV/c^2, is consistent with Standard Model expectations. This

observation of a very significant W, $Z \rightarrow q\bar{q}$ signal over a large QCD background indicates good prospects for jet spectroscopy at future hadron colliders as a method to discover possible new heavy particles.

From these large data samples precise measurements of the W and Z boson masses and their mass ratio have been obtained by the UA2 and CDF experiments. A combined value for the W mass of

$$m_W = 80.14 \pm 0.31 \text{ GeV}/c^2$$

has been measured which is not yet precise enough to significantly constrain the still unknown parameters of the Minimal Standard Model, m_{top} and m_{Higgs}. But these measurements allow a direct determination of the electroweak parameter, $\sin^2\theta_W$, independent of other experiments and of theoretical uncertainties providing therefore a stringent test of the Standard Model complementary to the e^+e^- experiments at LEP and SLC. A combined value of $\sin^2\theta_W$ determined from the W and Z mass ratio has been measured to

$$\sin^2\theta_W = 0.2265 \pm 0.0062$$

which agrees well with the measurement from low energy νN scattering experiments and also with the results from the LEP experiments. From this measurement a lower limit on the mass of the top-quark has been obtained to

$$m_{top} < 219 \text{ GeV}/c^2$$

at the 95% confidence level with $m_{Higgs} < 1000 \text{ GeV}/c^2$. Combining all $\sin^2\theta_W$ values obtained from various reactions including low energy and atomic physics data, properly taking into account the different definitions of $\sin^2\theta_W$ with the related differences in the uncertainties, a new world average value of

$$\sin^2\theta_W = 0.2290 \pm 0.0028$$

has been determined for an arbitrary value of the top-quark mass. From this value an upper limit on the mass of the top-quark has been deduced which is

$$m_{top} < 177 \text{ GeV}/c^2$$

at the 95% confidence level with $m_{Higgs} < 1000$ GeV/c^2. Using the best measurement of m_W and the best measurement of the mass ratio, m_W/m_Z, from the $\bar{p}p$ collider experiments a value for the radiative corrections of

$$\Delta r = 0.045 \pm 0.020$$

has been obtained. This value is still not precise enough to conclude on the existence of radiative corrections from other than known sources.

Direct searches for the top-quark have given a best lower limit of its mass to

$$m_{top} > 89 \text{ GeV}/c^2$$

by the CDF experiment, which makes its detection probably out of reach for the CERN collider in view of the much higher cross section at the TEV-I energy. It also makes its discovery unlikely even for LEP II.

In general, since the discovery of the W and Z bosons in 1983, all experimental results from the $\bar{p}p$, the e^+e^- colliders and from deep-inelastic lepton nucleon scattering experiments have confirmed the Standard Model in its minimal form with increasing precision and probing an increasing variety of aspects. The fact that the top-quark and the Higgs particle have not (yet) been found does not indicate a flaw in the Minimal Standard Model given the presently known mass limits. It calls for experiments which are capable to measure the Standard Model parameters, such as m_W, m_Z, $\sin^2\theta_W$ or Δr with much higher accuracy than it is possible today. It also requires much higher statistics than presently available. The production of Vector Boson pairs which result from the Vector Boson self-interactions predicted by the Standard Electroweak Theory is particularly interesting. Furthermore any deviation from the standard couplings, i.e. anomalous Vector Boson self-interactions, becomes apparent at higher Vector Boson invariant masses due to amplitudes which grow with energy. The observation of W^+W^- pairs close to its threshold is possible with LEP II, but to reach a sensitivity to the percent level in testing the existence of anomalous Vector Boson couplings much higher luminosities at much higher centre-of-mass energies are needed. Also the search for the neutral scalar Higgs particle predicted by the Minimal Standard Model - the detection will allow to understand the source of non-zero mass values for fermions and for the Intermediate Vector Bosons - will be one of the main topics of physics studies at future accelerators.

In the near future the precision measurements of the W properties and the search for the top-quark with increased statistics will remain the main goal of the $\bar{p}p$ colliders. UA2 has just started a new running period which is expected to increase the existing statistics by a factor of two. CDF and DØ are scheduled to take data from summer 1991 to 1992. Each experiment expects ~ 25 pb^{-1} after one year of running. This increase in statistics should allow for a precision of the W mass measurement to $\Delta m_W = \pm 220$ MeV/c^2 including statistical and systematic uncertainties and, if the top-quark is not too heavy ($m_{top} \leq 130$ GeV/c^2), it should be discovered at the Fermilab TEV-I collider by then.

In the long term future until end of 1995 due to the 44 bunch operation of the TEV-I collider a more than tenfold increase in statistics is expected. This would allow the CDF and the DØ experiments to get a detailed understanding of their systematic uncertainties on the W mass measurement with help of the Z statistics. A reasonable uncertainty of $\Delta m_W = \pm 100$ MeV/c^2 on the W mass can be expected which makes the TEV-I collider competitive with LEP II.

ACKNOWLEDGEMENTS

I would like to thank P. Darriulat, L. DiLella, D. Froidevaux and J.M. Gaillard for useful discussions and critical comments and careful reading of the manuscript and A.G. Clark for providing me with detailed informations about the CDF experiment. I am very grateful to M. Prost for her help in preparing the manuscript.

REFERENCES

1. The Staff of the CERN Proton-Antiproton Project, Phys. Lett. **107B** (1981) 306.
2. UA1 Collaboration, G. Arnison et al., Phys. Lett. **122B** (1983) 103;
   UA2 Collaboration, M. Banner et al., Phys. Lett. **122B** (1983) 476;
   UA1 Collaboration, G. Arnison et al., Phys. Lett. **126B** (1983) 398;
   UA2 Collaboration, P. Bagnaia et al., Phys. Lett. **129B** (1983) 130.
3. S.L. Glashow, Nucl. Phys. **22** (1961) 579;
   S. Weinberg, Phys. Rev. Lett. **19** (1967) 1264;
   A. Salam, Elementary Particle Theory, Ed. N. Svartholm, Stockholm,
   "Almquist and Wiksell" (1968), p. 367.
4. UA2 Collaboration, M. Banner et al., Phys. Lett. **118B** (1982) 203;
   UA1 Collaboration, G. Arnison et al., Phys. Lett. **123B** (1983) 115.
5. E. Jones, Proc. of the 6th Topical Workshop on Proton-Antiproton Collider Physics, Aachen 1986, World Scientific, Singapore (1987), p. 691.
6. Mark II Collaboration, G. S. Abrams et al., Phys. Rev. Lett. **63** (1989) 2173;
   ALEPH Collaboration, D. Decamp et al., Phys. Lett. **231B** (1989) 519
   and CERN - PPE/90 - 104;
   DELPHI Collaboration, P. Aarnio et al., Phys. Lett. **231B** (1989) 539
   and P. Abreu et al., CERN - PPE/90 - 119;
   L3 Collaboration, B. Adeva et al., Phys. Lett. **231B** (1989) 508
   and Phys. Lett. **237B** (1990) 138;
   OPAL Collaboration, M.Z. Akrawy et al., Phys. Lett. **231B** (1989) 530
   and Phys. Lett. **240B** (1990) 497.
7. UA1 Collaboration, A. Astbury et al., Phys. Scr. **23** (1981) 397.
8. UA1 Collaboration, "A Proposal to upgrade the UA1 detector in order to extend its physics programme" CERN/SPSC 83 - 48 SPSC/P92 Add.3 (1983).
9. UA2 Collaboration, "Proposal to Improve the Performance of the UA2 Detector" CERN/SPSC 84 - 30 SPSC/P93 Add.2 (1984);
   UA2 Collaboration, "Proposal to Improve the Performance of the UA2 Central Detector" CERN/SPSC 84 - 95 SPSC/P93 Add.3 (1984).
10. G. Blaylock et al., Proc. of the International Conference on the impact of digital microelectronics and microprocessors on particle physics, ICTP, Trieste 1988.
11. UA2 Collaboration, C. Booth, Proc. of the 6th Topical Workshop on Proton-Antiproton Collider Physics, Aachen 1986, World Scientific, Singapore (1987), p. 381.
12. K. Borer et al., Nucl. Inst. Meth. **253A** (1987) 548;
    R. Ansari et al., Nucl. Inst. Meth. **279A** (1989) 388.
13. R. Ansari et al., Nucl. Inst. Meth. **263A** (1988) 51;

R. Ansari et al., Nucl. Inst. Meth. **288A** (1990) 240.
14. R.E. Ansorge et al., Nucl. Inst. Meth. **265A** (1988) 33;
J. Alitti et al., Nucl. Inst. Meth. **273A** (1988) 135;
R.E. Ansorge et al., CERN - EP/88 - 126 (1988);
J. Alitti et al., Nucl. Inst. Meth. **279A** (1989) 364.
15. A. Beer et al., Nucl. Inst. Meth. **224** (1984) 360.
16. K. Borer et al., Nucl. Inst. Meth. **286A** (1990) 128.
17. UA2 Collaboration, R. Ansorge et al., CERN/SPSC 85 - 3 SPSC/M399 (1985).
18. CDF Collaboration, F. Abe et al., Nucl. Inst. Meth. **271A** (1988) 387;
See also references therein.
19. CDF Collaboration, F. Abe et al., Nucl. Inst. Meth. **268A** (1988) 75.
20. D0 Collaboration, M. Marx, Proc. of the 6th Topical Workshop on Proton Antiproton Collider Physics, Aachen 1986, World Scientific, Singapore (1987), p. 458.
21. UA1 Collaboration, C. Albajar et al., Phys. Lett. **185B** (1987) 233.
22. UA2 Collaboration, J. Alitti et al., in preparation.
23. CDF Collaboration, L.D. Gladney, Proc. of the 8th Topical Workshop on Proton-Antiproton Collider Physics, Castiglione 1989, World Scientific, Singapore (1989) 376.
24. CDF Collaboration, Th.J. Phillips, Proc. of the 8th Topical Workshop on Proton Antiproton Collider Physics, Castiglione 1989, World Scientific, Singapore (1989) 361.
25. Review of Particle Properties, Phys. Lett. **239B** (1990) III.1.
26. A. Sirlin, Phys. Rev. **D22** (1980) 971;
W.J. Marciano, Phys. Rev. **D20** (1979) 274.
27. F. Antonelli et al., Phys. Lett. **91B** (1980) 90;
M. Veltman, Phys. Lett. **91B** (1980) 95.
28. W.J. Marciano and A. Sirlin, Phys Rev. **D29** (1984) 945.
29. F. Jegerlehner, Z. Phys. **C32** (1986) 425.
30. G. Burgers and F. Jegerlehner, Z Physics at LEP, Vol. I, CERN 89 - 08, p. 55.
31. G.L. Fogli and D. Haidt, Z. Phys. **C40** (1988) 379.
32. NMC Collaboration, M.A.J. Botje, Proc. of the 19th Symposium on Multiparticle Dynamics, Arles (1988), Eds. D. Schiff and J. Tran Than Van, Editions Frontiers,p.237.
33. G. Altarelli et al., Nucl. Phys. **B246** (1984) 12 and Z. Phys. **C27** (1985) 617.
34. T. Matsuura and W.L. van Neerven, Z. Phys. **C38** (1988) 623;
T. Matsuura, S.C. van der Merck and W.L. van Neerven, Phys. Lett. **211B** (1988) 171 and Nucl. Phys. **B319** (1989) 570.
35. M. Diemoz, F. Ferroni, E. Longo and G. Martinelli, Z. Phys. **C39** (1988) 21.
36. A.D. Martin, R.G. Roberts and W.J. Stirling, Phys. Lett. **206B** (1988) 327 and Mod. Phys. Lett. **A4** (1989) 1135.
37. P.N. Harriman, A.D. Martin, R.G. Roberts and W.J. Stirling, Durham Preprint,

DTP-90-04 (1990) and revised April 1990;
J. Morfin and W.K. Tung, FNAL-PUB-90-74;
J. Kwiecinski, A.D. Martin, R.G. Roberts and W.J. Stirling, Durham Preprint, DTP-90-46 (1990);
M. Glück, E. Reya and A. Vogt, Dortmund preprint, DO-TH-89/20 (1989).

38. H. Plothow-Besch, Structure Functions, Contribution to the ECFA Large Hadron Collider Workshop, Aachen, 4-9th October 1990.
39. L.W. Whitlow at al., SLAC preprint, SLAC-PUB-5100 (1989);
BCDMS Collaboration, A. C. Benvenuti et al., Phys. Lett. **237B** (1990) 529 and Phys. Lett. **237B** (1990) 559;
EMC Collaboration, M. Arneodo et al., CERN - EP/89 - 121;
NMC Collaboration, D. Allasia et al., CERN - PPE/90 - 103;
CDHSW Collaboration, J.P. Berge et al., CERN - EP/89 - 103;
WA70 Collaboration, M. Bonesini et al., Z. Phys. **C38** (1988) 371;
E605 Collaboration, C.N. Brown et al., Phys. Rev. Lett. **63** (1989) 2637.
40. J. Feltesse, Proc. of the HERA workshop, Hamburg 1987, ed. R.D. Peccei published by DESY.
41. D.W. Duke and J.F. Owens, Phys. Rev. **D30** (1984) 49;
E. Eichten, I. Hinchliffe, K. Lane and C. Quigg, Rev. Mod. Phys. 56 (1984) 579;
M. Glück, E. Hoffman and E. Reya, Z. Phys. **C13** (1982) 119.
42. F. Dydak, Review talk on results from LEP and SLC at the 25th Int. Conf. on High Energy Physics, Singapore 1990.
43. UA2 Collaboration, R. Ansari et al., Phys. Lett. **186B** (1987) 440;
UA2 Collaboration, R. Ansari et al., Phys. Lett. **194B** (1987) 158;
For earlier UA2 publications see references therein.
44. UA1 Collaboration, C. Albajar et al., Z. Phys. **C44** (1989) 15;
For earlier UA1 publications see references therein.
45. UA1 Collaboration, C. Albajar et al., CERN - PPE/90 - 141.
46. UA2 Collaboration, J. Alitti et al., Z. Phys. **C47** (1990) 11.
47. CDF Collaboration, presented by T. Westhusing, Proc. of the 25th Rencontre de Moriond on Z^0 Physics, (1990), Editions Frontiers 1990, p. 423.
48. CDF Collaboration, F. Abe et al., Phys. Rev. Lett. **62** (1989) 1005.
49. UA4 Collaboration, M. Bozzo et al., Phys. Lett. **B147** (1984) 392;
UA4 Collaboration, M. Bozzo et al., Phys. Lett. **B198** (1987) 583.
50. CDF Collaboration, F. Abe et al., Phys. Rev. Lett. **64** (1990) 152.
51. D.A. Dicus and S. Willenbrock, Phys. Rev. **D34** (1986) 148.
52. P.B. Arnold and M.H. Reno, Nucl. Phys. **B319** (1989) 37.
53. UA2 Collaboration, J. Alitti et al., Z. Phys. **C47** (1990) 523.

54. A.C. Bawa and W.J. Stirling, Durham preprint DTP/87/42 (1987).
55. CDF Collaboration, presented by J. Hauser at the Workshop on Hadron Structure Functions and Parton Distributions, 26-28th April 1990, Fermilab, Batavia, Illinois.
56. CDF Collaboration, presented by M.E.B. Franklin at the 25th Int. Conf. on High Energy Physics, Singapore 1990.
57. UA2 Collaboration, R. Ansari et al., Phys. Lett. **186B** (1987) 452.
58. UA2 Collaboration, J. Alitti et al., CERN - EP/90 - 105, submitted to Z. Phys. C.
59. U. Baur, E.W.N. Glover and A.D. Martin, Phys. Lett. **232B** (1989) 519 and references therein.
60. UA2 Collaboration, J. Alitti et al., Phys. Lett. **241B** (1990) 150.
61. CDF Collaboration, F. Abe et al., Phys. Rev. Lett. **63** (1989) 720.
62. CDF Collaboration, F. Abe et al., Phys. Rev. Lett. **65** (1990) 2243 and F. Abe et al., FNAL-PUB-90/162E to be published in Phys. Rev.
63. JADE Collaboration, DESY 88 - 154 (1988); W.W. Ash et al., Phys. Rev. Lett. **58** (1987) 1080.
64. J. Ellis and G.L. Fogli, Phys. Lett. **231B** (1989) 189 and references therein; P. Langacker et al., Phys. Rev. Lett. **63** (1989) 1920.
65. AMY and Venus Collaboration, presented by E. Low at the International EPS Conference on High Energy Physics, Madrid, September 1989, p. 467;
AMY Collaboration, S. Eno at al., Phys. Rev. Lett. **63** (1989) 1910;
TOPAZ Collaboration, I. Adachi at al., Phys. Lett. **229B** (1989) 427;
VENUS Collaboration, K. Abe at al., Phys. Rev. **D39** (1990) 3524;
VENUS Collaboration, K. Abe at al., Phys. Lett. **234B** (1990) 382;
MARKII Collaboration, G. S. Abrams at al., Phys. Rev. Lett. **63** (1989) 2447;
ALEPH Collaboration, D. Decamp et al., Phys. Lett. **236B** (1990) 511;
DELPHI Collaboration, P. Abreu et al., CERN - EP/90 - 46;
OPAL Collaboration, M. Z. Akrawy et al., Phys. Lett. **236B** (1990) 364.
66. UA1 Collaboration, C. Albajar et al., Z. Phys. **C37** (1988) 505, as updated by the result of Ref. [69].
67. L.J. Reinders et al., Phys. Rept. **127** (1985) 1; T. Alvarez et al., Nucl. Phys. **B301** (1988) 1.
68. P. Nason et al., Nucl. Phys. **B303** (1988) 607.
69. G. Altarelli et al., Nucl. Phys. **B308** (1988) 724.
70. UA1 Collaboration, C. Albajar et al., Z. Phys. **C48** (1990) 1.
71. UA2 Collaboration, T. Åkesson et al., Z. Phys. **C46** (1990) 179.
72. CDF Collaboration, F. Abe et al., Phys. Rev. Lett. **64** (1990) 142.
73. CDF Collaboration, F. Abe et al., Phys. Rev. Lett. **64** (1990) 147.

74. CDF Collaboration, presented by C. Campagnari at the 25th Int. Conf. on High Energy Physics, Singapore 1990.
75. P. Langacker et al., Phys. Rev. **D30** (1984) 1470;
U. Baur et al., preprint MPI-PAE/DTH 29/85 (1985);
E. Cohen et al., Phys. Lett. **165B** (1985) 76;
F. del Aguila et al., Nucl. Phys. **B287** (1987) 419;
D. London and J.L. Rosner, Phys. Rev. **D34** (1986) 1530.
76. UA2 Collaboration, J. Alitti et al., in preparation.
77. CDF Collaboration, presented by J. Freeman at the 25th Int. Conf. on High Energy Physics, Singapore 1990.
78. R. Brown, D. Sahdev and K. Mikaelian, Phys. Rev. **D20** (1979) 1164.
79. U. Baur and D. Zeppenfeld, Nucl. Phys. **B308** (1988) 127;
D. Zeppenfeld and S. Willenbrock, Phys. Rev. **D37** (1988) 1775;
U. Baur and E.W.N. Glover, FNAL-PUB-90/75-T.
80. H. Plothow-Besch, Summary on W and Z Physics of the Standard Model Working Group, Contribution to the ECFA Large Hadron Collider Workshop,
Aachen, 4-10th October 1990.
81. P.W. Higgs, Phys. Lett. **12** (1964) 132 and Phys. Rev. Lett. **13** (1964) 508 and Phys. Rev. **145** (1966) 156.
82. CDF Collaboration, F. Abe et al., Phys. Rev. Lett. **D41** (1990) 1717.
83. ALEPH Collaboration, D. Decamp et al., CERN - PPE/90 - 101;
DELPHI Collaboration, P. Abreu et al., CERN - EP/90 - 44;
L3 Collaboration, B. Adeva et al., L3 preprint #019 (1990);
OPAL Collaboration, M.Z. Akrawy et al., Phys. Lett. **236B** (1990) 364
and CERN - PPE/90 - 100.
84. OPAL Collaboration, M.Z. Akrawy et al., CERN - PPE/90 - 150.
85. Proc. ECFA-CERN Workshop on the Large Hadron Collider in the LEP Tunnel, Lausanne and Geneva, 21-27 March 1984, ECFA 84/85 and CERN 84-10 (1984);
Proc. of the Workshop on Physics at Future Accelerators La Thuile and Geneva, 7-13 January 1987, CERN 87-07 (1987);
Proc. of the 1984 Snowmass Summer study on the Design and Utilisation of the Superconducting Super Collider, ed. by V. Barger and F. Halzen, World Scientific, Singapore, 1987;
Proc. of the 1988 Snowmass Summer Study on High Energy Physics in the 1990's, ed. by S. Jensen, World Scientific, Singapore, 1989.

CONTENTS

1. INTRODUCTION 1

2. THE DETECTORS 2
   2.1 The UA1 detector at CERN 3
   2.2 The UA2 detector at CERN 5
   2.3 The CDF detector at FNAL 7
   2.4 The DØ detector at FNAL 9

3. PARTICLE IDENTIFICATION AND DETECTOR CALIBRATION 10
   3.1 Lepton identification 10
      3.1.1 Electron identification 10
      3.1.2 Muon identification 13
      3.1.3 "Neutrino" identification 14
      3.1.4 Tau identification 18
   3.2 Jet algorithms 20
   3.3 Detector calibrations 21

4. THEORETICAL PREDICTIONS OF THE STANDARD MODEL 26
   4.1 The W and Z masses 26
   4.2 The W and Z partial and total widths 30
   4.3 The W and Z cross sections 32

5. EXPERIMENTAL RESULTS ON THE W AND Z PRODUCTION AND DECAY PROPERTIES 36
   5.1 Inclusive W and Z production cross sections 38
      5.1.1 Determination of Γ_W from the ratio of the W and Z production cross sections 42
      5.1.2 Lepton universality 48
   5.2 Inclusive W and Z transverse momentum spectra 50
   5.3 Inclusive W and Z angular distributions 56
      5.3.1 $W^{\pm}$ decays 56
      5.3.2 Z^{o} decays 58
   5.4 Hadronic decay modes 60
   5.5 Measurement of the W and Z masses 63

6. STANDARD MODEL PARAMETERS 75

7. SEARCH FOR THE TOP-QUARK 87
   7.1 Theoretical predictions on top-quark production and decay 87
   7.2 Experimental searches for the top-quark 89
      7.2.1 Top search in ℓ + n jets events 90
         7.2.1.1 Top search in μ + 2 jets events 90
         7.2.1.2 Top search in in e + n jets events 92
      7.2.2 Top search in lepton pair + jet events 95
         7.2.2.1 Top search in 2μ + jet events 95
         7.2.2.2 Top seach in $e\mu$ + X events 95
   7.3 Summary of the limits for the top-quark search 95

8. SEARCHES FOR HEAVY IVB', IVB PAIR AND HIGGS PRODUCTION 99
   8.1 Search for heavy W' and Z' Vector Bosons 99
   8.2 Search for IVB pair production 101
   8.3 Search for the Higgs boson 102

9. CONCLUSIONS AND OUTLOOK 103

TABLES

1. Electron identification criteria 12

2. Theoretical predictions of the total W and Z production cross sections 33

3. Partial W and Z production cross sections 41

4. Ratio R of the W to the Z boson production cross section 43

5. Recomputed ratios of IVB cross sections, partial and total widths 47

6. Total width of the W boson, Γ_W 47

7. Z mass measurements 66

8. W mass measurements 70

9. Uncertainties on the W mass measurements 71

10. Ratio of the W mass over the Z mass, m_W/m_Z 72

11. Final W mass 73

12. Experimental measurements of the Weinberg angle $\sin^2\theta_W$ 76

13. Experimental measurement of the ρ parameter 82

14. Experimental measurement of the radiative corrections Δr 83

15. Experimental measurement of the mass difference $m_Z - m_W$ 85

FIGURE CAPTIONS

Fig. 1 Artistic view of the UA1 detector 3

Fig. 2 Schematic view of one quarter of the UA2 detector in the longitudinal cross section 5

Fig. 3 Perspective view of the CDF detectors 7

Fig. 4 Isometric view of the DØ detectors 9

Fig. 5 Example of the p_T^e vs p_T^ν distribution from UA2 13

Fig. 6 Resolution function of the $\not{p}_T$ measurement as a function of ΣE_T 17
a) for UA1 b) for UA2 c) for CDF

Fig. 7 p_T^W distribution with the detector response superimposed 18

Fig. 8 Response measured in summer 1989 over prediction from summer 1986 23

Fig. 9 a) Invariant mass distribution of $J/\Psi \rightarrow \mu^+\mu^-$ 24
b) Invariant mass distribution of $\Upsilon \rightarrow \mu^+\mu^-$

Fig. 10 Partial W and Z cross sections, σ_W^ℓ and σ_Z^ℓ, as a function of $\sqrt{s}$ 42

Fig. 11 Ratio R as a function of $\sqrt{s}$ 44

Fig. 12 a) Measurement of the Z boson mass from LEP and SLC 45
b) Measurement of the Z boson width from LEP and SLC

Fig. 13 Total width of the W boson, Γ_W, as a function of the mass of the top-quark 49

Fig. 14 W transverse momentum distribution, p_T^W, from UA1 52

Fig. 15 a) W transverse momentum distribution with p_T^W below 30 GeV/c from UA2 53
b) W transverse momentum distribution with p_T^W above 20 GeV/c from UA2

Fig. 16 Z transverse momentum distribution, $p_T^{e^+e^-}$ from UA2 54

Fig. 17 a) W transverse momentum distribution, p_T^W, from CDF 55
b) Z transverse momentum distribution, $p_T^{e^+e^-}$, from CDF

Fig. 18 Decay angular distribution of $W \rightarrow e\nu$ from UA1 57

Fig. 19 a) Forward-backward asymmetry of $W \rightarrow \mu\nu$ from CDF for muons 58
b) Forward-backward asymmetry of $W \rightarrow e\nu$ from CDF for electrons

Fig. 20 Decay angular distribution of $Z \rightarrow e^+e^-$ from CDF 59

Fig. 21 Two-jet mass spectrum from UA2. Vertical scale weighted by $(m/100)^6$ 61

Fig. 22 Background subtracted two-jet mass spectrum from UA2 62

Fig. 23 a) Invariant mass distribution, m_{ee}, from UA2 64
b) Invariant mass distribution, m_{ee}, from UA2 using the p_T constraint

Fig. 24 a) Invariant mass distribution, $m_{\mu\mu}$, from CDF 65
b) Invariant mass distribution, m_{ee}, from CDF using the central tracking chamber
c) Invariant mass distribution, m_{ee}, from CDF using the calorimeters

Fig. 25 a) Transverse mass distribution, $m_T^{e\nu}$, from UA2 66
b) Transverse mass distribution, $m_T^{\mu\nu}$, from CDF
c) Transverse mass distribution, $m_T^{e\nu}$, from CDF

Fig. 26 a) Electron transverse momentum distribution, p_T^e, from UA2 69
b) Neutrino transverse momentum distribution, p_T^ν, from UA2
c) Electron transverse momentum distribution, p_T^e, from CDF
d) Neutrino transverse momentum distribution, p_T^ν, from CDF for electrons
e) Muon transverse momentum distribution, p_T^μ, from CDF
f) Neutrino transverse momentum distribution, p_T^ν, from CDF for muons

Fig. 27 m_W as a function of m_Z 74

Fig. 28 m_W as a function of m_{top} 75

Fig. 29 $\sin^2\theta_W$ as a function of m_{top} 78

Fig. 30 $\sin^2\bar{\theta}_W$ as a function of m_{top} 79

Fig. 31 Summary of measurements of $\sin^2\theta_W$ 81

Fig. 32 Δr as a function of m_{top} 84

Fig. 33 $m_Z - m_W$ as a function of m_Z 86

Fig. 34 Inclusive production cross section for $t(\bar{t})$ as a function of m_{top} at $\sqrt{s} = 630$ GeV and 1.8 TeV 88

Fig. 35 Distribution on Isolation in μ + 2 jets events from UA1 91

Fig. 36 Transverse mass distribution for e + $\geq$ 1 jet(s) events from UA2 93

Fig. 37 Transverse mass distribution for e + $\geq$ 1 jet(s) events from CDF 94

Fig. 38 Inclusive production cross section for $t(\bar{t})$ as a function of m_{top} from UA1 96

Fig. 39 Inclusive production cross section for $t(\bar{t})$ as a function of m_{top} from UA2 96

Fig. 40 Inclusive production cross section for $t\bar{t}$ as a function of m_{top} from CDF 98
a) for the e + jet sample b) for lepton pairs.

Imprimé au CERN. Prix : 3.55 Fr.